THESIS FOR THE DEGREE OF DOCTOR OF PHILOSOPHY

Plasmonic Gold Nanorods as Probes of Soft Matter and Biological Systems

EMELIE TORNÉUS

Department of Physics and Astronomy
Chalmers University of Technology
Gothenburg, Sweden 2026

Plasmonic Gold Nanorods as Probes of Soft Matter and Biological Systems

EMELIE TORNÈUS
ISBN 978-91-8103-425-7

Acknowledgements, dedications, and similar personal statements in this thesis, reflect the author's own views.

Doktorsavhandlingar vid Chalmers tekniska högskola
Ny serie nr 5882
ISSN 0346-718X
DOI: https://doi.org/10.63959/chalmers.dt/5882

Department of Physics and Astronomy
Division of Nano- and Biophysics
Chalmers University of Technology
SE-412 96 Gothenburg
Sweden Telephone +46 31 772 1000

Chalmers Digitaltryck
Gothenburg, Sweden 2026

Cover: 'Shapes in Blue', 2026. Painted by the author in watercolor and ink.

Plasmonic Gold Nanorods as Probes of Soft Matter and Biological Systems
EMELIE TORNÉUS
Department of Physics and Astronomy
Chalmers University of Technology

Abstract

Motion and structure at the nanoscale encode information about local forces, mechanical properties, and dynamic interactions that are difficult to access using conventional measurement techniques. This challenge is particularly pronounced in biological and soft-matter systems, where fluctuations and structural changes demand probes combining minimal perturbation with high spatial and temporal sensitivity. Plasmonic gold nanorods provide such a platform. Their localized surface plasmon resonance gives rise to strong light scattering for sensitive optical readout, while optical forces and torques enable controlled trapping, translation and rotation.

This thesis explores gold nanorods as nanoscale probes in complex biological and physical environments. Single nanorods are optically trapped and driven to rotate by circularly polarized light, transducing local mechanical activity into rotational-frequency fluctuations. Applied to living endothelial cells, this light-driven nanomotor platform resolves heterogeneous nanoscale motions across the nucleus, perinuclear region, and cell periphery, and uncovers transient oscillations that reveal short-lived mechanical events typically inaccessible to conventional methods. The same rotational control, applied beyond biology, enables low-contact profilometry through lateral scanning of a trapped nanorod over nanoscale surface features. In another approach, nanorods serve as intracellular tracers of vesicular motion. Dark-field microscopy combined with deep-learning-based particle tracking and state segmentation enables long-duration, high-throughput analysis of intracellular transport in prostate cancer cells, resolving confined, diffusive, and directed motion across large trajectory ensembles. This reveals distinct transport phenotypes, with diffusion dominating in both cell lines and directed transport occurring as short-lived bursts. Nanorod surface chemistry further shapes this behavior, modulating the coupling between vesicle loading and active transport. Together, these studies establish plasmonic gold nanorods as a versatile platform for probing nanoscale dynamics with minimal perturbation across biological and physical systems. The results highlight the pronounced heterogeneity of such environments and demonstrate how a single nanoscale probe, viewed through light, can resolve motion and structure across diverse complex systems.

Keywords: Nanoscale, Living Cells, Cell Dynamics, Intracellular transport, Optical Tweezers, Nanorod Rotation, Diffusion, Dark Field Microscopy, Profilometry

List of Publications

This thesis is based on the following papers:

Paper I

Rotating Gold Nanomotors for High-Resolution Mapping of Subcellular Nanomotions
Emelie Tornéus, Charlotte Hamngren Blomqvist, Caroline Beck Adiels, and Hana Šípová-Jungová
Small Methods ***2025****, 9, e01393*

Paper II

Gold Nanorod Tracking and Deep-learning Analysis Reveal Intracellular Transport Phenotypes in Therapy-resistant Prostate Cancer Cells
Emelie Tornéus, Yuchao He, Mirja Granfors, Jesús Pineda, Caroline Beck Adiels, Giovanni Volpe and Hana Šípová-Jungová
In Manuscript

Contribution to Papers

Paper I
I conducted all experimental work, including method development and optimization, established the data analysis framework, and contributed to manuscript writing.

Paper II
I performed data analysis of single-particle trajectories, including intensity quantification, velocity characterization, and sub-trajectory transport-state classification, and interpreted the results. I conducted the SPR experiments and contributed to manuscript writing.

Declaration of Transparency

This thesis is a continuation of the work published in the licentiate thesis "*Optically Driven Nanomotors for Cellular Motion Detection at the Nano-Scale*" By Emelie Tornéus, Chalmers University of Technology, 2024.[1] Parts of the theoretical background and introductory material originate from the licentiate thesis but have been revised and expanded. The chapters included in the present work have been updated to reflect additional results, extended analyses, and research carried out after the licentiate degree.

Generative AI tools were used during the writing of this thesis to assist with language editing, proofreading, and improving clarity of the text. They were not used to generate scientific content, perform analysis, or formulate conclusions, and the author takes full responsibility for the content of this thesis.

Acknowledgements

The journey to becoming a researcher is a winding and wandering path, and without support and encouragement it is easy to lose your way. I have been fortunate to have a wonderful group of people around me, keeping me on the right track — because, as the saying goes, "it takes a village to raise a PhD student".

First, I want to thank my supervisor, Hana Jungová. Thank you for giving me this opportunity and for your invaluable guidance throughout this work. I have learnt a great deal from you, and I am especially grateful for your unwavering support and for always having my back, even when the path was not straightforward. To Mikael Käll, also my supervisor — thank you for your honest and thoughtful advice, and for everything you have taught me along the way. I am grateful for your support throughout this journey. I would also like to thank my examiner, Fredrik Höök, for the inspiring science you do, and for giving me a much-needed course in biophysics at the beginning of my PhD.

Caroline Beck Adiels, I am very grateful for our interesting discussions and for your advice throughout the years. Charlotte Hamngren Blomqvist — thank you for keeping those cells alive and for so generously sharing your knowledge with me. You are amazing. I would also like to thank the rest of the GU crew for the good company, the conversations, and the many shared moments that made this time so enjoyable.

To my colleagues on floor 6 — especially Pantea, Laura, and Betül — I am grateful for all your support, and for all the brilliant advice and conversations throughout the years. To Khosro, Oliver O., Erik, Marco, Timur, Michaela, Oliver S., Arthur, Zengya, Abhay, and everyone who has passed through over the years — thank you for the encouraging atmosphere that has kept the science going, and for the conversations, the laughter, and the countless lunches and fikas that have made floor 6 such a special place to spend my days.
I would also like to thank all my former and present colleagues at the Nano and Biophysics department for creating such a welcoming and inspiring environment to grow in.

To the wonderful women united by physics — Adriana, Pantea, Ariadna, Laura, Julia, Mirna, Rebecka, Hanna, Juliette and Yashna — thank you for the community and the laughter. You became such an important part of my PhD, and your encouragement and kindness have meant the world to me. I am grateful our paths crossed.

Kajsa — for ten years we have accompanied each other in our quest for knowledge at Chalmers, and I think we can finally say mission accomplished. Thank you for all the laughs, and for always being a sounding board. I am so happy I got to share this journey with you.

To my dear friends — Frida, Sanna, Josef, Govin, Ale, Amir, Sofia, Harald, Julia, Victor, Stina, and Emma — you are such a special bunch, and I am in awe of every single one of you. And to Leo and Cornelia, who have stolen my heart entirely — thank you for all the joy, distraction, and warmth you have brought into my life outside of research.

To my parents — thank you for always encouraging and believing in me. To Eleonor, my big sister and my brothers, Erik and Emil, thank you for always being there for me. To my girls — Elvira, Siri, Aili, Lisa, Edith, and Helmi — thank you for reminding me of what is actually important. To Matti and my extended family, the Kettunens — thank you for being my foundation.
Finally — thank you, Johan, for everything. For being my home, my calm, and my reminder that there is a world out there.

Emelie Tornéus
2026/05/01
Göteborg

Abbreviations

ACF	Autocorrelation Function
AFM	Atomic Force Microscopy
AuNP	Gold Nanoparticle
AuNR	Gold Nanorod
BSA	Bovine Serum Albumin
CCM	Cell Culture Medium
CCV	Clathrin-Coated Vesicle
CIE	Clathrin- and Caveolae-Independent Endocytosis
CME	Clathrin-Mediated Endocytosis
COOH	Carboxyl
CTAB	Cetyltrimethylammonium Bromide
DDA	Discrete Dipole Approximation
DF	Dark-field
DFM	Dark-field Microscopy
DFT	Discrete Fourier Transform
DLVO	Derjaguin–Landau–Verwey–Overbeek (theory)
DPBS	Dulbecco's Phosphate-Buffered Saline
DTFT	Discrete-Time Fourier Transform
EDL	Electric Double Layer
EGF	Epidermal Growth Factor
EM	Expectation–Maximization
EthD-1	Ethidium Homodimer-1
FBS	Fetal Bovine Serum
FDTD	Finite-Difference Time-Domain
FEM	Finite Element Method
GFP	Green Fluorescent Protein
GNN	Graph Neural Network
HMEC-1	Human Microvascular Endothelial Cell line 1
HMM	Hidden Markov Model
IQR	Interquartile Range
LNCaP	Lymph Node Carcinoma of the Prostate

LodeSTAR	Localization and detection from Symmetries, Translations And Rotations
LSPR	Localized Surface Plasmon Resonance
MAGIK	Motion Analysis through GNN Inductive Knowledge
MLWA	Modified Long Wavelength Approximation
MP-SPR	Multi-Parametric Surface Plasmon Resonance
MSD	Mean Squared Displacement
NA	Numerical Aperture
NaOL	Sodium Oleate
NIR	Near-Infrared
OAM	Orbital Angular Momentum
OH	Hydroxyl
PA	Protein Adsorption
PBS	Phosphate-Buffered Saline
PC	Protein Corona
PDMS	Polydimethylsiloxane
PEG	Polyethylene Glycol
PMT	Photomultiplier Tube
PSA	Power Spectral Analysis
PVP	Poly(vinylpyrrolidone)
QPD	Quadrant Photodiode
ROI	Region of Interest
SAM	Self-Assembled Monolayer
sCMOS	Scientific Complementary Metal–Oxide–Semiconductor
SD	Standard Deviation
SEM	Scanning Electron Microscopy
SG	Savitzky–Golay
SPR	Surface Plasmon Resonance
SPT	Single-Particle Tracking
STFT	Short-Time Fourier Transform
TCSPC	Time-Correlated Single-Photon Counting
vdW	van der Waals

Contents

1

Introduction

With the invention of the microscope in the 17th century, we gained the ability to observe the world at scales far smaller than those accessible to the naked eye, a development that profoundly changed our understanding of nature. This new access to the microscopic world quickly captured scientific curiosity and soon directed attention toward the fundamental building blocks of life. In 1665, Robert Hooke was the first to observe and name *cells* in his publication Micrographia, based on his studies of cork.[2] Shortly thereafter, Antonie van Leeuwenhoek reported the first observations of living cells in his correspondence with the Royal Society of London, revealing that life itself could be studied at microscopic scales.[3] Yet conventional optical microscopy carries a fundamental limitation: the diffraction of light restricts spatial resolution to approximately half its wavelength, preventing direct observation of structures at the tens-of-nanometers scale. Reaching beyond this barrier has required the development of more advanced techniques, and as experimental methods have continued to evolve, attention has increasingly shifted toward even smaller length scales, where nanoscale structure and dynamics govern the behavior of both biological and physical systems.

At the nanoscale, the world behaves very differently from what we experience in everyday life. In the aqueous environments where most biological and many physical processes take place, gravity plays only a minor role, while the behavior of nanoscale objects is largely governed by van der Waals and electrostatic interactions.[4] A single collision with a surrounding water molecule can suddenly redirect a nanoscale object, a phenomenon we recognize as Brownian motion. These principles take on a particularly

rich form inside living cells, which, if we could step inside, would resemble a densely populated city rather than a quiet environment. The activity arises from thermal fluctuations that drive diffusion, as well as from active transport by molecular motors along cytoskeletal filaments and microtubules.[5,6] Motion at these scales is further characterized by low Reynolds numbers, meaning that viscous forces dominate over inertia and movement is regulated by an instantaneous balance between applied forces and hydrodynamic drag.[7,8] Even motor-driven transport remains subject to this regime. As a result, cargo moves at an approximately constant velocity and stops almost immediately when the motor detaches, after which Brownian motion once again dominates.

Although the general physical principles governing nanoscale behavior are well established, directly observing and quantifying them in living and dynamic systems remains fundamentally challenging. While some techniques can resolve individual atoms, capturing nanoscale dynamics in living systems remains particularly difficult, as high spatial resolution often requires fixed samples, vacuum environments, or invasive probing.[9–12] Among available tools, optical microscopy is particularly valuable for studying living systems because it enables imaging without mechanical perturbation,[13] and fluorescence microscopy further extends this capability by allowing selective labeling and visualization of specific molecules or structures against a dark background.[14] To reach the nanoscale with light, super-resolution microscopy was developed to extend optical imaging beyond the diffraction limit, enabling visualization at nanometer resolution.[15–17] These advances demonstrate how methodological innovation is required to access the nanoscale using light.

However, resolving structure alone is not sufficient to understand nanoscale behavior. Many processes at this scale, from molecular motor activity to the mechanical response of soft biological structures, involve forces and displacements that imaging alone cannot capture, requiring tools that can both apply and measure mechanical interactions directly. Optical tweezers, for example, allow forces and torques to be applied and measured on individual micro- and nanoscale objects with piconewton precision and nanometer spatial resolution.[18–23] Atomic force microscopy similarly enables imaging and force measurements at nanometer resolution.[11,12,24–27] Yet, combining non-invasive optical readout with active manipulation and nanoscale sensitivity remains a central challenge.

Plasmonic gold nanorods offer a unique platform to bridge this gap. Because of their strong, tunable optical response in the visible-to-near-infrared regime and their anisotropic geometry, gold nanorods can be optically tracked, trapped, and rotated, enabling simultaneous measurement and manipulation at the nanoscale. Their motion, both translational and rotational, encodes information about the surrounding nanoscale environment, encoding local interactions in measurable optical signals.

This thesis presents optical probing and manipulation of plasmonic gold nanorods as a unified approach to investigate nanoscale structures and dynamics. Within living cells, internalized nanorods act as nanoscale cargo whose trajectories reveal how diffusion, motor-driven transport, and surface chemistry shape intracellular dynamics. When optically trapped and rotated near cellular interfaces, the same particles become probes of sub-cellular nanomotion, enabling low-contact measurements of transient mechanical activity.[28] Extending this concept beyond biological systems, controlled rotation of trapped nanorods is applied to nanoscale profilometry, where variations in scattering and rotational response provide a means to map surface structures without perturbing the system. Across these studies, the motion of a single nanorod functions as a transducer linking optical interaction to the local nanoscale environment, demonstrating how a single nanoscale probe, viewed through light, can resolve dynamics across both biological and physical systems.

Thesis Outline

The thesis is organized into seven chapters. **Chapter 2** introduces the interaction between light and matter, forming the theoretical foundation of this thesis. The optical properties of noble metals are presented, with emphasis on size- and shape-dependent effects, localized surface plasmon resonances, and the resulting absorption, scattering, and photothermal phenomena. Building on this, **Chapter 3** outlines the theoretical framework for optical trapping and manipulation of gold nanorods. Optical forces are described within the dipole approximation, followed by a discussion of light-driven rotation of anisotropic particles, Brownian motion of trapped nanoparticles, and the role of surface interactions in two-dimensional trapping configurations.

Chapter 4 then shifts focus from the physics of the nanorod itself to its behavior in biological environments, covering colloidal stability and surface functionalization in cell culture media, protein corona formation, nanoparticle–cell interactions, and the mechanisms and analysis of intracellular transport. With the theoretical and biological foundations established, **Chapter 5** describes the experimental and analytical methods used throughout the thesis, including nanorod synthesis and functionalization, dark-field microscopy, optical tweezers, rotational readout, deep-learning-based single-particle tracking, and cell culture procedures.

Chapter 6 summarizes the appended papers and describes how the framework developed in the preceding chapters was applied to measurements of cellular nanomotion and intracellular transport in prostate cancer cells. Finally, **Chapter 7** summarizes the key results of this work and discusses potential directions for future research.

2

Plasmonic Gold Nanoparticles

The interplay between light and matter underpins our ability to visually perceive the world around us. When light interacts with an object, its material composition, size, and geometry determine how the light is scattered and absorbed, ultimately shaping how the object appears to an observer. These two fundamental processes, scattering and absorption, govern light–matter interactions across a wide range of length scales.

At the nanoscale, metallic nanoparticles exhibit a particularly strong optical response. When illuminated, their conduction electrons oscillate collectively with the incident electromagnetic field, giving rise to a localized surface plasmon resonance that dramatically enhances both scattering and absorption. The following chapter develops the framework needed to describe this interaction for gold nanoparticles. **Section 2.1** introduces the optical properties of noble metals through the Drude model. **Section 2.2** derives the optical response of sub-wavelength particles using the quasi-static approximation, and ends with the light-induced heating that arises from plasmonic absorption.

2.1 Optical Properties of Noble Metals

Light, described from a classical perspective, is an electromagnetic wave with oscillating electric and magnetic fields. In this thesis, we focus on the light–matter interactions of gold, a non-magnetic material, for which the interaction is governed predominantly by the electric field. Therefore, we consider a plane electric wave propagating in space, given by

$$\mathbf{E}(\mathbf{r}, t) = \mathbf{E}e^{i(\mathbf{k}\cdot\mathbf{r}-\omega t)}. \tag{2.1}$$

Here, $\mathbf{r}$ denotes the position vector, $\mathbf{k}$ the wave vector, and $\omega = 2\pi f$ the angular frequency, where f is the frequency of light. The magnitude of the wave vector, $k = |\mathbf{k}|$, is known as the wavenumber and is given by $k = \frac{2\pi}{\lambda}$, where λ is the wavelength. The relationship between the wavenumber and the angular frequency is known as the *dispersion relation* $k = \frac{\omega}{c}$, where $c \approx 3 \times 10^8$ m/s is the speed of light in vacuum.[29]

In a homogeneous material, the propagation of light is determined by the complex refractive index $N = n' + in''$, leading to the dispersion relation $k = \frac{\omega}{c}N$. The refractive index becomes complex in absorbing materials, such as gold, to account for dissipative losses within the medium. The imaginary part (n''), often referred to as the attenuation coefficient, accounts for absorptive losses within the medium, while the real part (n') functions as a scaling factor for the properties of the wave[a]. The refractive index is closely related to the *permittivity* of the material. When an incident electric field $\mathbf{E}$ interacts with a material, it displaces the charged particles, leading to a distortion of both the material and the field. This response is captured by the electric displacement field $\mathbf{D}$, defined as

$$\mathbf{D} = \varepsilon_0\mathbf{E} + \mathbf{P}. \tag{2.2}$$

Here, $\mathbf{P}$ is the macroscopic polarization density, that is, the total induced polarization of the material and ε_0 is the permittivity of free space. For a material such as gold, which is non-magnetic, linear[b], isotropic[c] and homogeneous[d], the polarization density is proportional to the electric *susceptibility* χ, as

$$\mathbf{P} = \varepsilon_0\chi\mathbf{E} \tag{2.3}$$

which leads to

[a] The frequency remains unchanged, while the phase velocity, wavelength, and wavenumber are altered.[30]

[b] A material is *linear* if the interaction with light is independent on the intensity, or the amplitude $|\mathbf{E}_0|$ of the incident field.

[c] A material is *isotropic* if the material have the same optical properties in all directions.

[d] A material is said to be *homogeneous* if its properties are the same throughout.

$$\mathbf{D} = \varepsilon \mathbf{E}. \tag{2.4}$$

with permittivity $\varepsilon = \varepsilon_r \varepsilon_0 = \varepsilon_0(\chi + 1)$, where ε_r is the relative permittivity, describing how a material responds to an applied electric field. The interaction between light and matter is stronger for a material with large ε_r, and vice versa if ε_r is small (**Figure 2.1**).

For a single frequency or wavelength, the permittivity is a constant. However, the optical response of a material is dispersive and depends on the frequency of light (ω). Hence, it makes sense to introduce the relative permittivity as a function of frequency $\varepsilon_r(\omega)$, which is often referred to as the dielectric function of the material. $\varepsilon_r(\omega)$ is complex-valued, as the material cannot respond to a change in the applied field instantaneously, which results in a phase difference between **D** and **E**.

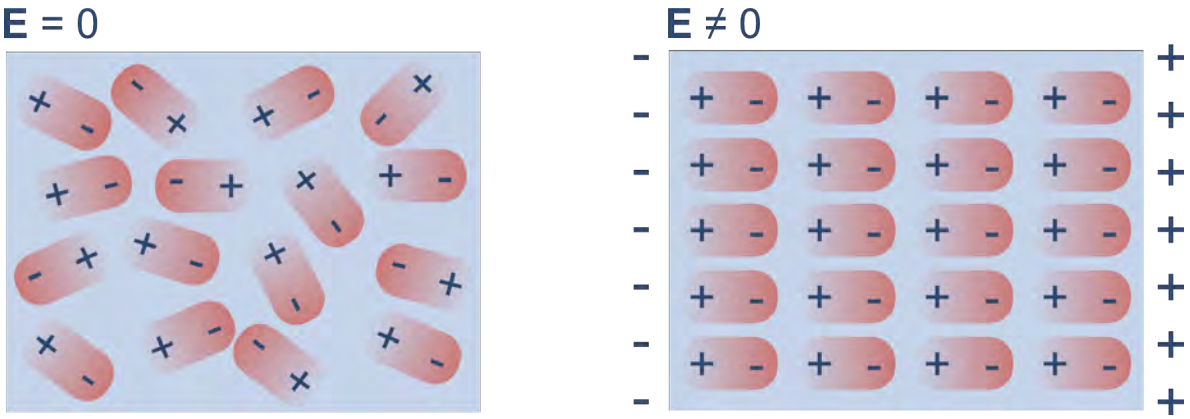

Figure 2.1: Permittivity is a measure of the electric polarizability of a material and quantifies how much the material permits the formation of electric fields within it. Left: no electromagnetic field (**E**) is applied and the material is unpolarized. Right: The material becomes polarized with an applied **E**-field.

The relative permittivity $\varepsilon_r(\omega)$ of many materials can be well described by the relatively simple classical Drude–Lorentz model.[29] In this model, the electrons within the material are treated as simple harmonic oscillators subjected to the driving force of the applied electric field **E**. Since the mass of a nucleus is much larger than that of an electron ($m_n \gg m_e$), the nuclei can be assumed to remain stationary. An electron is then treated as being bound to its nucleus by a restoring force that follows Hooke's law, while also experiencing a damping force proportional to its velocity. Applying Newton's second

law, the equation of motion for each electron in a homogeneous and isotropic material becomes that of a damped harmonic oscillator

$$\ddot{\mathbf{x}}(t) + \zeta\dot{\mathbf{x}}(t) + \omega_0^2\mathbf{x}(t) = -\frac{e}{m_e}\mathbf{E}(t), \tag{2.5}$$

where $\mathbf{x}$ is the displacement of the electron, m_e is the electron mass, ζ is the damping coefficient, e is the electron charge, and ω_0 is the resonance frequency. The terms on the left-hand side represent the acceleration, damping, and restoring force, respectively, while the right-hand side describes the driving force due to the applied electric field. By performing a Fourier transform with respect to the angular frequency ω, and solving **Equation 2.5** for $\mathbf{x}(\omega)$, we get

$$\mathbf{x}(\omega) = \frac{-(e/m_e)}{\omega_0^2 - \omega^2 - i\zeta\omega}\mathbf{E}(\omega). \tag{2.6}$$

Each electron gives rise to an induced dipole moment $p = -ex$, which contributes to the total macroscopic polarization. The total polarization $\mathbf{P}$ is then obtained by summing over all such dipole moments within a unit volume. If q denotes the number of electrons per unit volume, this gives

$$\mathbf{P}(\omega) = -qe\mathbf{x}(\omega) = \frac{qe^2/m_e}{\omega_0^2 - \omega^2 - i\zeta\omega}\mathbf{E}(\omega). \tag{2.7}$$

By combining **Eq. 2.3** and **Eq. 2.7**, we obtain the susceptibility $\chi(\omega)$, and using $\varepsilon_r = 1 + \chi$ we arrive at the relative Lorentz permittivity,

$$\varepsilon_r(\omega) = 1 + \chi(\omega) = 1 + \frac{\omega_P^2}{\omega_0^2 - \omega^2 - i\zeta\omega} \tag{2.8}$$

where $\omega_P = (qe^2/\varepsilon_0 m_e)^{1/2}$ is the plasma frequency.

The first term of **Eq. 2.8** refers to the vacuum response and the second term is the material's response. For conducting materials, very little energy from the applied field $\mathbf{E}$ is needed to excite the electrons to a higher energy state, they are so-called *free* electrons. The optical response of free electrons can be described using the Lorentz model by releasing the electrons from the restoring force of the nucleus, i.e., by setting the spring constant to zero, or equivalently the natural frequency $\omega_0 = 0$,[31] in **Eq. 2.7**. This reduces the Lorentz model to the Drude model of free electrons:

$$\varepsilon_r(\omega) = \varepsilon_\infty - \frac{\omega_P^2}{\omega^2 + i\zeta\omega}. \tag{2.9}$$

The first term in **Equation 2.9**, ε_∞, now accounts for the response of the material background of bound electrons oscillating at high frequencies.[29] The damping frequency $\zeta = 1/\tau$ is related to the relaxation time τ of the electrons, which is the average time an electron travels between collisions with lattice vibrations or impurities[e].

The Drude approximation of the permittivity does not account for interband transitions between the conduction and valence bands in the material. For gold, which is the material used in this thesis, these interband transitions are responsible for the enhanced absorption at wavelengths below 600 nm.[32] In more general Drude-Lorentz models, additional Lorentz terms can be included to account for these transitions involving bound electrons. In **Figure 2.2**, the real and imaginary parts of the relative permittivity of gold are shown together with experimentally measured data. However, in the spectral range of interest for this work, the Drude approximation provides a sufficiently accurate description.

Now that we have an expression for the permittivity, we recall the expression for the complex refractive index N introduced at the beginning of this chapter, and can see how they are related as

$$\sqrt{\varepsilon_r} = N = n' + in''. \tag{2.10}$$

Denoting the real and imaginary part of the relative permittivity as ε_r' and ε_r'', we can now write them as a function of n and and vice versa,

$$\varepsilon_r' = n'^2 - n''^2 \tag{2.11}$$

$$\varepsilon_r'' = 2n' \cdot n''. \tag{2.12}$$

The refractive index is often considered more intuitive than the permittivity, as it is directly connected to the wave properties during propagation in the medium, describing both the phase velocity and the attenuation of the electromagnetic wave.[33]

[e]Within the Drude model, the electrical conductivity is given by $\sigma = \frac{ne^2\tau}{m_e}$, showing that the relaxation time τ determines how efficiently charge carriers respond to an applied electric field.

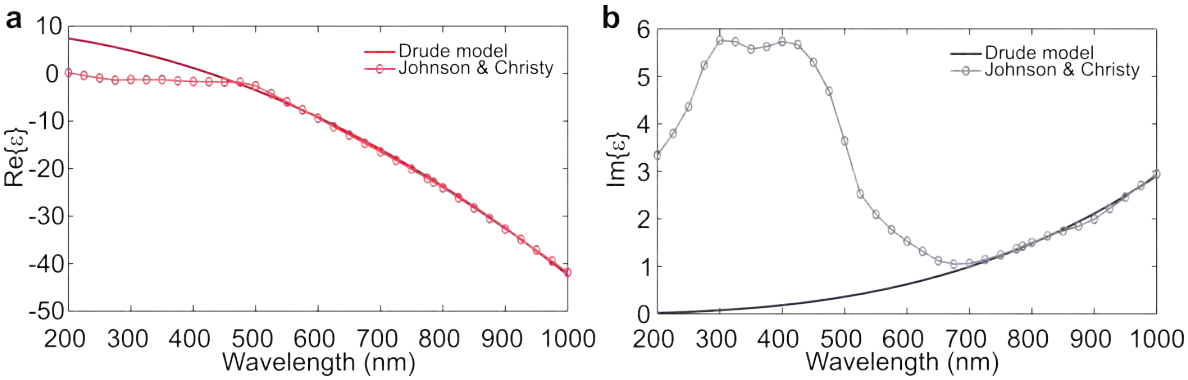

Figure 2.2: Real (**a**) and imaginary (**b**) part of the relative permittivity (ε) for gold, calculated with the Drude model using a plasma frequency of $1.4{\cdot}10^{16}$ (rad/s), damping frequency $1.05{\cdot}10^{14}$ (rad/s) and high-frequency permittivity of 9.5.[34] The Drude model is compared with experimentally measured permittivity from Johnson and Christy.[35]

2.2 Light-Matter Interaction of Sub-wavelength Particles

The optical properties described in the previous section apply to bulk materials without spatial constraints. We now consider how these interactions change when the material is confined to sub-wavelength dimensions. In this regime, the macroscopic description in terms of propagation of light is no longer sufficient, and it becomes more appropriate to describe light–matter interactions in terms of absorption and scattering.[36]

When an electromagnetic wave interacts with a sub-wavelength particle, the electric field induces a collective oscillation of the electrons within the particle. This oscillating charge distribution gives rise to a secondary electromagnetic field, which is responsible for the scattered light, while energy dissipation within the material leads to absorption. The strength of this response depends on the material properties, the particle geometry, and the surrounding medium.[36] At certain frequencies, the oscillation of the electron cloud becomes resonant, leading to a strong enhancement of the absorption and scattering of the electromagnetic field. This resonance is referred to as a localized surface plasmon resonance (LSPR). **Figure 2.3** illustrates the LSPR of spherical and spheroidal particles, where the anisotropic morphology of the spheroid gives rise to two distinct LSPR modes. In gold and silver nanoparticles, these resonances occur in the visible and near-infrared regions of the electromagnetic spectrum, producing intense colors in both reflected and transmitted light. This phenomenon has been utilized since the Middle Ages in stained glass to create the characteristic luminous atmosphere of

churches and cathedrals throughout Europe.[37]

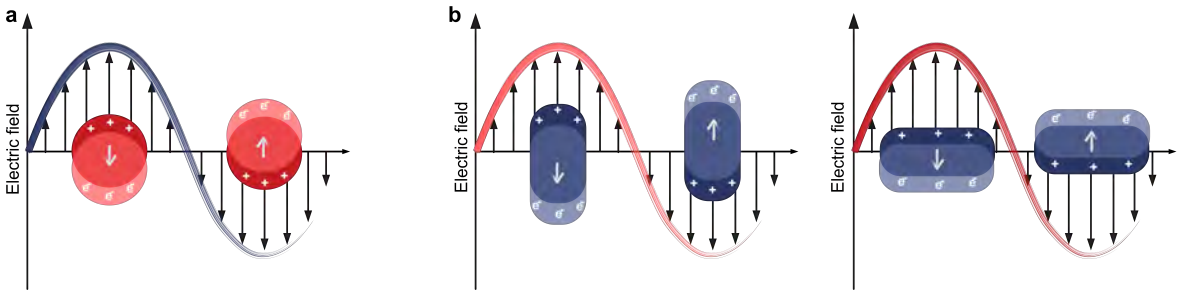

Figure 2.3: Schematic illustration of localized surface plasmon resonance (LSPR), showing the oscillation of the induced surface charges in response to an external electric field. **a** Spherical nanoparticle. **b** Spheroidal (rod-shaped) nanoparticle, exhibiting both longitudinal and transverse LSPR modes at resonance.

In 1908, Gustav Mie developed a theory describing the colors arising from the absorption and scattering of light by small colloidal particles, now known as Mie theory. This theory provides an analytical solution to Maxwell's equations for an electromagnetic plane wave incident on a spherical particle, resulting in an infinite series of vector spherical harmonics that describe the electromagnetic field at any point in space. Mie theory accurately describes light scattering and absorption for spherical particles of all sizes.[33] However, it is not the most intuitive framework for understanding scattering and absorption, as it requires summing an infinite series of multipole contributions. If, instead, the particle diameter is much smaller than the incident wavelength, the light–matter interaction can be described using the quasi-static approximation, which provides a more physically intuitive description of the problem.

2.2.1 Quasi-Static Approximation

If we have a particle much smaller than the wavelength ($a \ll \lambda$) of the applied electromagnetic field, the field across the particle can be assumed to be homogeneous. The resulting charge displacement, and consequently the scattered field, will then follow that of an electric dipole[f]. Hence, all spatial variations within the particle can be neglected.

[f]For wavelengths in the visible regime, the quasi-static approximation is regarded as accurate for particles with a radius smaller than 30 nm.

Spherical Particle

A homogeneous and isotropic spherical particle with radius a is located in a uniform electric field $\mathbf{E}$.[36] The surrounding medium is non-absorbing and homogeneous with a real permittivity $\varepsilon_m = n'^2$ and the complex permittivity of the particle is $\varepsilon = N^2$. The applied electric field $\mathbf{E}$ give rise to the induced dipole moment

$$\mathbf{p}(\omega) = \varepsilon_0 \varepsilon_m \alpha(\omega) \mathbf{E}(\omega), \tag{2.13}$$

where $\alpha(\omega)$ represents the polarizability of the particle, which can be obtained by solving the Laplace equation for the electrostatic case (see the derivation in reference[36]) and then replacing the static permittivity with the frequency dependent one. The result is found to be:

$$\alpha = 4\pi a^3 \frac{\varepsilon - \varepsilon_m}{\varepsilon + 2\varepsilon_m}. \tag{2.14}$$

It follows from **Eq. 2.14** that the resonance condition is given by $\varepsilon = -2\varepsilon_m$, the LSPR mentioned previously.

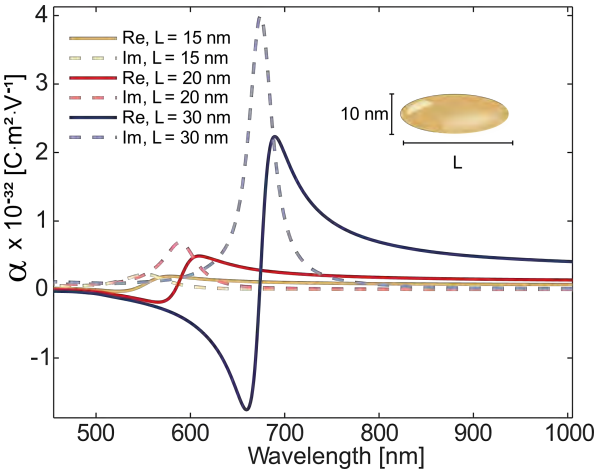

Figure 2.4: Real (solid) and imaginary (dashed) parts of the polarizability α along the long axis (a_1) of a prolate gold spheroid with width 10 nm ($a_2 = a_3 = 5$nm) and different lengths L in water, calculated in the quasi-static approximation using the Johnson and Christy permittivity.[35]

Spheroidal Particle

The quasi-static approximation can also be applied to spheroidal particles and serves as a good first approximation for nanorods. As in the spherical case, the particle dimensions must be much smaller than the wavelength; however, the semi-axes a_1, a_2, and a_3 of the particle must now be considered.[33] For a prolate spheroid (cigar-shaped particle), two of the semi-axes are equal ($a_2 = a_3$), while the third semi-axis is longer ($a_1 > a_2$). The dipole moment for a spheroid (j = 1,2,3) is then given by

$$\mathbf{p}_j = 4\pi\varepsilon_0\varepsilon_m a_1 a_2 a_3 \frac{\varepsilon - \varepsilon_m}{3(\varepsilon_m + L_j(\varepsilon - \varepsilon_m))}\mathbf{E} \tag{2.15}$$

where L_j represent the geometrical factor of the dimensions of the spheroid. For semi-axes a_1, L is

$$L_{a1} = \frac{a_1 a_2 a_3}{2}\int_0^\infty \frac{1}{(a_1^2 + q)f(q)}dq \tag{2.16}$$

with $f(q) = ((a_1^2 + q)(a_2^2 + q)(a_3^2 + q))^{1/2}$. The polarizability for a spheroid becomes

$$\alpha_j = 4\pi a_1 a_2 a_3 \frac{\varepsilon - \varepsilon_m}{3(\varepsilon_m + L_j(\varepsilon - \varepsilon_m))}. \tag{2.17}$$

For any ellipsoid, the geometrical factors satisfy $L_1 + L_2 + L_3 = 1$, and for a sphere, where all axes are equal, $L_{1,2,3} = 1/3$, **Eq. 2.17** reduces to **Eq. 2.14**. In contrast to a sphere, a spheroid supports two distinct plasmon resonances corresponding to oscillations along the semi-minor and semi-major axes (illustrated in **Figure 2.3**).

Since the permittivity is complex, the polarizability is also complex and can be written as $\alpha = \alpha' + i\alpha''$, where α' and α'' are the real and imaginary parts, respectively. **Figure 2.4** shows these components as a function of wavelength for a permittivity $\varepsilon(\omega)$. The imaginary part exhibits a pronounced peak corresponding to the localized surface plasmon resonance, where absorption and scattering are maximized. Near this wavelength, the real part of the polarizability changes rapidly, indicating a phase shift in the dipole response. This behavior is characteristic of a resonant dipole oscillator and occurs when the Fröhlich condition is satisfied, i.e., when $\mathrm{Re}[\varepsilon(\omega)] = -2\varepsilon_m$.[36]

2.2.2 Optical Cross-Sections

Having established the particle polarizability, we now turn to the optical cross sections describing scattering and absorption of sub-wavelength particles. Optical cross sections quantify how efficiently a particle absorbs, scatters, or extinguishes incident electromagnetic radiation and are defined as the ratio of the scattered, absorbed, or extinguished power to the incident power density. This definition results in a quantity with units of area, hence the name *cross section*.

Within the quasi-static approximation, we can also determine the scattering and absorption of light by a nanoparticle analytically. The scattering cross section, σ_{scat}, describes how efficiently a particle scatters light, while the absorption cross section, σ_{abs}, describes how much of the incident light is absorbed by the particle. The extinction cross section quantifies the total loss of intensity of the incident light due to both absorption and scattering, and is given by $\sigma_{\text{ext}} = \sigma_{\text{scat}} + \sigma_{\text{abs}}$. Both σ_{ext} and σ_{scat} can be expressed in terms of the particle polarizability as

$$\sigma_{ext} = kIm\{\alpha(\omega)\} = 4\pi k a^3 Im\left\{\frac{\varepsilon - \varepsilon_m}{\varepsilon + 2\varepsilon_m}\right\} \tag{2.18}$$

and

$$\sigma_{scat} = \frac{k^4}{6\pi}|\alpha(\omega)|^2 = \frac{8\pi}{3}k^4 a^6\left|\frac{\varepsilon - \varepsilon_m}{\varepsilon + 2\varepsilon_m}\right|^2 \tag{2.19}$$

Here, with the wavenumber $k = 2\pi/\lambda_m$.[36] **Figure 2.5** shows the σ_{ext} for a gold sphere and spheroid in water, with varying radius and length, respectively.

Based on the quasi-static approximation, the resonance condition $\varepsilon = -2\varepsilon_m$ appears to depend only on the permittivity of the particle material and the surrounding medium. However, in reality the particle size also plays an important role for the LSPR. As the particle size increases, effects such as retardation and radiative damping cause the LSPR to shift to longer wavelengths. Retardation effects, also referred to as dynamic depolarization, arise because the particle can no longer be considered a point-like oscillating dipole. Instead, the phase of the induced electromagnetic field varies across the particle, resulting in a phase lag between the driving field and the induced dipole moment. This reduces the effective polarizability and lowers the frequency of the dipole oscillation, which causes the LSPR to shift to longer wavelengths. Radiative damping arises from energy loss due to radiation from the oscillating dipole of the particle. As

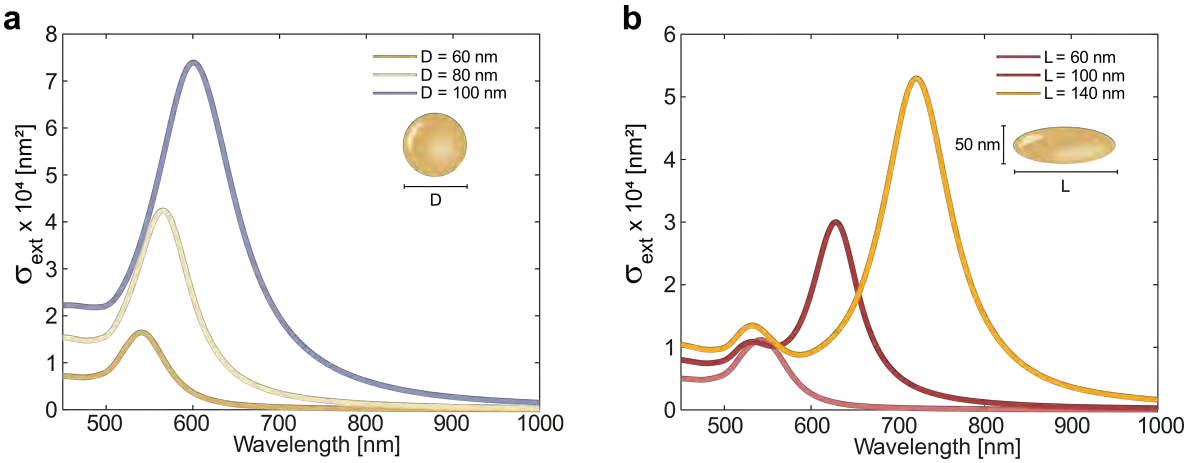

Figure 2.5: Extinction cross-section spectra of gold nanoparticles in water under unpolarized plane-wave illumination. The spectra are calculated using the quasi-static approximation with MLWA corrections for **a** spherical particles with increasing diameter and **b** spheroidal nanorods with a fixed width of 50 nm and increasing length. The relative permittivity of gold was taken from the Johnson & Christy experimental data.[35]

the particle becomes larger, scattering becomes more significant (which can be seen in **Eq. 2.19** with $\sigma_{scat} \propto a^6$) and the radiated energy damps the dipole oscillation, leading to a broadening and reduction of the plasmon resonance.

For small particles, absorption dominates due to Ohmic losses, and most of the incident light energy is converted into heat. This is important for many applications of metallic nanoparticles. For example, gold nanorods have been used for photothermal cancer treatment,[38,39] and nanoparticles have been used to drive Marangoni convection flows,[40,41] where the particle design is optimized to generate as much heat as possible. However, in other applications scattering is instead promoted. This is the case for the work presented in this thesis. In **Paper I**,[28] radiative scattering dominates the optical torque driving the rotation of optically trapped nanorods,[42] while in **Paper II**, we exploit the strong scattering of nanoparticles relative to the background to enable single-particle tracking.[43]

The quasi-static approximation, which we have used to gain intuitive insight into light–matter interactions, does not account for these size-dependent effects. However, it can be extended to include somewhat larger particles (on the order of ∼100 nm) through the modified long wavelength approximation (MLWA).[44,45] The MLWA modifies the polarizability by including dynamic depolarization and radiative damping effects, and is defined as

$$\alpha_{MLWA} = \alpha_j \left(1 - \frac{2}{3} ik^3 \alpha_j - \frac{k^2}{a_j} \alpha_j\right)^{-1}. \tag{2.20}$$

Here, the first term describes the radiative damping, which arises from re-radiation of energy by the induced dipole. The second term accounts for the dynamic depolarization of the radiation across the particle surface due to finite ratio of particle size to wavelength.[46] This dynamic depolarization term causes a red shift in the LSPR as the particle size increases. Nevertheless, this approach is only a good approximation when the particle response is predominantly dipolar.

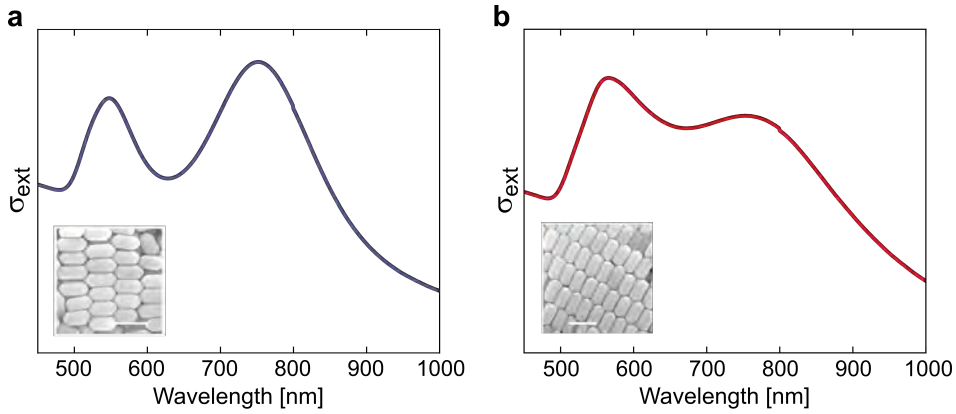

Figure 2.6: Experimental extinction spectra (a.u.) as a function of wavelength for the two nanorod samples used in this work. **a** Nanorods with an average size of 69 × 135 nm. **b** Nanorods with an average size of 98 × 164 nm. Insets show SEM images of the corresponding nanorods with a scale bar of 200 nm.

However, the quasi-static and MLWA models assume simple particle geometries such as spheres or spheroids. The shape of the nanoparticles in this work is deviating a fair bit from an ideal spheroid, as can be seen in **Figure 2.6**, and this significantly affects the plasmonic response of the particles[g]. Furthermore, for larger particles, higher-order modes of the electromagnetic field inside and around the particle can no longer be neglected, and the dipole approximation becomes insufficient. To accurately describe particles with realistic geometries and include all electromagnetic effects such as retardation, radiative damping, and multipolar resonances, numerical methods are required.[47] Common numerical approaches include the finite-difference time-domain (FDTD) method, the finite element method (FEM), and the discrete dipole approxi-

[g]If the quasi-static approximation were used to calculate σ_{ext} for nanorods of the sizes shown in **Figure 2.6**, the resulting spectrum would differ drastically from the measured one.

mation (DDA), all of which solve Maxwell's equations numerically for arbitrary geometries and material distributions. These methods enable calculation of both near-field and far-field optical properties and are therefore widely used for modeling plasmonic nanoparticles with complex shapes and environments.[47]

2.2.3 Light-Induced Heating of Gold Nanoparticles

While the previous section focused on the optical response of plasmonic nanoparticles, it is also important to consider what happens to the absorbed optical energy, which is largely converted into heat through photothermal processes. When metallic nanostructures are illuminated, the incident light excites collective oscillations of the conduction electrons, which generate oscillating currents within the metal. Due to the intrinsic losses of metals at optical frequencies, these currents undergo resistive damping, resulting in the conversion of optical energy into heat. Consequently, the light absorbed by plasmonic nanoparticles is dissipated as heat into the surrounding environment. Near the plasmon resonance wavelength, both absorption and scattering are strongly enhanced, which increases the heat generation and makes photothermal effects particularly important in plasmonic systems.[48]

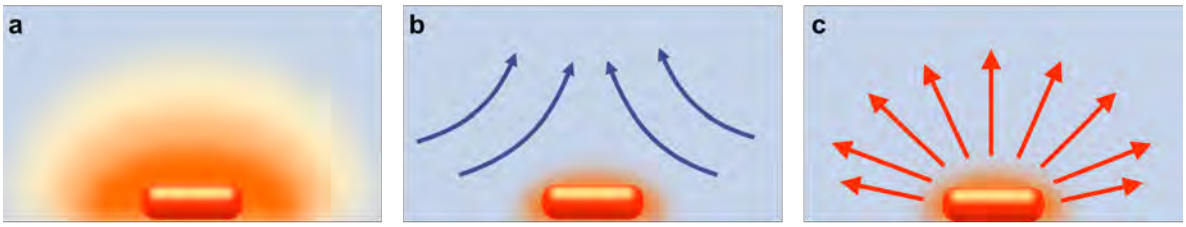

Figure 2.7: Illustration of light-induced heating of a gold nanorod. **a** Heat dissipating via conduction. **b** Heat dissipating via convection. **c** Heat dissipating via thermal radiation.

To simplify the analysis, we consider the case of a very small spherical nanoparticle ($<$ 50 nm). For particles much smaller than the incident wavelength, the electric field inside the particle can be assumed to be uniform, which results in uniform heat generation. Due to the high thermal conductivity of metals, the temperature inside the nanoparticle can therefore be considered uniform. Under light irradiance I, a nanoparticle converts absorbed optical energy into heat, with the generated heat power given by $Q = \sigma_{\text{abs}} I$.[48] Under steady-state conditions, the temperature of a spherical nanoparticle is given by

$$T_{np} = T_{env} + \frac{\sigma_{\text{abs}} I}{4\pi a \kappa}, \tag{2.21}$$

where T_{env} is the temperature of the surrounding environment, a is the particle radius, and κ is the thermal conductivity of the surrounding medium. Outside the nanoparticle, the temperature decreases with distance as $1/r$, into the surrounding medium. The generated heat is dissipated into the surrounding environment primarily through thermal conduction (or thermal diffusion), where thermal energy is transferred through collisions between neighboring atoms or molecules. Another mechanism of heat dissipation is convection, which refers to heat transfer induced by the motion of a fluid. Heating can create density variations in the fluid, which in turn generate fluid motion that transports heat away from the nanoparticle. However, for nanoscale heat sources in liquids, convection is typically weak and does not significantly affect the temperature distribution. A third mechanism is radiative heat transfer, which corresponds to heat dissipation through thermal radiation. However, radiative heat transfer is usually negligible in nanoscale systems compared to conductive heat transfer.[48] **Figure 2.7** illustrates the three different heat transport mechanisms.

3

Optical Trapping of Plasmonic Nanoparticles

Light can be used to manipulate microscopic objects, as the transfer of optical momentum gives rise to forces on matter. This principle forms the basis of optical tweezers, a technique that enables the trapping and manipulation of micro- to nanoscale objects using a tightly focused laser beam.[18–20,49] In 1986, Arthur Ashkin and co-authors reported the first single-beam optical trap,[50] later termed optical tweezers. This work followed Ashkin's earlier demonstration of laser-driven transport and trapping of micron-sized particles in water via momentum transfer.[51] In 1987, Ashkin and co-authors further demonstrated the application of optical tweezers to manipulate single cells and intracellular organelles.[52]

Since their invention, optical tweezers have been widely used to investigate a broad range of biological and biophysical processes, a significance recognized by the awarding of the Nobel Prize in Physics to Arthur Ashkin.[53] Their widespread adoption is partly due to the ability to probe cells and cellular components in real time in a non-invasive manner. Optical tweezers have been employed to study the mechanical properties of DNA,[54] measure forces generated by motor proteins such as kinesin and dynein,[55,56] investigate the viscoelastic properties of the cytoplasm,[57,58] and manipulate single cells to study interaction dynamics and adhesion properties.[52,59]

The work presented in this thesis is similarly concerned with dynamics at the cellular and sub-cellular scale, where the structures of interest are far smaller than the diffraction

limit of light and the motions we wish to resolve are often subtle. Measuring sub-cellular nanomotion therefore requires a tool that can both position a probe with nanometer precision and continuously read out its response in a non-invasive manner. Optical tweezers provide exactly this combination, and when they are used to trap a gold nanorod, the rotational degree of freedom of the particle becomes an additional readout channel that is directly sensitive to the local environment of the rod. This chapter develops the theoretical framework needed to understand how optical trapping and rotation of gold nanorods work in practice.

It begins with an overview of the optical forces governing the system, with particular emphasis on metallic nanoparticles and their description within the dipole approximation. The transfer of angular momentum from light to trapped nanoparticles is then examined. The stochastic motion of optically trapped particles is then considered, including both translational and rotational Brownian motion, followed by a discussion of surface interactions.

3.1 Optical Forces

Radiation pressure arises from the momentum carried by light, enabling photons to exert measurable forces on matter, which forms the physical basis of optical tweezers. In **Chapter 2** we described light as an electromagnetic wave, but light can also be described as photons, the quantum of light. A photon carries momentum $p = \frac{h}{\lambda_0}$, where h is Planck's constant and λ_0 is the wavelength of light. The corresponding photon energy is $E = \frac{hc}{\lambda_0}$. When a photon is normally incident on a surface and reflected (i.e., elastically scattered without energy loss), its energy remains unchanged; however, the direction of its momentum changes, resulting in a recoil force acting on the surface.[60] The power P of an incident light beam corresponds to the energy delivered per unit time and can be expressed as $P = NE$, where N is the number of photons incident per second. The force on the surface can then be understood as the total change in photon momentum per unit time. For perfect reflection, each photon undergoes a momentum change of $2p$, giving a total force $F = \frac{2P}{c}$, which is the maximum force exerted by the beam. For complete absorption, the momentum change is p per photon, yielding $F = \frac{P}{c}$.

Although radiation pressure captures the basic mechanism of momentum transfer from light to matter, optical trapping is achieved by tightly focusing a beam of sufficiently

high power. In this case, the force exerted on a particle is no longer determined solely by the net momentum transfer, but also by the spatial structure of the electromagnetic field. The total force, $\mathbf{F}$, can be decomposed into a *scattering/absorption force*, $\mathbf{F}_{\text{scat/abs}}$, and a *gradient force*, $\mathbf{F}_{\text{grad}}$, illustrated in **Figure 3.1**. The scattering/absorption force is a non-conservative force acting along the propagation direction of the incident light, arising from scattering and absorption processes, and is proportional to the light intensity. In contrast, the gradient force is a conservative force originating from spatial variations in the electromagnetic field, which drives the particle toward regions of higher intensity and enables confinement[a]. For stable three-dimensional trapping, the gradient force must dominate over the scattering/absorption force, which is achieved experimentally by tightly focusing the beam using a high numerical aperture (NA) objective.[60]

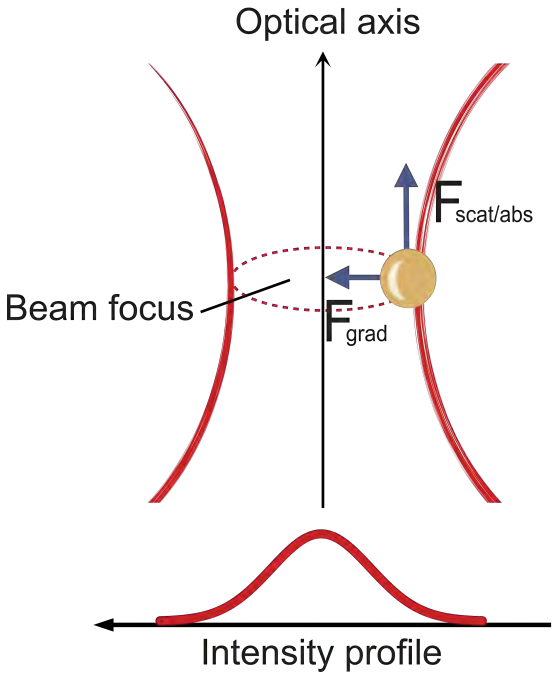

Figure 3.1: An optically trapped particle smaller than the wavelength of light experiences a scattering/absorption force, $\mathbf{F}_{scat/abs}$, that pushes the particle along the direction (optical axis) of the light's propagation, and a gradient force, $\mathbf{F}_{grad}$, that guides it towards the focus, i.e., the area of highest light intensity in the case of a Gaussian beam profile.

For a dielectric particle whose diameter is much larger than the wavelength of light, the forces acting on the particle can be described using ray optics.[61] In this regime, individual light rays are refracted as they enter and exit the particle. As a result,

[a]This applies to particles with a higher refractive index than the surrounding medium.

the outgoing rays propagate in different directions from the incident rays, implying a change in the momentum of the light. By conservation of momentum, this change gives rise to a force on the particle. For a Gaussian beam, the combined effect of these forces produces a restoring force toward the focal point of the trapping laser. For particles much smaller than the wavelength, the optical forces can be calculated using the *dipole approximation*, in which the particle is considered an electric dipole that becomes polarized by the electric field of the trapping laser.[62]

3.1.1 Dipole Approximation

Within this approximation, the induced dipole interacts with the electromagnetic field of the trapping laser and experiences a Lorentz force. The induced dipole moment $\mathbf{p}$ is linearly proportional to the electric field $\mathbf{E}$, such that the total optical force can be decomposed into a gradient and a scattering/absorption component, $\mathbf{F} = \mathbf{F}_{grad} + \mathbf{F}_{scat/abs}$, which can be expressed as follows:

$$\mathbf{F}_{grad}(r) = \frac{\alpha'}{2c\varepsilon_0}\nabla I(r) \tag{3.1}$$

$$\mathbf{F}_{scat/abs}(r) = \frac{\sigma_{ext}}{c}\langle \mathbf{S}(r)\rangle \tag{3.2}$$

where r denotes the position of the particle, $I = \frac{1}{2}c\varepsilon_0|\mathbf{E}|^2$ is the intensity of the light, and $\langle \mathbf{S}\rangle$ is the time-averaged Poynting vector, defined as $\mathbf{S} = \mathbf{E} \times \mathbf{B}$, i.e., the cross product of the electric and magnetic fields.[60,63]

As seen from **Eq. 3.1**, the conservative gradient force can either attract or repel particles within the optical trap. For a particle with positive polarizability, corresponding to a refractive index higher than that of the surrounding medium, the force is directed toward regions of higher intensity. Conversely, a particle with a lower refractive index than the surrounding medium experiences a force directed away from the high-intensity regions.[60]

For plasmonic particles, the polarizability is determined by the relationship between the LSPR and the wavelength of the trapping laser. This can lead to an attractive gradient force when the laser is red-detuned (i.e., at wavelengths longer than the LSPR), and a repulsive force when it is blue-detuned (i.e., at wavelengths shorter than the LSPR).[64] Owing to the large scattering cross-section of plasmonic particles, they are inherently

challenging to trap, especially in the vicinity of their LSPR. To mitigate absorption and scattering effects, the trapping laser is typically detuned from the particle's LSPR, enabling stable three-dimensional confinement.[65] However, if the trapping laser is tuned to the LSPR of the particle, stable trapping can be achieved in two dimensions by balancing the scattering/absorption force with a physical boundary, such as a cover glass, together with repulsive surface forces. This configuration is employed in **Paper I**, where cellular nanomotions are investigated using an optically trapped probe.[28,42,63,66]

3.1.2 Optically Induced Rotation of Nanoparticles

Just as light can transfer linear momentum and exert a force, it can also carry and transfer angular momentum. When a particle modifies the angular momentum of the light field, conservation of angular momentum gives rise to a corresponding optical torque on the particle.[67,68]

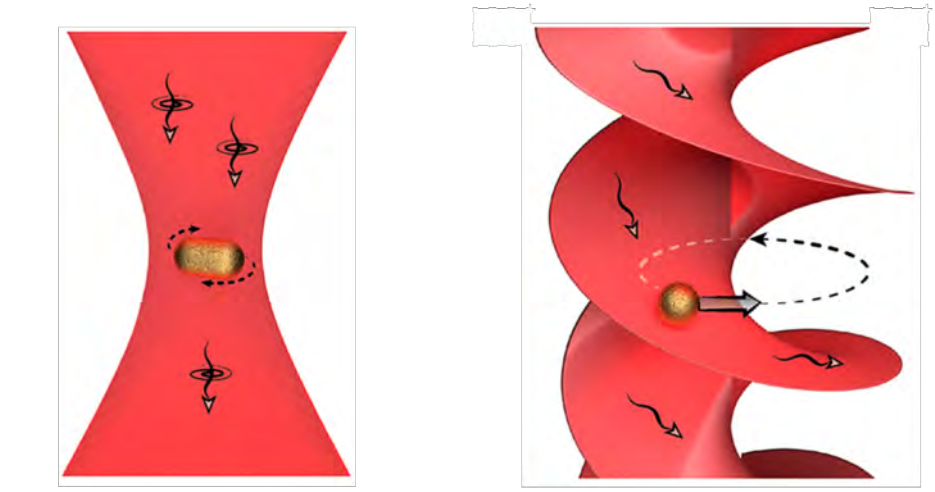

Figure 3.2: Illustration of photon induced rotation of nanoparticles. Spin angular momentum of the circularly polarized laser light is transferred to a nanorod through photon absorption or scattering. Orbital angular momentum is transferred to a nanoparticle through the phase construction of laser beam. Reprinted (adapted) with permission from Ref.[69] Copyright © 2020, American Chemical Society.

The angular momentum of light can be decomposed into two components:[69] *spin* angular momentum, associated with circular polarization, and *orbital* angular momentum, associated with the spatial phase structure of the light field. **Figure 3.2** illustrates

the two types of optical torque acting on a particle. The transfer of spin angular momentum to an optically trapped particle occurs when the particle modifies or absorbs circularly polarized light, and depends on the particle's physical properties such as anisotropy and absorptivity.[70] For anisotropic or birefringent particles, unequal phase delays along different axes alter the polarization state of the light, resulting in a change in its spin angular momentum and a corresponding optical torque on the particle.[71] For circularly polarized light, this torque is non-conservative and independent of the particle's orientation, leading to continuous rotation.

For isotropic particles, spin angular momentum transfer instead occurs through absorption.[68,72] Each photon in a circularly polarized beam carries one unit of spin angular momentum, $\hbar$, oriented along the propagation direction, with the sign set by the handedness of the polarization: positive for left-circularly polarized light and negative for right-circularly polarized light. When such a photon is absorbed by the particle, conservation of angular momentum requires that its spin be transferred to the particle itself, producing a torque about the beam axis.[72] The direction of rotation therefore reverses when the handedness of the polarization is reversed, and linearly polarized light, being an equal superposition of the two circular states, carries no net spin and induces no rotation through absorption.

In contrast, orbital angular momentum drives the trapped particle into a circular orbit around the beam center through the azimuthal component of the scattering force arising from the beam's helical phase structure. If the particle encompasses the entire beam profile, this results in rotation about its center of mass.[70,73–75]

In **Paper I**, we exploit the transfer of spin angular momentum to drive the rotation of plasmonic gold nanorods in an optical trap. Owing to their LSPR, these particles exhibit enhanced light–matter interactions, leading to increased optical torques.[42] When confined in two dimensions against a cover glass, gold nanorods have been shown to exhibit stable rotation in water at frequencies on the order of tens of kHz around its short axis.[42]Unlike isotropic spherical particles,[72,76] the anisotropic nanorod allows angular momentum to also be transferred through resonantly enhanced scattering, which for sufficiently large rods dominates the total optical torque and reduces photothermal heating.[42] The resulting rotational dynamics are governed by the balance between three torques acting on the particle, and the equation of motion for rotation about a single axis reads

$$J\ddot{\varphi}(t) = M_{\text{opt}} + M_f + M_s \tag{3.3}$$

where J is the moment of inertia for the particle and φ is the orientation angle. The optical driving torque is denoted M_{opt}, M_f is the counter acting friction torque from the surrounding media and M_s is the stochastic thermal torque responsible for the particle's rotational Brownian motion, with $\langle M_s \rangle = 0$.[42,63,76] A general expression of the optical torque is

$$M_{opt} = \left\langle \mathbf{p} \times \mathbf{E} \right\rangle \tag{3.4}$$

which describes the torque arising from the interaction between the induced dipole moment $\mathbf{p}$ and the electric field $\mathbf{E}$. The M_{opt} can be calculated analytically if $\mathbf{p}$ can be estimated using the dipole approximation or by using Mie theory for a sphere. If the particle geometry becomes more complex, a numerical approach using Maxwell's stress tensor to calculate the $\mathbf{E}$-field can be used.[77]

The optical driving torque can be decomposed into absorption and scattering contributions, $M_{opt} = M_{scat} + M_{abs}$, where $M_{abs} = \sigma_{abs} \cdot I_{inc}/\omega_0$ for a light intensity of I_{inc}, photon energy $\hbar\omega_0$ and particle absorption cross section σ_{abs}.[42] The scattering component of the total torque can be calculated as $M_{scat} = M_{opt} - M_{abs}$.

The friction torque M_f for a sphere or spheroidal particle at low Reynolds numbers can be expressed as

$$M_f = -\pi\eta L^3 \dot{\varphi} g, \tag{3.5}$$

where $\eta = \eta(T)$ is the temperature-dependent dynamic viscosity of the surrounding medium, $\dot{\varphi}$ is the angular velocity, L is the length of the particle and g is the geometrical factor of the trapped particle.[78] For a sphere $g = 1$, but for a spheroid, the geometrical factor depends on its eccentricity ξ_0 and is calculated via

$$g = \frac{-\varepsilon_e^3}{-2\xi_0 + (\xi_0^2+1)\hat{\xi_0}} \cdot \left[2\xi_0(\xi_0^2-1)tanh^{-1}\left(\frac{1}{\xi_0}\right) + \frac{-4+8\xi_0^2-3\xi_0(\xi_0^2-1)\hat{\xi_0}}{3}\right], \tag{3.6}$$

where $\xi_0 = \frac{1}{\varepsilon_e} = \frac{1}{\sqrt{1-\left(\frac{b}{a}\right)^2}}$, with a and b being the semi-major and -minor axis of the particle and $\hat{\xi_0}$=$\ln\left(\frac{\xi_0+1}{\xi_0-1}\right)$.

At steady state, when M_{opt} is counterbalanced by M_f, the average rotation frequency of the particle can be expressed as[42]

$$f_{avg} = \frac{M_{opt}}{2\pi^2\eta g L^3} = \frac{M_{opt}}{2\pi\gamma_r}, \tag{3.7}$$

where $\gamma_r = \pi\eta g L^3$ and is called the rotational friction coefficient. The thermal stochastic torque M_s also affects the rotation of the particle and increases in strength with increasing friction and temperature.[42,63,76]

3.2 Stable Trapping and Trap Stiffness

For particles stably trapped near the focus of the beam, the force field can be linearized around the equilibrium position.[60] When the particle is displaced from this position, a restoring force acts to return it to the trap center. For small displacements, this force is approximately proportional to the displacement and can therefore be described by Hooke's law as

$$\begin{cases} F_x \approx -\kappa_x(x - x_{\mathrm{eq}}), \\ F_y \approx -\kappa_y(y - y_{\mathrm{eq}}), \\ F_z \approx -\kappa_z(z - z_{\mathrm{eq}}) \end{cases} \tag{3.8}$$

where, $[x, y, z]$ is the particle's position, $[x_{eq}, y_{eq}, z_{eq}]$ is the equilibrium position and, κ_x, κ_y and κ_z are the optical spring constants, also referred to as the *trap stiffness*. In this regime, the optical trap can be described as a three-dimensional potential well that is separable into three harmonic oscillators, one for each spatial direction $i = x, y, z$:

$$U(r_i) = \frac{1}{2}\kappa_i r_i^2. \tag{3.9}$$

Stable trapping occurs when the potential well $U(r)$ is much deeper than the thermal energy k_BT. A stability criterion for a trapped particle can be estimated by $\sim exp[-U(r)/k_BT] \ll 1$, where k_B is Boltzmann's constant and T is the absolute temperature.[50,60] In the 2D trapping configuration used in **Paper I**, axial confinement is instead provided by the cover glass and surface forces (**Section 3.3**), so only the in-plane stiffnesses κ_x and κ_y are relevant to the trap dynamics.

3.3 Brownian Motion

Although the optical forces confine the particle to a small volume, it is never completely at rest. Instead, the particle undergoes continuous fluctuations within the optical trap due to *Brownian motion* (**Figure 3.3**). This erratic motion arises from constant collisions with molecules in the surrounding fluid, which themselves move due to their thermal energy. Consequently, such motion persists even at thermodynamic equilibrium in the absence of external perturbations.[79] The Brownian motion of a particle can be described by adding a stochastic force ($\chi(t)$) to Newton's equation of motion,[60] resulting in the Langevin equation for *translational* Brownian motion as

$$m\ddot{\mathbf{r}}(t) + \gamma_t\dot{\mathbf{r}}(t) = \chi(t) \tag{3.10}$$

where m is the mass of the particle and γ_t is its friction coefficient. For micro- to nanoscale particles, the motion is typically in the low Reynolds number regime[b]. In this case, γ_t can be expressed using Stokes' law for a spherical particle of radius a as $\gamma_t = 6\pi\eta a$, where η is the dynamic viscosity of the fluid, which can be described by an Arrhenius-type equation.[76,80] The stochastic force $\chi(t)$ is not correlated with the particle position and has a zero mean, $\langle\chi(t)x(t)\rangle = 0$ and $\langle\chi(t)\rangle = 0$.

If a particle is subjected to an external force, such as an optical force generated by optical tweezers, the Langevin equation becomes

[b]This means that inertial forces are negligible compared to viscous forces, so the acceleration term in the Langevin equation can be dropped. In this overdamped limit, the particle's displacement is determined by the instantaneous balance between drag and the stochastic force.[60]

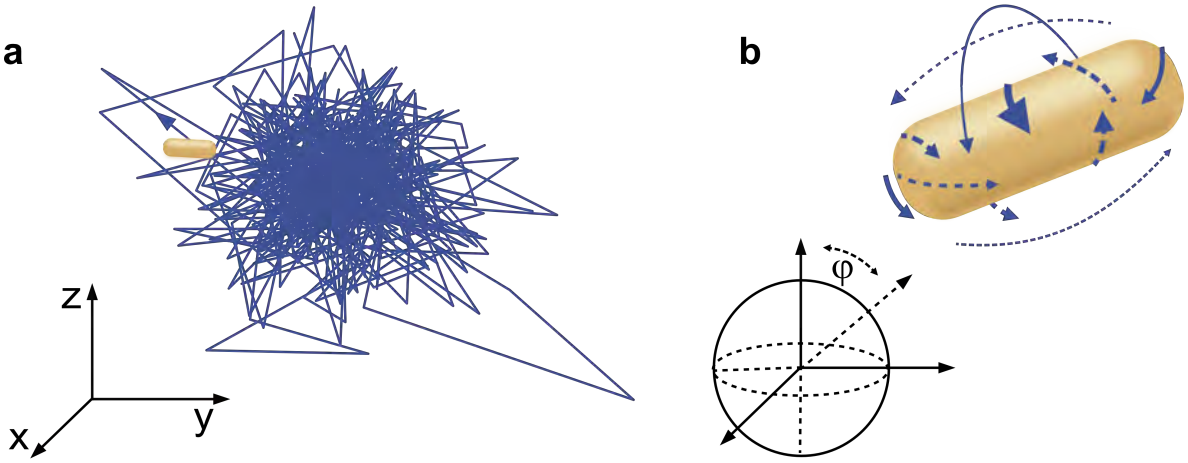

Figure 3.3: Illustration of translational and rotational Brownian motion. **a** Translational Brownian motion, where the particle's position changes over time. **b** Rotational Brownian motion, where the particle's orientation changes over time.

$$\dot{\mathbf{r}}(t) = \frac{1}{\gamma_t}\mathbf{F}(r) + \sqrt{2D_t}W(t). \tag{3.11}$$

Here, the term $W(t)$ represents white noise with an intensity of $2D_t$, where $D_t = k_B T/\gamma_t$ is the diffusion coefficient.[60] As discussed above, the acceleration term in **Equation 3.10** is dropped, as the speed of the object is solely determined by the forces acting on it in the moment.[7,60]

In addition to translational Brownian motion, a particle also experiences *rotational* Brownian motion. This phenomenon occurs due to collisions with surrounding molecules, causing the particle to randomly change its orientation. Rotational Brownian motion is particularly important when trapping non-spherical particles, such as rods or ellipsoids, as the rotational diffusion coefficient varies along different axes of the particle. The rotational Brownian motion can also be described by a Langevin equation, but in this case, it includes an externally applied torque M_{ext},

$$\dot{\varphi}(t) = \frac{M_{ext}}{\gamma_r} + \sqrt{2D_r}W(t), \tag{3.12}$$

where, φ is the rotation angle of the particle and γ_r and $D_r = k_B T/\gamma_r$ are the rotational friction coefficient and diffusion coefficient of the rotational motion, respectively.[42,60,81]

3.3.1 Hot Brownian Motion

As discussed in **Chapter 2**, laser irradiation can lead to significant heating of plasmonic particles due to Ohmic losses. As a result, the Brownian motion described above, which assumes thermal equilibrium in a homogeneous environment, is insufficient to describe the particle dynamics. The heating of the particle induces both temperature and viscosity gradients in the surrounding fluid, giving rise to a non-equilibrium regime. In this case, the particle undergoes so-called *hot Brownian motion*, which requires additional considerations to accurately describe its dynamics.[82–84]

A particle maintained at a temperature higher than its surroundings establishes a radially symmetric temperature profile in the surrounding fluid, which can be treated as stationary in the particle's comoving frame.[82–84] This is justified by the fact that heat conduction occurs on a much faster timescale than the particle's Brownian motion. While the system is in a complex nonequilibrium state, its dynamics can often be well described by an effective Markov theory that treats the particle as if it were in a homogeneous medium at specific effective temperatures and viscosities. However, the effective quantities differ between translational and rotational Brownian motion, because rotational motion couples more strongly to the fluid immediately adjacent to the particle surface, where the temperature is highest, and therefore experiences a higher effective temperature than translational motion.[81,84,85]

Hot Brownian motion has been experimentally studied by laser heating nanoparticles and tracking their translational and rotational dynamics to extract effective temperatures and friction coefficients.[81,85,86] These measurements reveal a hierarchy of temperatures: the translational effective temperature lies above the bulk fluid temperature, the rotational effective temperature higher still, and the particle surface temperature highest of all.

3.4 Surface Interaction and Trapping in 2D

In the trapping system used in **Paper I**, the particle is confined in two dimensions, as the enhanced scattering/absorption force along the beam propagation direction overcomes the axial gradient force. As a result, the particle is pushed toward the cover-glass surface, where surface interactions must be considered. The scattering/absorption force is counterbalanced by Coulomb repulsion (electrostatic forces) arising from the overlap

of the electric double layers (EDLs) of the nanoparticle and the surface.[66]

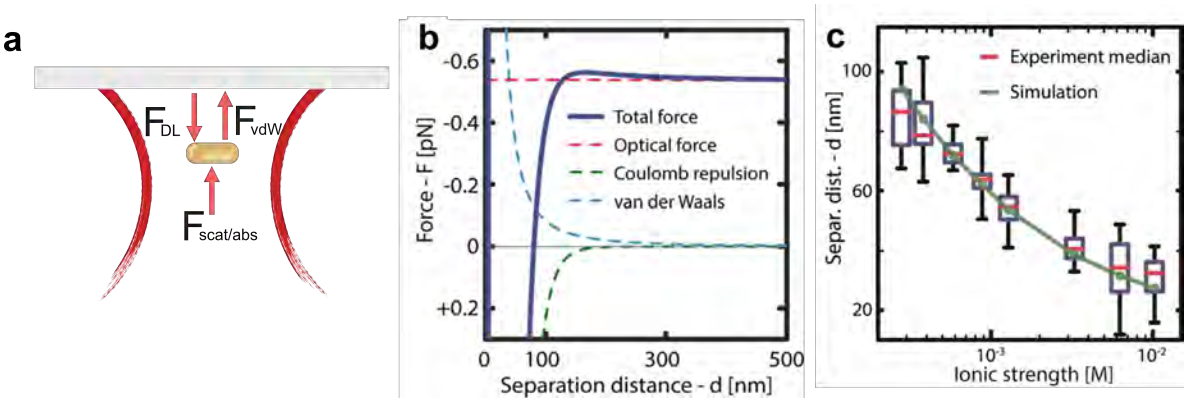

Figure 3.4: **a** A plasmonic nanorod is pushed toward the cover glass by the scattering/absorption force ($\mathbf{F}_{scat/abs}$), balanced by double-layer repulsion ($\mathbf{F}_{DL}$); at short distances, van der Waals attraction ($\mathbf{F}_{vdW}$) becomes significant. **b** Total axial force and its components, estimated from theoretical models, shown along the optical axis and decomposed into individual contributions. **c** Surface separation vs. ionic strength (5.6 mW) from experiment and Brownian dynamic simulations (varying Debye length; log x-scale). Red bars/boxes/whiskers show median, IQR, and range. Reprinted (adapted) with permission from Ref.[66] Copyright © 2019, American Chemical Society.

Colloidal nanoparticles, such as those used in this work, carry a surface charge that attracts a surrounding cloud of counterions. The resulting EDL consists of a *Stern layer*, composed of adsorbed ions at the nanoparticle surface, and a *diffuse layer*, an atmosphere of ions of opposite net charge extending into the surrounding liquid.[4,87] When two similarly charged particles (or a nanoparticle and a surface, as in our case) approach each other, the overlap of their electric double layers (EDLs) gives rise to a repulsive force due to osmotic and electrostatic interactions. A standard way to characterize the surface charge of a nanoparticle is through its zeta potential, defined as the electrostatic potential at the shear plane[c] separating the bound ion layer from the bulk liquid.[4,87]

At sufficiently short separations, however, attractive van der Waals (vdW) forces become significant and can overcome the electrostatic repulsion, potentially leading to particle aggregation. vdW forces are a result of the interaction of induced, instantaneous, or permanent dipoles found in the interatomic bonds of nanoparticles.[87] **Figure**

[c]This plane is defined as the specific distance from the particle's surface where ions are no longer bound to the particle and instead move with the bulk liquid.[87]

3.4 b, shows the magnitudes of the different force components along the optical axis for an optically trapped gold nanoparticle.[66]

The DLVO theory can be used to predict the stability of a colloidal system by superimposing the attractive vdW forces and the repulsive electrostatic forces.[4] For example, it can be used to estimate how electrostatic repulsion is reduced with increasing ionic strength, and thereby determine the conditions under which aggregation occurs. This is particularly important for systems involving nanoparticles in biological environments, which typically exhibit high ionic strengths.

Figure 3.4c shows the distance between the trapped particle and the surface as a function of ionic strength (salt concentration) of the surrounding liquid. As the ionic strength increases, the electric double layer becomes more strongly screened, causing the particle to move closer to the surface. To prevent aggregation in such environments, surface modifications can be employed, for example by coating the particle with a polymer layer.[87]

4

Gold Nanorods in Biological Environments

Translating a method from a well-controlled physical environment to a biological one introduces a new set of constraints. Cells and their surrounding media are heterogeneous, crowded, and active. Any nanoparticle introduced into such a setting is immediately modified by its interactions with biomolecules. If internalized, it is further subjected to active intracellular processes. For gold nanorods, the optical properties (**Chapter 2**) and mechanical response in an optical trap (**Chapter 3**) characterized so far are therefore only a starting point. Despite this complexity, gold nanorods have proven remarkably versatile in biomedical contexts, where their tunable optical response is exploited for imaging, drug delivery, and antibacterial materials. Realizing this potential, however, requires understanding how the surrounding environment shapes their behavior — through functionalization, protein binding in the surrounding medium, and, when applicable, cellular uptake and trafficking.

This chapter first presents examples of biomedical applications of gold nanorods. It then turns to their behavior in biological media, covering colloidal stability in cell culture media, surface functionalization strategies, and protein corona formation in serum. Because these factors govern nanoparticle–cell interactions and influence cellular uptake, the final section discusses intracellular transport mechanisms and how particle motion inside cells can be characterized.

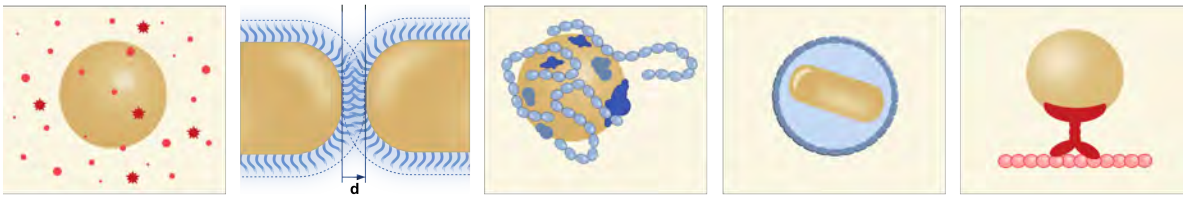

Figure 4.1: Illustrations of key processes affecting nanoparticles in biological environments. From left to right: colloidal aggregation in biological media; steric stabilization by surface-tethered polymers, where d denotes the minimum approach distance; protein corona formation through adsorption of serum proteins onto the nanoparticle surface; encapsulation of a rod-shaped nanoparticle within an endosomal vesicle following cellular uptake; and intracellular transport.

4.1 Gold Nanorods for Biological Applications

Gold nanoparticles have been used in biological applications for several decades, owing to their controllable size and shape, tunable physicochemical properties, chemical stability, and relatively good biocompatibility.[88] Their surfaces can additionally be functionalized with a wide range of biomolecules, enabling targeted delivery and controlled interactions with biological systems. A central reason for their broad use, however, is the LSPR introduced in **Chapter 2**, which gives gold nanoparticles their strong optical response and an enhanced electromagnetic field near the particle surface. For spherical particles, the LSPR lies in the visible spectral range, whereas gold nanorods exhibit two plasmon modes, with a longitudinal mode that can be tuned toward the near-infrared (NIR) region by increasing the aspect ratio. This spectral range coincides with the biological optical window, where absorption and scattering in tissue are relatively low and light can therefore penetrate deeper.[89] Together with their functionalizable surface, this tunable optical response makes gold nanorods particularly attractive for in vivo imaging and therapeutic applications.

Owing to their tunable optical properties and strong plasmonic response, gold nanorods are widely used in bioimaging, both as standalone imaging agents and as contrast enhancers for techniques such as fluorescence and Raman imaging.[90] When used as imaging agents, the nanoparticles are injected into the bloodstream and circulate throughout the body. They can either act as non-targeted agents — relying, for example, on passive accumulation in tumors through the enhanced permeability and retention (EPR) effect[91] — or be functionalized with targeting ligands to actively reach specific tissues or organs.[90] Gold nanorods have been used, for instance, in two-photon luminescence

imaging to track single nanorods flowing through blood vessels in mouse ears,[92] and in photoacoustic molecular imaging to enhance contrast in cancer tumors.[93]

Gold nanorods have been extensively investigated for therapeutic applications, particularly in photothermal cancer therapy, where their strong optical absorption enables efficient conversion of light into localized heat for tumor ablation.[38,94,95] In addition to photothermal therapy, gold nanorods have been explored for targeted drug delivery, where they act as drug carriers and have been shown to increase therapeutic efficiency compared to drugs administered without nanorod carriers.[96] Furthermore, gold nanorods can serve as activation agents for drug release via photothermal conversion, where irradiation-induced heating triggers controlled drug release from nanocarrier systems.[97]

Beyond cancer treatment, their photothermal conversion has also been applied for antibacterial purposes, where near-infrared-induced heating can kill bacteria and disrupt biofilms, including drug-resistant strains.[98,99] This effect has been used in implant coatings to prevent bacterial adhesion and treat implant-associated infections.[100]

Realizing this potential is not straightforward, as nanoparticles introduced into a biological environment encounter complex interactions that can alter their behavior and fate. The following sections address the central factors that determine their success: colloidal stability, surface functionalization, protein corona formation, and interactions with cells.

4.2 Surface Modifications for Increased Biocompatibility and Stabilization

Biological environments, such as cell culture medium (CCM), can strongly affect the stability of colloidal gold nanorods due to their complex chemical composition. CCM is a buffered solution designed to support living cells and contains essential components such as nutrients (amino acids, vitamins, inorganic salts, and glucose), growth factors, hormones, and pH buffers, with the exact composition varying depending on the cell line. These components directly influence the stability of gold nanorods in solution: processes such as protein adsorption or compromised surface functionalization can promote particle aggregation. In addition, the high ionic strength of CCM screens electrostatic interactions, thereby suppressing the repulsive forces between like-charged

nanorod surfaces and further increasing the likelihood of aggregation.[87] Consequently, chemical modification of the nanorod surface is required to ensure stability under such conditions.

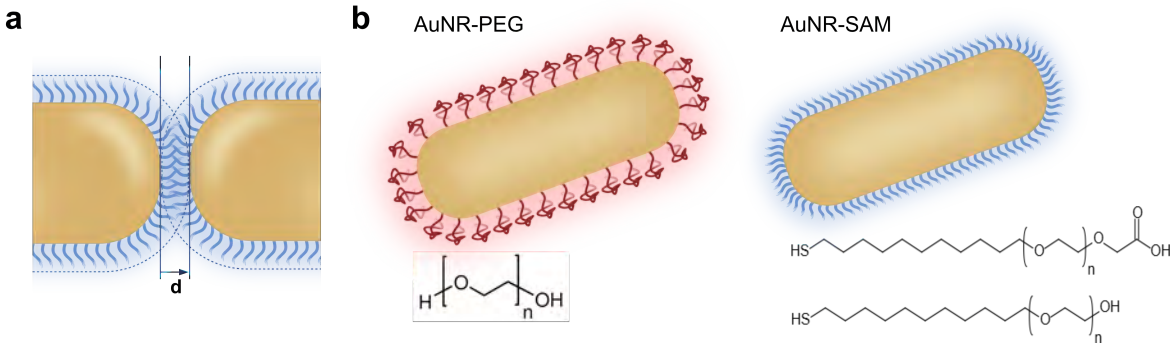

Figure 4.2: Surface functionalization of nanoparticles serves to improve colloidal stability, reduce non-specific protein adsorption, and modulate cellular uptake and intracellular routing. **a** Schematic illustration of steric stabilization between two colloidal particles coated with surface-tethered polymers, where d denotes the minimum approach distance set by the polymer layer. **b** Schematic of gold nanorods (AuNR) functionalized with thiolated poly(ethylene glycol) (PEG, left) and with hydroxyl- (OH) or carboxyl- (COOH) terminated alkanethiol self-assembled monolayers (SAM, right). Chemical structures of the corresponding ligands are shown below each schematic.

To mitigate these effects, appropriate ligand coatings can shield the nanorod surface and provide stabilization mechanisms that remain effective under the high ionic strength conditions of cell culture media. Under such conditions, steric stabilization is the most common strategy for maintaining stability of colloidal gold nanorods (**Figure 4.2a**).[87] Steric stabilization arises from polymeric functionalization of the nanorod surface and does not rely on electrostatic interactions. Instead, it ensures colloidal stability through repulsive forces generated when surface-bound polymer layers overlap and become compressed as particles approach each other. This polymeric layer physically prevents the nanorods from coming into sufficiently close contact for attractive vdW forces to induce aggregation.[87,101]

Since surface chemistry strongly influences protein adsorption, cellular interactions, and nanoparticle uptake, controlling the surface functionalization provides a way to tune nanoparticle behavior in biological environments. In this work, different ethylene-glycol-based surface coatings were used to control protein adsorption and nanoparticle–cell

interactions, ranging from protein-resistant surfaces to surfaces that promote protein corona formation and cellular uptake.

Surface chemistry also governs cytotoxicity.[102] In gold nanorod synthesis, cetyltrimethylammonium bromide (CTAB) is commonly used as a stabilizing agent, but it is highly cytotoxic and must therefore be replaced or covered by other surface ligands before biological experiments can be performed.[103] Two common approaches are coating the nanorods with poly(ethylene glycol) (PEG) or with self-assembled monolayers (SAMs) of alkanethiols.[104,105] Both are biocompatible, weakly negatively charged, and effective at suppressing non-specific protein adsorption, but they differ in length, structure, and the way they pack on the gold surface. The terminal group of either coating can additionally be tuned to introduce different chemical functionalities, such as hydroxyl, methoxy, or carboxyl groups, enabling control over surface charge and further conjugation.[105]

In **Paper I**, the aim was to prevent nanoparticle binding to cells. This was achieved using gold nanorods functionalized with a hydroxyl-terminated oligo(ethylene glycol) alkanethiol self-assembled monolayer (HS-$(CH_2)_{11}EG_4OH$, hereafter SAM-OH), a neutral coating known to resist nonspecific protein adsorption.[106] In **Paper II**, we instead investigated whether surface functionalization influenced intracellular transport of the nanoparticles. For this purpose, PEGylated particles were compared with particles functionalized with the corresponding carboxyl-terminated alkanethiol (HS-$(CH_2)_{11}EG_6$ COOH, SAM-COOH) (**Figure 4.2b**). The negatively charged terminal group of SAM-COOH promotes protein adsorption and protein corona formation, which in turn influences cellular interactions and intracellular trafficking.

The contrasting behavior of these coatings arises from fundamental structural differences between SAMs and PEG on the nanoparticle surface. SAMs are known for their very high grafting density.[105] The alkyl chains attract one another through van der Waals forces and pack into a tight, ordered lattice. On top of this alkyl lattice, the ethylene glycol oxygens form hydrogen bonds with water, creating a tightly bound hydration shell that prevents proteins and other molecules from reaching the gold surface.[105] PEG chains are much longer but their hydrophilic segments repel one another in water, so the grafting density is lower than for an alkanethiol SAM. Instead of a dense, ordered lattice, PEG forms a soft, hydrated brush whose protein resistance comes from steric and osmotic repulsion as approaching proteins compress and dehydrate the chains.[104,105,107]

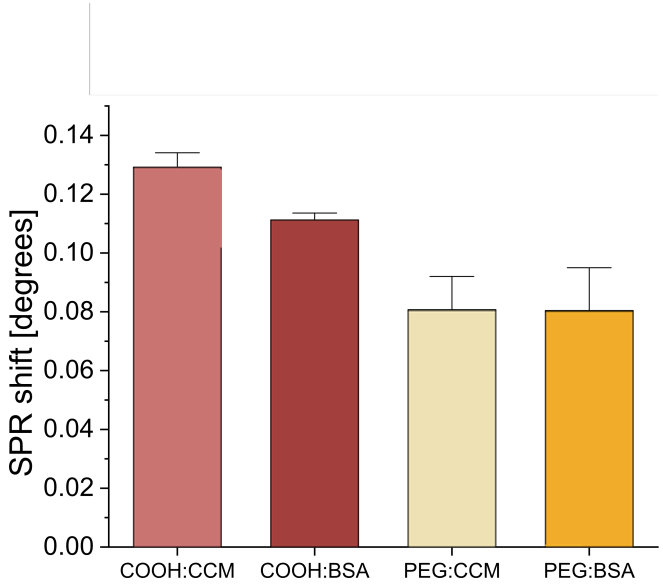

Figure 4.3: A shift in the surface plasmon resonance (SPR) signal reflects mass binding to the surface and is therefore a direct measure of non-specific adsorption of biomolecules. SPR shift for different surface functionalizations: protein adsorption measured for 5 kDa polyethylene glycol (PEG) and SAM–COOH (COOH) functionalized surfaces in cell culture medium (CCM) and bovine serum albumin (BSA). COOH-functionalized surfaces are shown in red and PEG-functionalized surfaces in beige/yellow. Bars represent the mean adsorption response, and error bars indicate the outlier threshold (1.5× interquartile range, Tukey method).

To probe how the two surface functionalizations interact with biomolecules, we used SPR to measure adsorption on SAM-COOH and PEG surfaces under two contrasting conditions: a single-protein reference (1 mg/mL bovine serum albumin, BSA) and a complex biological environment (cell culture medium, CCM). **Figure 4.3** shows the SPR shift for SAM-COOH and PEG surfaces exposed to two different protein environments: cell culture medium (CCM) and bovine serum albumin (BSA). Both surface coatings show protein adsorption in both environments, confirming that no coating is entirely non-fouling under these conditions. A clear difference between the two coatings is nevertheless evident: SAM-COOH produces a larger SPR shift than PEG in both solutions, indicating a greater amount of adsorbed protein. The higher adsorption on SAM-COOH is attributed to its negatively charged terminal group, which electrostatically attracts positively charged residues on proteins and promotes adsorption. In contrast, the neutral PEG brush resists protein adsorption through its hydrated, sterically repulsive layer, resulting in the lower SPR response observed here.

4.2.1 Protein Corona

While the SPR measurements were performed on flat surfaces, the same adsorption processes occur on nanoparticles in biological media, where they lead to the formation of a protein corona (PC) — a layer of biomolecules that assembles on the nanoparticle surface and significantly influences how nanoparticles are recognized, processed, and internalized by cells.[108] The PC is often divided into two subcategories, the hard corona and the soft corona. The hard corona consists of proteins that are tightly bound directly to the nanoparticle surface, whereas the soft corona is composed of more loosely bound proteins that interact with proteins in the hard corona.[108] This distinction is largely operational, however, since the hard corona is typically defined as the proteins remaining after washing or centrifugation, meaning the classification depends partly on the measurement method.[109] PC formation is still an active area of research, and the structure of the corona is not yet fully understood. While some studies describe the corona as a monolayer[110] of adsorbed proteins, others report a multilayer structure consisting of a hard corona and multiple soft corona layers.[111] Furthermore, several studies have shown that the proteins present in the hard and soft corona are not necessarily different protein species.[112] Instead, the key factors determining whether a protein resides in the hard or soft corona are its binding affinity to the nanoparticle surface and its residence time within the corona.

The composition and architecture of the protein corona depend on the biological environment — protein concentration, exposure order, pH, ionic strength, and flow conditions all play a role[108] — but also, and equally importantly, on the intrinsic physicochemical properties of the nanoparticles themselves, such as size, shape, surface charge, and surface functionalization.[88]

Surface chemistry is particularly influential. Surface charge affects the binding affinity, thickness, and composition of the protein corona. For example, gold nanoparticles with either positive or negative surface charge were found to bind a wider range of proteins in human plasma compared to uncharged particles.[113] Surface coatings sets the dominant interaction mode - including steric repulsion, hydrophobic interactions, and ligand–receptor recognition[88] - and therefore determines whether a nanoparticle promotes or inhibit nonspecific protein adsorption.[114] Hydrophilic PEG coatings are widely used to reduce nonspecific adsorption due to steric and hydration repulsion, giving them so-called stealth properties. Despite this, PEGylated nanoparticles still

form a PC in biological environments, and this residual corona can itself mediate cellular recognition and uptake.[115] Other coatings behave very differently: citrate provides only weak electrostatic stabilization and is easily displaced or destabilized in high-ionic-strength media,[87] poly(vinylpyrrolidone) (PVP) coatings can lead to higher protein adsorption, and thiol-based ligands such as glutathione can be displaced by proteins, resulting in strong protein binding to the nanoparticle surface.[116]

Particle size is a second key parameter.[88] For example, studies on negatively charged poly(acrylic acid) functionalized gold nanoparticles have shown that proteins exhibit higher binding affinity and slower dissociation rates as particle size increases from smaller (7 nm) to larger (22 nm) nanoparticles.[117] The thickness and architecture of the corona are also size-dependent:[118] particles larger than 80 nm, substantially bigger than most proteins, can accommodate multilayer coronas, intermediate particles (12–80 nm) typically form a single protein layer, and very small particles (<7 nm) may not be fully covered at all. Shape plays a comparably important role by setting the available contact area and the steric environment for approaching proteins.[88] This is particularly relevant for the gold nanorods used in this thesis: in a direct comparison of carboxy-PEG-functionalized gold nanorods and nanostars, the nanostars were found to form a thicker protein corona with a distinct protein composition relative to the nanorods.[119]

4.3 Nanoparticle Internalization Pathways and Intracellular Fate

The first interaction a nanoparticle has with a cell is with the outer plasma membrane. Through contact with membrane components such as proteins, lipids, and receptors - often mediated by the protein corona discussed above - the nanoparticle is subsequently internalized, almost exclusively via endocytosis.[120,121] Several endocytic pathways can contribute to nanoparticle uptake, including phagocytosis, macropinocytosis, clathrin-mediated endocytosis (CME), caveolae-mediated endocytosis, and clathrin- and caveolae-independent endocytosis (CIE)[120,121] (**Figure 4.4**). Which of these pathways a given nanoparticle uses depends on its size, shape, and surface chemistry, but also on the cell type involved, since not all cells express the full set of endocytic machinery.[120,121] Some cells, for example, lack caveolae and must therefore internalize nanoparticles through the remaining pathways.[120,121] The particular route taken is im-

portant because it determines the intracellular fate of the nanoparticle - which vesicles it traffics through, whether it reaches the lysosome, and how long it resides inside the cell.[122,123]

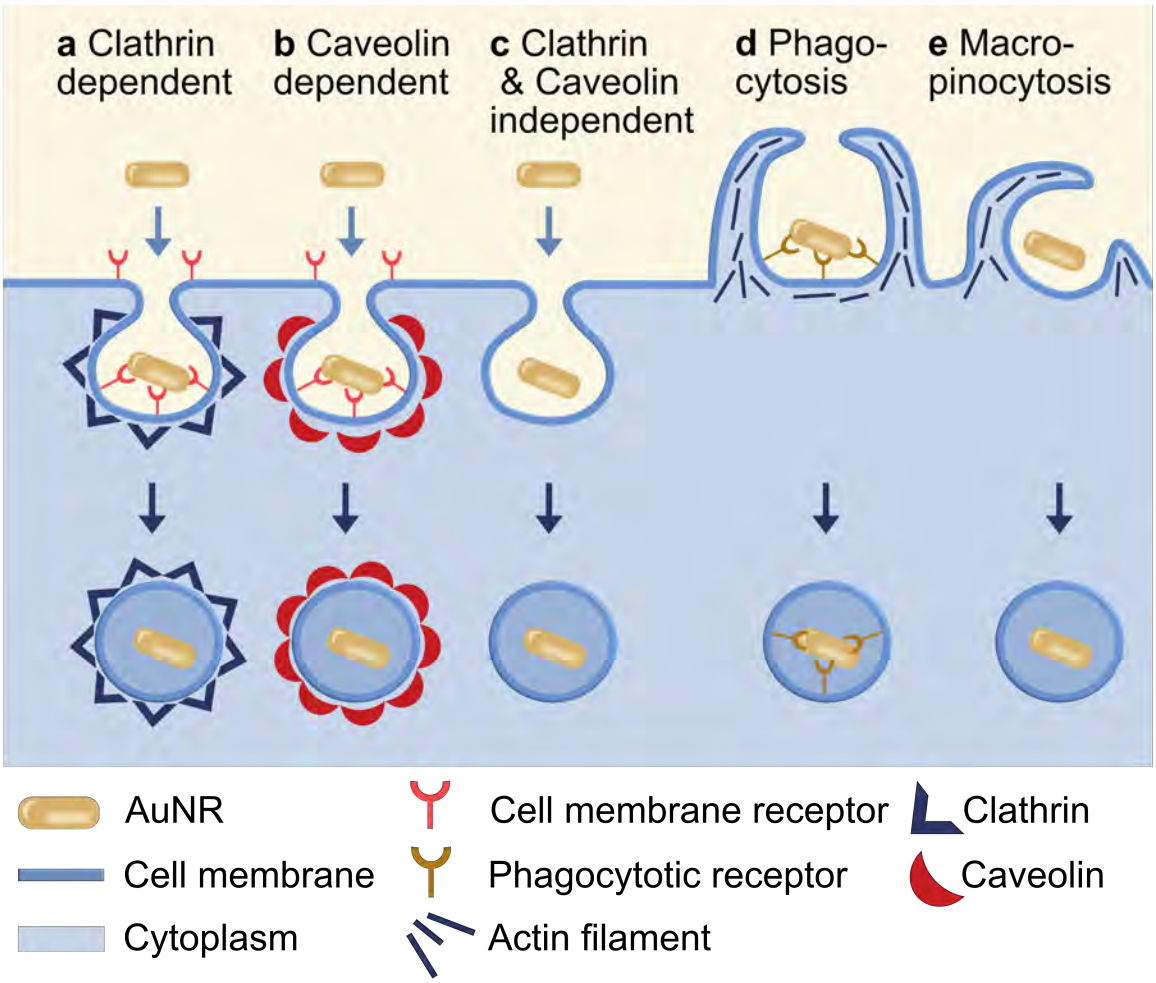

Figure 4.4: Schematic illustration of the five endocytosis pathways by which nanoparticles enter cells: **a** clathrin-dependent endocytosis, **b** caveolin-dependent endocytosis, **c** clathrin- and caveolin-independent endocytosis, **d** phagocytosis, and **e** macropinocytosis. The pathway followed depends on factors such as nanoparticle size, shape, and surface chemistry, as well as cell type.

Clathrin-mediated endocytosis (CME) is one of the most important pathways for nanoparticle uptake and is also responsible for the regulated internalization of surface receptors and nutrients, including iron uptake via the transferrin receptor.[124] CME is named after clathrin, the main structural protein involved: clathrin triskelions assemble into a lattice of hexagons and pentagons, forming a polyhedral coat around forming vesicles that increase membrane curvature.[125] The resulting clathrin-coated vesicles (CCVs)

range from approximately 50 to 200 nm in diameter, with the exact size depending on cargo and cell type — from 50 nm vesicles at chemical synapses to 120–150 nm vesicles in epithelial cells.

Caveolae-mediated endocytosis is another common route of nanoparticle internalization. Caveolae are flask-shaped invaginations of the plasma membrane, 50–100 nm in diameter, found in many mammalian cell types.[120,121] Beyond cargo internalization, they contribute to signal transduction, transcytosis, lipid regulation, membrane-protein trafficking, and membrane-tension homeostasis. In cells lacking functional clathrin or caveolae, internalization can still proceed via clathrin- and caveolae-independent endocytosis (CIE). This pathway does not rely on a dedicated coat protein and is instead driven by specific lipid compositions, typically enriched in cholesterol.[126]

Macropinocytosis is an actin-dependent, non-selective pathway in which the cell engulfs large volumes of extracellular fluid through membrane ruffles, forming vesicles (macropinosomes) that can internalize micron-sized particles.[127] It can be constitutive, occurring continuously as part of normal cell function, or inducible, triggered by external signals such as growth factors. Cancer cells, for example, often upregulate macropinocytosis to meet the increased nutrient demand of rapid growth.[120] Phagocytosis is the uptake of particles larger than 500 nm and is primarily carried out by specialized "professional" phagocytes such as macrophages, dendritic cells, and neutrophils, whose role is to clear foreign particles, pathogens, and dying cells from the body. Other cell types, such as fibroblasts and epithelial and endothelial cells, also exhibit limited phagocytic activity.[128]

The particular route taken is important because it determines the early intracellular fate of the nanoparticle, which vesicles it traffics through initially, how quickly it reaches the lysosome, and how long it resides inside the cell.[122] Although the different entry routes converge onto a common downstream sorting network, the entry pathway influences how the nanoparticle is processed within it. In CME and caveolae-mediated endocytosis, a scission protein mediates release of the newly formed vesicle from the plasma membrane, whereas in macropinocytosis, membrane protrusions close to enclose extracellular material and form a macropinosome. The resulting vesicles fuse with early endosomes, which act as central sorting hubs directing cargo toward different intracellular destinations.[121] A fraction of the cargo is routed to recycling endosomes and returned to the plasma membrane, while the remainder matures into late endosomes that either fuse with lysosomes — exposing the cargo to degradative enzymes — or are

exocytosed, releasing their contents back into the extracellular environment.[120]

4.3.1 Nanoparticle Properties and their Effects on Cellular Uptake

The size of nanoparticles plays an important role in cellular uptake.[129] After a nanoparticle interacts with the cell membrane through receptor–ligand interactions, electrostatic interactions, or hydrophobic interactions, the membrane begins to bend and form pits or ruffles that eventually envelop the particle completely.[120] The efficiency of this membrane invagination strongly depends on particle size. For example, one study showed that among spherical gold nanoparticles ranging from 14 to 100 nm in diameter, those with a diameter of 50 nm were internalized most efficiently.[130] Another study reported that particles smaller than 40–50 nm were taken up more slowly due to their inability to occupy multiple receptor binding sites simultaneously.[131]

Particle shape is another important factor influencing cellular uptake. Rod-shaped particles have been found to undergo slower uptake compared to spherical particles.[120] This has been hypothesized to result from slower membrane wrapping or from surfactant molecules on the nanorods interfering with ligand binding.[132] Studies have also shown that rods with a lower aspect ratio are taken up faster than rods with a higher aspect ratio,[133] and that a larger particle surface area can lead to faster uptake.[134] Furthermore, internalized rods have been reported not to cause lysosomal swelling, which was observed for internalized spheres, suggesting that rods may induce a milder cellular stress response.[135]

Surface charge and hydrophobicity also strongly influence cellular uptake. Positively charged nanoparticles generally exhibit higher uptake than neutral or negatively charged particles,[120] in part because cationic particles can enter cells by disrupting or forming transient holes in the membrane.[136] Hydrophobic nanoparticles can insert directly into the lipid bilayer and cross the membrane without conventional membrane wrapping.[137] In biological media, however, these bare-surface effects are attenuated by protein corona formation, which screens the underlying surface functionalization and reshapes how the particle is perceived by the cell (see **Section 4.2.1**). Deliberate surface functionalization is therefore widely used to steer cellular interactions — for example, to direct particles toward specific cell types, as demonstrated for cervical-cancer-targeted nanoparticles with enhanced uptake relative to unfunctionalized controls.[138]

4.3.2 Intracellular Transport

Once nanoparticles enter the cell, they encounter a complex intracellular transport system that distributes ions, metabolites, proteins, and organelles across the cell.[5] This transport operates over a wide range of length scales, from nanoscale mixing that supports reaction kinetics to the directed movement of cargo over micrometers. Short-range transport is dominated by Brownian diffusion, which drives mixing and random encounters between molecules. For longer distances and larger cargoes such as organelles or RNA–protein complexes, cells rely on active transport, in which molecular motors move along cytoskeletal filaments.[5] Some cells additionally use advection — bulk flow of cytosolic fluid — to move particles through the cytoplasm (**Figure 4.5**).

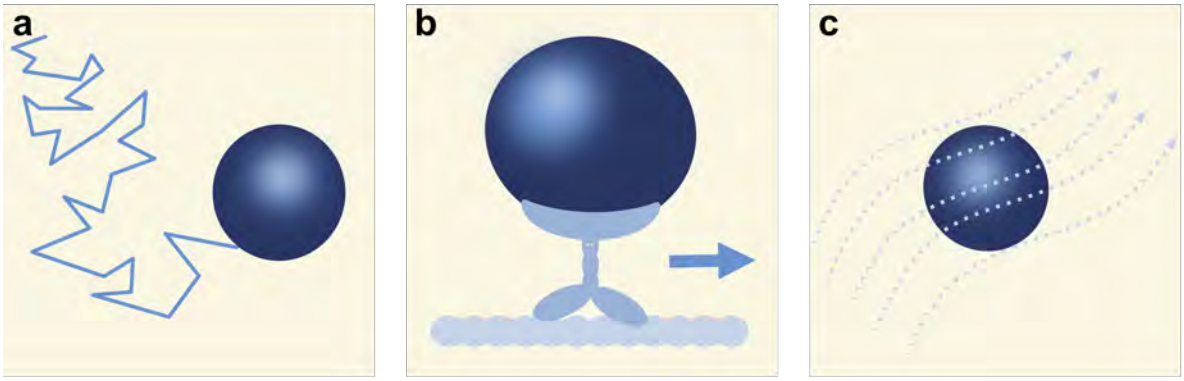

Figure 4.5: Intracellular transport mechanisms: **a** diffusive motion, **b** active motor-driven transport along cytoskeletal filaments, and **c** advection in a flowing cytoplasm.

In this thesis, we focus on diffusion and motor-driven transport, as these are the dominant modes for intracellular nanoparticles in mammalian cells. Both can be resolved experimentally by single-particle tracking (SPT),[139] which follows the position of individual nanoparticles over time and, through analysis of their trajectories, distinguishes diffusive motion from directed, motor-driven transport. This approach is used in **Paper II** to characterize intracellular transport phenotypes of gold nanorods in two therapy-resistant prostate cancer cell lines, PC-3 and LNCaP-19, and to examine how nanorod surface functionalization modulates these transport patterns.

4.3.2.1 Low Reynolds Number Regime

Transport at the micro-scale is characterized by how the distance traveled by particles scales with time, which reflects whether the motion is driven by diffusion, active trans-

port, or other transport mechanisms. Intracellular transport occurs within the regime of low Reynolds numbers, which is defined by

$$Re = \frac{va\rho}{\eta} = \frac{va}{\nu} \tag{4.1}$$

where v is the speed of flow, a is the characteristic length (e.g., particle diameter), ρ is the fluid density, η is the dynamic viscosity, and ν is the kinematic viscosity of the fluid. If, for example, a particle with a diameter of $a = 0.1$ μm is transported within a cell, assuming the viscosity of water at $\nu = 1 \times 10^{-6}$ m^2s^{-1} ($\eta = 1 \times 10^{-3}$ Pa·s) and moving at a speed of $v = 1$ μm s^{-1}, the Reynolds number becomes $Re = 10^{-7}$, that is $Re \ll 1$.[8] In this regime, viscous forces dominate over inertial forces, and particle motion is governed primarily by viscous drag rather than inertia. This means that particles stop moving immediately when the applied force is removed, and continuous force is required to maintain motion.[7]

Intracellular transport can be characterized by a power-law relationship between distance traveled and time, $l \sim t^{\beta}$, where the scaling exponent β ranges between $0 < \beta \leq 1$. Active transport, such as the motion of organelles driven by molecular motors or intracellular fluid flows, corresponds to $\beta = 1$, resulting in motion at approximately constant velocity ($l = vt$). In contrast, diffusive transport, or transport resembling a random walk, scales as $l \sim (Dt)^{0.5}$, which describes particles with diffusivity D in a viscous fluid and motion with uncorrelated steps over long time scales.[140]

Even slower scaling of distance explored versus time ($\beta < 0.5$) occurs when particles undergo sub-diffusive motion.[141] This type of transport is characterized by negative correlations in particle velocities between consecutive time steps, meaning that particles are more likely to reverse direction over time. Such behavior can occur, for example, when particles move through a crowded or viscoelastic medium such as the cytoplasm, which contains polymer networks and macromolecular crowding.[5] The cytoplasmic transport of large protein complexes and organelle-sized particles is therefore often observed to exhibit sub-diffusive behavior.

4.3.2.2 Diffusion

Intracellular transport is a highly regulated system and is essential for cellular homeostasis. The choice of transport mechanism depends on several factors, such as the size of the particle, the distance over which it must be transported, whether directed delivery

to a specific location is required, and the time scale of the biological process. Diffusive transport is primarily used for small molecules such as ATP, ions, and metabolites, as these can diffuse at sufficiently high speeds to support processes such as molecular mixing, which enables biochemical reactions to occur, and the maintenance of chemical gradients.[5] For example, ATP molecules produced in mitochondria can diffuse through the cytoplasm to ATP-requiring enzymes throughout the cell.[142] Diffusion is driven by thermal fluctuations and governed by the thermal energy of the surrounding fluid (k_BT), meaning that particle motion arises from random collisions with surrounding molecules and does not require ATP-driven transport mechanisms.

The motion of diffusing particles in a viscous medium can be described as a random walk. For such motion, the mean squared displacement (MSD) increases linearly with time in each spatial dimension:

$$\text{MSD} = \langle x^2 \rangle = 2Dt, \qquad D = \frac{k_BT}{\mu} \tag{4.2}$$

where μ is the friction coefficient of the particle, k_B is Boltzmann's constant, and T is the temperature of the medium. For a spherical particle moving in a viscous fluid at low Reynolds numbers, the friction coefficient is given by Stokes' law, $\mu = 6\pi\eta a$, where η is the viscosity of the fluid and a is the particle radius. Combining this expression with **Equation 4.2** yields the Stokes–Einstein relation,

$$D = \frac{k_BT}{6\pi\eta a}. \tag{4.3}$$

The Stokes–Einstein relation relies on several assumptions, namely that the particle is embedded in a continuous, purely viscous, three-dimensional fluid of infinite extent, and that the motion is driven only by thermal fluctuations with no external sources of energy.[143] However, the intracellular environment does not fully satisfy these assumptions, as the cytoplasm is a crowded, viscoelastic, and actively driven medium. As a result, diffusion in cells often deviates from classical Brownian motion. A detailed discussion of diffusion in complex intracellular environments, including crowding effects, viscoelasticity, and active processes, is beyond the scope of this thesis. For a deeper overview, see the review by Mogre et al.[5]

4.3.2.3 Active Transport

For the transport of larger organelles or protein complexes, diffusion becomes inefficient due to the much longer transport times required. Cells therefore rely on active transport, in which cellular cargo is attached to motor proteins that use ATP hydrolysis as an energy source to move in a directed manner along cytoskeletal filaments.[5] Active transport is used when cargo must be delivered to specific locations within the cell. For example, during cell membrane repair,[144] vesicles are transported to the damaged site to facilitate repair. Another example occurs during mitosis, when organelles must be distributed between daughter cells.[145]

The velocities of actively transported cargos have been found to range between 0.3–2 μm s^{-1}[8,146–148] and are usually independent of cargo size.[149] In mammalian cells, long-distance transport primarily occurs along microtubules, which are hollow tubes that can reach lengths of up to 30 μm.[150] Motor proteins move along the outside of these filaments, carrying cargo between different regions of the cell. Microtubules, as well as actin filaments, are polarized structures with distinct plus and minus ends, and the polarization of these cytoskeletal "highways" governs the direction of active transport. In many mammalian cells, the minus end of the microtubules is directed toward the nucleus, while the plus end is directed toward the cell periphery.[5]

Two main families of motor proteins are responsible for transport along microtubules, namely kinesins and dyneins.[146,151] Kinesins transport cargo away from the nucleus toward the plus ends, which is called anterograde transport, while dyneins transport cargo toward the minus ends, corresponding to retrograde transport toward the nucleus. Many cargos show bidirectional transport,[152] switching direction along the microtubules as a result of both kinesin and dynein motors being attached to the cargo simultaneously.[153] Some cargos do not attach directly to motor proteins, but instead "hitchhike" by attaching, via a linker protein, to another organelle that is already in transport.[148] Active transport enables directed movement of vesicles, organelles, and signaling molecules to specific locations within the cell and is essential for processes such as growth, repair, signaling, and cell division. Together with diffusion and cytoplasmic flows, it forms an integrated intracellular transport system that maintains cellular organization and function.

5

Materials and Methods

In the preceding chapters, the basic principles of light–matter interaction in gold nanorods, their behavior in optical traps, and their interactions in biological environments have been established. Together, these provide the necessary foundation for the work explored in this thesis and define the context in which the experiments are conducted. This chapter describes the materials and experimental procedures used to obtain the results presented in this thesis. It outlines the optical and microscopy techniques, including dark-field microscopy and the optical tweezers setup, as well as the analysis methods used to probe cellular nanomotion and intracellular transport. In this way, the chapter provides a practical framework for exploring cellular dynamics at the nanoscale, while demonstrating the use of gold nanorods as probes in both physical and biological systems.

5.1 Materials and Sample Preparation

5.1.1 Gold Nanorod Synthesis

The gold nanorods used in this thesis were synthesized by Dr. Lei Shao using a wet-chemical seed-mediated growth method, and are shown in **Figure 5.1**. In this approach, small gold seed particles are first prepared by reducing a gold salt ($HAuCl_4$) in the presence of a surfactant. These seeds are then added to a separate growth solution, where further reduction of gold ions occurs preferentially on the seed surfaces rather than through new nucleation, allowing the particles to grow in a controlled manner.[154]

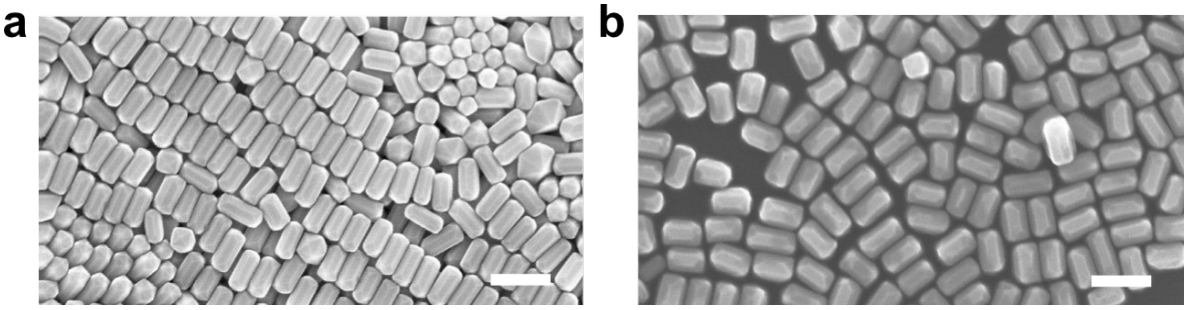

Figure 5.1: Scanning electron microscopy (SEM) images of the two types of gold nanorods used for the work presented in this thesis. **a** Gold nanorods with an average size of $\sim 70 \times 140$ nm. **b** Gold nanorods with an average size of $\sim 100 \times 165$ nm. Scale bar: 200 nm.

The growth solution contained a binary surfactant mixture of hexadecyltrimethylammonium bromide (CTAB) and sodium oleate (NaOL). Compared to the more commonly used CTAB-only system, this binary mixture provides improved control over the nanorod diameter and narrower size distributions.[154] Anisotropic growth into rod-shaped particles is driven by the addition of silver ions, which promote elongation along one crystallographic direction and thereby determine the final aspect ratio of the nanorods.

Because the longitudinal LSPR of gold nanorods depends strongly on their aspect ratio, the resonance wavelength was further fine-tuned after synthesis by anisotropic oxidation. In this step, additional CTAB, HCl, and $HAuCl_4$ are added to the nanorod solution, which selectively shortens the rods while largely preserving their diameter.[42,154] The LSPR can thus be tuned to match the wavelength of the trapping laser used in the optical experiments, which is important for efficient optical trapping and rotation.

5.1.2 Surface Functionalization of Gold Nanorods

In both **Paper I** and **Paper II**, the experiments were conducted in biological environments, where the nanorods were located either in the vicinity of or inside living cells. The synthesis method results in a bilayer of CTAB molecules on the surface of the nanorods, which must be removed prior to introduction into cell samples, as CTAB is highly cytotoxic and can severely affect cell viability.[155,156] This is achieved through surface functionalization, which not only reduces cytotoxicity but also preserves colloidal stability and minimizes aggregation.

Three different surface functionalizations were used in this work: a hydroxyl-terminated

oligo(ethylene glycol) alkanethiol self-assembled monolayer (HS-$(CH_2)_{11}EG_4OH$, hereafter SAM-OH), the corresponding carboxyl-terminated alkanethiol (HS-$(CH_2)_{11}EG_6COOH$, SAM-COOH), and thiolated polyethylene glycol with a molecular weight of 5kDa (PEG). SAM-OH was used in **Paper I**, as it was stable in cell culture medium and did not bind to the cell membrane during rotation measurements. SAM-COOH and PEG were used in **Paper II** to investigate whether surface functionalization affected the intracellular transport of gold nanorods.

SAM functionalization. The nanorod solution was first washed by centrifugation at 7500 rpm for 60 s, after which the supernatant was removed and the nanorods were resuspended in Milli-Q water. The alkanethiol (SAM-OH or SAM-COOH; ProChimia, Poland) was dissolved in absolute ethanol to a concentration of 10 mM and mixed with the nanorod solution to a final thiol concentration of 0.5 mM, corresponding to a CTAB:thiol ratio of approximately 1:4. The solution was then stored overnight at 4 °C to allow formation of the self-assembled monolayer. After incubation, the solution was washed again by centrifugation, removal of the supernatant, and resuspension of the nanorods in Milli-Q water.

PEG functionalization. Thiolated PEG was dissolved at 1 mg/mL and added to the washed nanorod solution at a volume ratio of 1:5 (PEG solution:nanorod solution), giving a final PEG concentration of 0.17 mg/mL. The nanorods were incubated overnight, centrifuged, and redispersed in 10× diluted PBS buffer (10 mM phosphate buffer, 140 mM NaCl, and 3 mM KCl, pH 7.4 at 25 °C; Sigma-Aldrich).

5.1.3 SPR Measurements

To investigate how the two surface coatings interact with a protein-rich solution, and whether protein adsorption (PA) differs between them, we used Multi-Parametric Surface Plasmon Resonance (MP-SPR) on a Navi 220A NAALI instrument (BioNavis, Finland) with a laser wavelength of 670 nm. Surface Plasmon Resonance (SPR) is an optical technique that enables real-time, label-free detection of changes at a metal–dielectric interface. When plane-polarized light is incident on a thin metal film under total internal reflection conditions, it can excite surface plasmons at a specific resonance angle. This resonance condition is highly sensitive to the refractive index near the surface.[157] As molecules accumulate at the interface, the local refractive index changes, resulting in a shift in the resonance angle. The magnitude of this shift is directly related

to the amount of material adsorbed on the surface, allowing quantitative comparison of PA between different surface coatings.

SPR gold sensor slides with a gold thickness of ∼50 nm (BioNavis, Finland) were cleaned twice with 70% EtOH and dried with N_2 after each step. The slides were then rinsed with Milli-Q water and dried with N_2. The gold slides were subsequently functionalized with either SAM-COOH or PEG. For the SAM-COOH functionalization, the thiol was dissolved in absolute ethanol to a concentration of 10 mM, after which 105 μL of this solution was added to 10 mL Milli-Q water to form the immersion solution for the sensor slides. For the PEG functionalization, PEG was dissolved in PBS (pH 7.4) to a concentration of 1 mg/mL and subsequently mixed with Milli-Q water at a ratio of 1:5 (PEG solution:water). During functionalization, the sensor slides were stored in the dark at 4 °C overnight to allow formation of a self-assembled monolayer on the surface. Prior to measurement, the sensor slides were air-dried under ambient conditions.

PA was measured on the two functionalized surfaces using cell culture media (CCM) and bovine serum albumin (BSA). CCM was prepared as described in the cell culture procedure, and BSA was dissolved in PBS to a concentration of 10 mg/mL. Both solutions were diluted 10× in Milli-Q water and filtered (0.22 μm) to prevent clogging of the instrument tubing. Measurements were performed at room temperature using the instrument's two parallel channels, enabling simultaneous acquisition of PA from CCM and BSA on the same surface. The flow cell was first filled and rinsed with PBS at 20 μL/min until a stable baseline was obtained. PBS was then exchanged with CCM in one channel and BSA in the other, and the solutions were injected for 35 minutes at 10 μL/min, followed by rinsing with PBS. The SPR response was quantified as the angular shift, defined as the difference between the PBS baselines before and after injection. Experiments were performed on three sensor slides for each surface functionalization.

5.1.4 Cell Culturing and Sample Preparation

HMEC-1

In Paper I, cell experiments were performed on human microvascular endothelial cells (HMEC-1), kindly provided by Patricia Lalor's group at the University of Birmingham. Cell culture was performed by Dr. Charlotte B. Hamngren, with the exception of the cells used for the viability assay, which were prepared by the author (**Figure 5.2**).

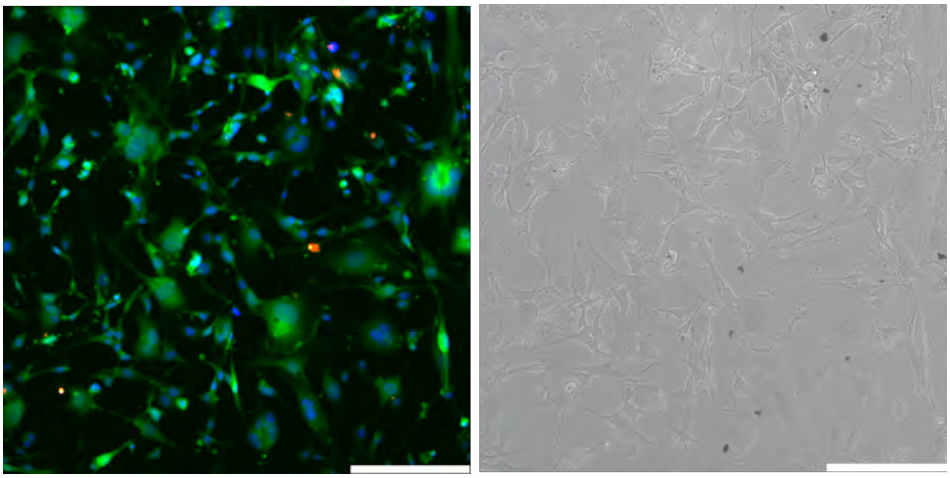

Figure 5.2: Cell viability assay of the HMEC-1 cell line with the addition of gold nanorods functionalized with hydroxyl-terminated SAMs. Green fluorescence corresponds to live cells stained with calcein-AM, red fluorescence marks compromised or dead cells stained with ethidium homodimer-1 (EthD-1), and blue fluorescence highlights all nuclei stained with Hoechst. Phase-contrast images of the corresponding fields are shown on the right for structural context. Scale bar: 166 μm.

HMEC-1 cells were maintained at 37 °C in a humidified incubator with 5 % CO2. The culture medium was MCDB 131 (Gibco, Fisher Scientific, USA), supplemented with 10 mM L-glutamine, 10 ng mL^{-1} epidermal growth factor (EGF), 1 µg mL^{-1} hydrocortisone, 10 % fetal bovine serum (FBS), 1 % non-essential amino acids, and 1 % penicillin/streptomycin. Cells were allowed to reach 80 % to 90 % confluency before use in experiments.

For harvesting, the cells were detached using TrypLE Express Enzyme (Gibco, Thermo Fisher Scientific, USA) with a 7-minute incubation, followed by centrifugation at 200 g for 7 minutes. The supernatant was discarded and the pellet was resuspended in fresh medium and diluted to roughly 30 % confluency. This low seeding density produced a sparse cell distribution on the glass coverslips, which was important for the subsequent nanomotion measurements. The diluted cell suspension was then deposited onto cleaned coverslips and left to sediment for 2 hours in the incubator.

Each coverslip carrying sedimented HMEC-1 cells served as the top layer of the imaging chamber. Cells along the edges of the coverslip were carefully wiped away with a lint-free tissue to enable a tight seal. A 120 µm spacer was positioned on the coverslip, and 3 µL of a gold nanorod suspension (approximately 10^7 mL^{-1} in MCDB 131 medium) was drop-cast onto the surface before the chamber was closed with a microscope-grade

glass slide. Measurements were started immediately after chamber assembly, under conditions that minimized non-specific adhesion and prevented appreciable cellular uptake of the nanorods.

Procedure for Fixing HMEC-1

For control measurements using fixed HMEC-1 cells, the cells were cultured and seeded on coverslips as described above. All fixation steps were performed at room temperature. The cells were first washed three times with cold (4 °C) phosphate-buffered saline (PBS), with 5-minute intervals between washes. They were then fixed with cold 4 % formaldehyde for 15 minutes, followed by three PBS rinses and an additional three PBS washes, again spaced by 5 minutes. After fixation, the cells were stored in PBS at 4 °C until measurement.

Viability Assay for HMEC-1

HMEC-1 cells were cultured as described above and seeded at ∼50% confluency in 35 mm glass-bottom dishes and incubated overnight at 37°C with functionalized nanorods (1:100 dilution of stock solution). Cell viability was assessed using a Live/Dead Viability/Cytotoxicity Kit (Thermo Fisher Scientific) with Hoechst staining. Cells were rinsed with PBS (+/+) and incubated with staining solution (calcein-AM, ethidium homodimer-1, and Hoechst) for 15 min at 37°C in the dark. Imaging was performed on a Leica DMI6000B fluorescence microscope using a 20× objective. Images were analyzed in ImageJ by thresholding each channel to quantify live (green), dead (red), and total (blue) cells. Viability was calculated as the percentage of live cells relative to total cells.

LNCaP-19 and PC-3

The cells used in **Paper II**, were cultured by Dr. Peter Dahlbecker and Dr. Hana Jungová and provided by Karin Welén, Sahlgrenska Academy, University of Gothenburg.[158] Human prostate cancer cell lines LNCaP-19 and PC-3 were cultured in RPMI-1640 medium supplemented with 10% fetal bovine serum (FBS), sodium pyruvate (1 mM), $NaHCO_3$ (0.375 g L^{-1}), glucose, and 1% penicillin–streptomycin. Cells were maintained at 37 °C in a humidified incubator with 5% CO_2 and passaged at 70–80% confluency. For passaging, the culture medium was removed, and adherent cells were rinsed with

phosphate-buffered saline (PBS, without Ca^{2+}/Mg^{2+}), detached using trypsin, resuspended in complete medium, and seeded into new culture flasks containing prewarmed medium.

For nanoparticle uptake experiments, cells were seeded onto cleaned and sterilized glass microscope slides at approximately 50% confluency and allowed to adhere overnight. The following day, cells were exposed to gold nanorods (gold nanorods) and incubated for 12–16 h at a final concentration of 5 pM. After incubation, excess gold nanorods were removed by washing three times with pre-warmed culture medium, and fresh medium was added prior to live-cell imaging.

Viability Assay for LNCaP and PC-3

A viability assay was performed to assess whether functionalized gold nanorods affected cell viability under the exposure conditions used in this study. PC-3 and LNCaP-19 cells were incubated overnight with PEG- or SAM-functionalized nanorods and evaluated using a Live/Dead Viability/Cytotoxicity assay (Thermo Fisher, USA). The experiments were performed by Dr. Hana Jungová. As a rigorous control, cells were exposed to a nanorod concentration approximately 100-fold higher than that used for the live-cell transport measurements.

Cells were cultured on glass coverslips and incubated overnight at 37 °C with a 1:100 dilution of the functionalized nanorod stock solution. After exposure, the samples were washed twice with Dulbecco's phosphate-buffered saline (DPBS) containing Ca^{2+} and Mg^{2+} (GE Healthcare, Sweden) and stained with 4 μM calcein-AM and 4 μM ethidium homodimer-1 (EthD-1) in DPBS at 37 °C for 40 minutes. The samples were then washed twice more with DPBS before imaging. A dead-cell control was prepared in parallel by treating a separate set of cultured cells with 70 % ethanol for 7 minutes at room temperature prior to staining.

Fluorescence imaging was performed on an inverted microscope equipped with a mercury lamp and appropriate filter cubes. Calcein-AM and EthD-1 signals were detected through GFP (FF495, Semrock) and mCherry (49008 ET, Chroma) filter sets, respectively, using a 20× objective.

5.2 Dark-Field Microscopy

Gold nanoparticles exhibit enhanced scattering and due to this, dark-field (DF) microscopy is often used for their observation and imaging. In DF microscopy, the sample is illuminated with oblique light that passes through a DF condenser. The scattered light is collected by the objective lens, while transmitted light is excluded from the image, creating a dark background around the scattering sample structures (**Figure 5.3a, b**). DF imaging requires the numerical aperture of the condenser to be larger than that of the objective so that only scattered light, and not direct light, enters the objective. In this setup (**Figure 5.4**), an oil-immersion DF condenser with NA = 1.2-1.43 and an objective with NA = 0.7 were used to satisfy this condition.

DF imaging of cells is possible because cellular compartments differ in molecular density, and therefore in refractive index, from the surrounding cytoplasm, causing them to scatter the illuminating light.[159] DF imaging is also non-invasive and requires no staining, making it well suited for observing live cells in their native state. When combined with gold nanoparticles, DF is particularly advantageous because AuNPs scatter light far more intensely than biological structures, making them easily distinguishable from the cellular background.[160]

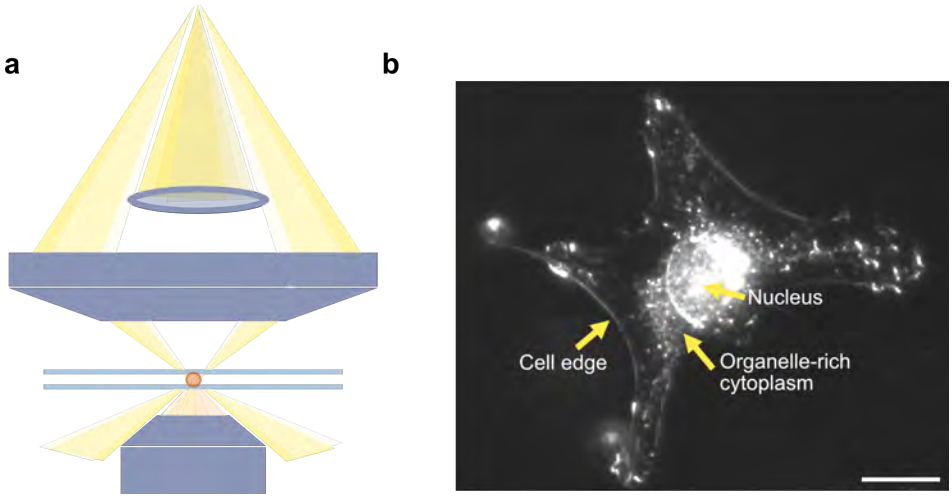

Figure 5.3: **a** Illustration of the inverted dark-field (DF) microscope used in this study, with the DF condenser positioned above the sample and the objective below. **b** DF microscopy image of an endothelial cell. The nucleus appears as a region of relatively homogeneous scattering, while surrounding vesicles and organelles scatter light more strongly, producing bright spots distributed throughout the cytoplasm. The cell boundary is visible as a faint outline at the periphery. Scale bar: 20 μm.

Figure 5.3b shows a DF image of an endothelial cell in which several structural features can be identified. The cell boundary appears only as a faint outline, reflecting the thin, well-spread morphology of the cell at its periphery, where there is little material to scatter the illuminating light. The nucleus is visible as a large region of relatively homogeneous scattering near the center of the cell. Surrounding and overlying the nucleus, the cytoplasm contains numerous bright, sub-micron puncta corresponding to vesicles and small organelles such as mitochondria and lysosomes. These structures fall within the size range (≈0.1–1 μm) where scattering is well described by Mie theory, and their refractive index contrast with the surrounding cytoplasm makes them efficient scatterers despite their small size.[159,161] The perinuclear region appears particularly bright, consistent with the high density of organelles typically found there.

5.3 Optical Trapping of Gold Nanorods in 2D

The measurements presented in **Paper I** rely on optically trapping a single gold nanorod, driving it to rotate, and reading out small variations in its rotation frequency. The rotation frequency depends on the particle's axial position within the trap, so once this dependence is calibrated, frequency fluctuations can be translated into nanometer-scale height variations of the surface beneath the particle. This section describes the optical setup, how the rotational dynamics are extracted from the back-scattered light, and how the same configuration is used both for nanomotion measurements on living cells (**Section 5.6**) and for non-contact surface profilometry (**Section 5.5**).

5.3.1 Setup for 2D Trapping

The optical trapping is achieved using an optical tweezers setup built around a Nikon Eclipse TE300 inverted microscope equipped with white-light DF illumination for nanoparticle imaging and detection.[42,66,81,162] The microscope is equipped with a piezoelectric stage, enabling precise spatial control along the x-, y-, and z-axes. Image acquisition is performed using a CMOS camera (sCMOS Neo 5.5, Andor), and a short-pass filter is installed in the detection path to block the trapping laser and thereby prevent photodamage to the camera sensor. A schematic illustration of the trapping setup is shown in **Figure 5.4**.

A collimated, linearly polarized laser beam (Xtra 2, Toptica Photonics) with a wavelength of 785 nm is directed into the microscope via a non-polarizing beam splitter

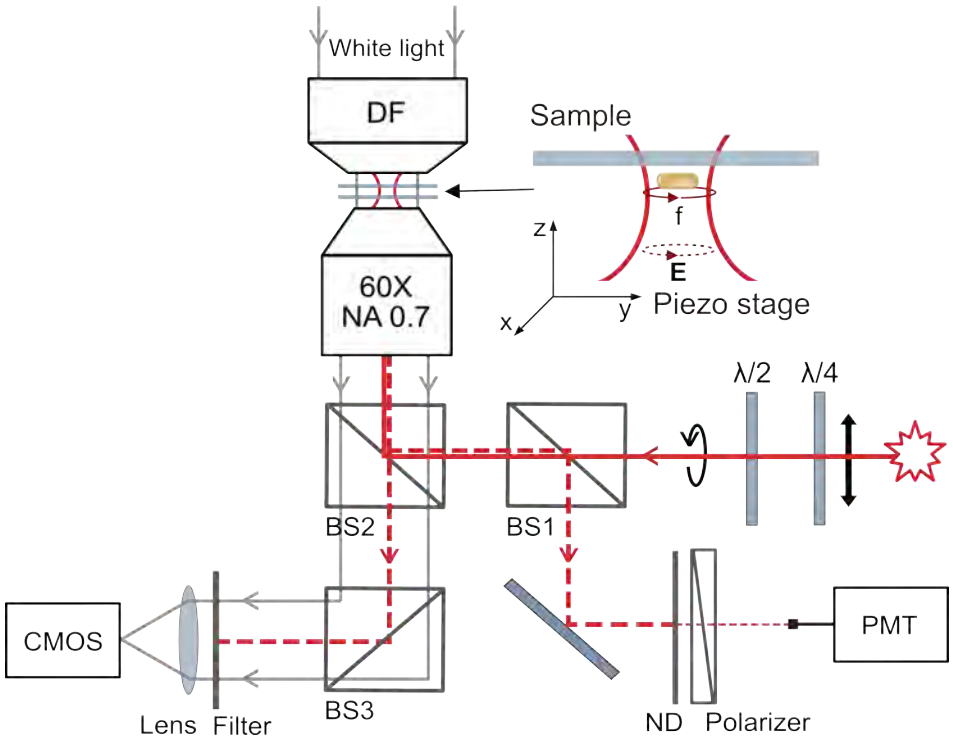

Figure 5.4: Schematic illustration of the optical setup: the inverted microscope enables trapping of a single gold nanorod against the upper cover glass of the sample chamber. Rotation of the nanorod is induced through spin angular momentum transfer, generated by a circularly polarized near-infrared laser beam (λ = 785 nm). The trapped particle is illuminated from above by a white light DF condenser. Laser light back-scattered from the particle passes through a polarizer before being collected by a fiber-coupled photomultiplier tube (PMT), for particle motion analysis.

(BS), BS2 in **Figure 5.4**. Since the experiment relies on rotating the trapped nanorod, the linear polarization of the laser must be converted to circular polarization. This is achieved using a $\lambda/4$ and a $\lambda/2$ wave plate. A $\lambda/4$ plate alone would normally suffice to produce circular polarization, but the beam splitter that directs the laser upward introduces ellipticity. The $\lambda/2$ plate pre-compensates for this, so that the slightly elliptical beam becomes circularly polarized after the beam splitter and before entering the objective. Angular momentum is then transferred from the circularly polarized beam to the nanorod, enabling optical trapping and rotation.

Due to the large scattering cross-section of the nanorods, the particles become optically trapped in two dimensions against the upper cover glass of the sample chamber.[42] The back-scattered light from the trapped nanorod is collected by the objective and directed out of the microscope. The objective used in the experiments was a 60×

magnification, 0.7 NA extra-long working distance air objective (Nikon). The back-scattered light is then directed via BS1, passed through a linear polarizer, and coupled into a fiber-coupled single-photon counting photomultiplier tube (PMT), which serves as our detector (Becker & Hickl). As the nanorod rotates around its short axis, the scattered light is dominated by scattering from the long axis of the rod. Due to the strong anisotropy of the nanorod and the longitudinal LSPR being close to the laser wavelength, the back-scattered light becomes linearly polarized. The polarization direction of the back-scattered light changes as the nanorod rotates, and by placing a linear polarizer in the detection path, the detector records periodic oscillations in the detected intensity. These intensity oscillations are then used to determine the rotation frequency of the nanorod.

5.3.2 Analyzing the Rotational Dynamics of a Gold Nanorod

We analyze the signal using two complementary methods: the autocorrelation function (ACF) and the Short-Time Fourier Transform (STFT) (**Figure 5.5**). The ACF correlates the signal with itself at different time lags, yielding the nanomotor's rotation frequency f and a decay time τ_0 that quantifies the loss of rotational phase coherence due to rotational Brownian motion. These parameters are averaged over the full measurement cycle. The STFT complements this by computing the discrete Fourier transform of short, windowed segments of the signal, producing a time–frequency representation in which the rotation appears as a peak at $2f$. From each time slice of the resulting spectrogram, both the instantaneous rotation frequency $f(t)$ and a time-resolved decay time $\tau(t)$ can be extracted, providing access to rotational dynamics on timescales shorter than the full measurement cycle.

Auto-Correlation Function

The detected intensity signal is recorded using time-correlated single-photon counting (TCSPC), where individual photon arrival times were recorded over the acquisition period. The rotation frequency and rotational dynamics were extracted by calculating the autocorrelation function (ACF) of the detected photon signal using the TCSPC analysis software. The ACF measures the similarity between the signal and a time-delayed version of itself as a function of the delay (lag). Consequently, it captures both the periodicity of the signal and the rate at which correlations decay over time,

providing information about the underlying rotational dynamics.[163] Periodic intensity fluctuations caused by the rotation of the nanorod appear as oscillations in the ACF, which can theoretically be described as

$$C(\tau) = I_0^2 + 0.5 I_1^2 \exp\left(-\frac{\tau}{\tau_0}\right) \cos(4\pi f \tau), \tag{5.1}$$

where I_0 represents the average intensity, I_1 denotes the amplitude of intensity fluctuation, f stands for the average rotation frequency, and τ_0 represents the autocorrelation decay time.[76] τ_0 is closely related to the rotational Brownian motion and is expressed as

$$\tau_0 = \frac{\gamma_r}{4 k_B T_r}. \tag{5.2}$$

Here, T_r denotes the rotational Brownian temperature, k_B represents Boltzmann's constant, and $\gamma_r(T)$ is the friction coefficient given by $\pi\eta(T)gL^3$. $\eta(T)$ represents the temperature-dependent dynamical viscosity of the surrounding water, g represents a geometrical shape factor dependent on the nanorod eccentricity, and L denotes the length of the nanorod. The rotational dynamics, and thereby the temperature, can be extracted by fitting the theoretical autocorrelation curve to the experimental data.

Short-Time Fourier Transform

The PMT collects back-scattered photons at a sampling frequency of 100 kHz, producing an intensity time trace of the rotating nanorod. The ACF provides precise estimates of the dominant periodicity and decay time, but these parameters are averaged over the entire acquisition time. However, the intensity trace also contains information about temporal variations in the nanorod's rotational dynamics on shorter time scales. The data show a periodic oscillation that corresponds to the alignment of the particle's long axis with the linear polarizer, this scattering-maxima occurs twice per revolution of the rod. To resolve these time-dependent variations, the signal is analyzed using the Short-Time Fourier Transform (STFT). While time-dependent changes could also be analyzed by dividing the signal into segments and analyzing each segment separately, the STFT provides a continuous time–frequency representation with improved temporal resolution.

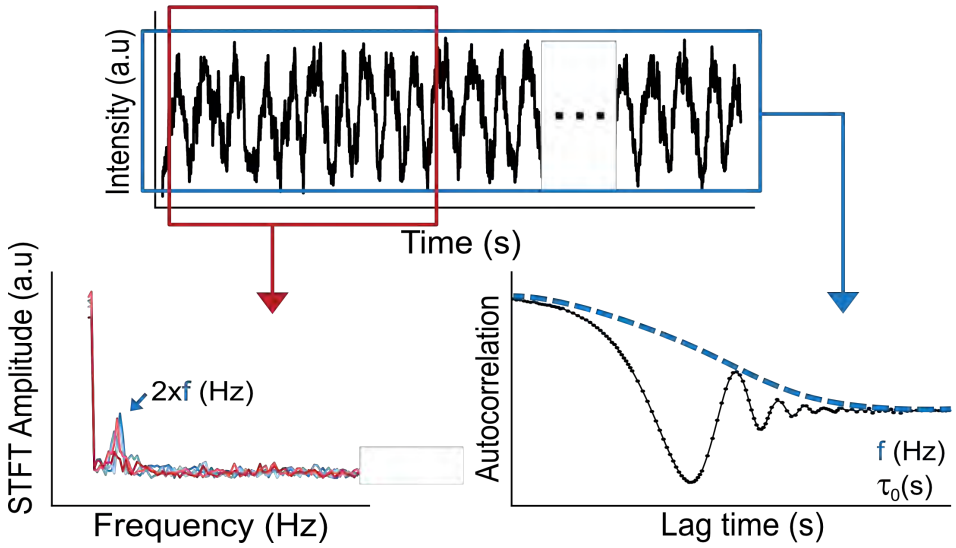

Figure 5.5: The signal contains information about the rotational dynamics of the optically trapped nanomotor. Top: Time trace of the backscattered intensity from the nanomotor. Bottom left: Local power spectrum obtained from the Short-Time Fourier Transform (STFT), showing a peak at twice the rotation frequency, $2f$. The position of the peak yields the instantaneous rotation frequency, while its Lorentzian width yields the decay time $\tau(t)$. Bottom right: Autocorrelation function (ACF) of the signal, from which the rotation frequency and decay time τ_0 are extracted.

STFT is a time–frequency representation in which the signal is divided into shorter segments, and the Fourier transform is computed for each segment. This method is particularly useful when the signal contains temporal variations that would otherwise be averaged out if a standard Discrete Fourier Transform (DFT) or Discrete-Time Fourier Transform (DTFT) were applied to the entire signal, which can result in loss of time-dependent information.[164,165]

The STFT is computed by sliding a window function $w[n]$ with length M over the signal $x[n]$ and calculating the DFT of each window segment of the signal. The window function moves over the original signal at intervals of R, with an overlap of $L = M - R$ between adjoining segments. For a discrete signal, the STFT is defined as

$$X[m,\omega] = \sum_{n=-\infty}^{\infty} x[n]w[n-m]e^{-j\omega n}, \tag{5.3}$$

where (m) represents the time index corresponding to the center of the window, and (n) denotes the time variable. In the resulting spectrogram, a peak appears at twice the

rotation frequency (see **Figure 5.5**, bottom left). Dividing this frequency by two yields the instantaneous rotation frequency $f(t)$, producing a trace analogous to that obtained from the ACF but with higher time resolution. A time-resolved decay time $\tau(t)$ can also be obtained from the spectrogram. By the Wiener-Khinchin theorem,[166] the ACF and the power spectrum form a Fourier transform pair, so an exponentially decaying ACF corresponds to a Lorentzian peak in the power spectrum. Fitting a Lorentzian to the peak in each time slice of the spectrogram (see **Figure 5.5**, bottom left) therefore allows $\tau(t)$ to be extracted via[166]

$$\tau = \frac{1}{\pi \cdot FWHM}. \tag{5.4}$$

The choice of window function affects the time and frequency resolution of the STFT. A commonly used window is the rectangular window, which simply selects a segment of the signal without modification. Another common choice is the Hanning window, which tapers to zero at the edges, producing smoother transitions between segments and reducing spectral leakage.[167]

Spectral leakage occurs when energy from one frequency component spreads into adjacent frequency bins in the DFT.[167] This arises because the DFT implicitly treats the analyzed segment as one period of an infinitely periodic signal; when the segment does not contain a whole number of periods, discontinuities at the segment boundaries cause energy to smear across neighboring bins. Therefore, the choice of window function should be adapted to the characteristics of the signal under analysis. The back-scattered light from the rotating nanorod produces a signal that is not strictly periodic, particularly when the particle is trapped above a living cell where environmental fluctuations affect the rotational dynamics. In this case, the Hanning window is preferable, as its tapered edges suppress boundary discontinuities and yield a more accurate representation of the signal in the frequency domain.

Another important parameter is the window length, which governs the trade-off between temporal and frequency resolution: a shorter window provides higher temporal resolution at the expense of broader spectral peaks, while a longer window sharpens the peaks at the cost of temporal resolution.[164] For the data analyzed in this work, the rotation period of the nanorod must also be considered. To reliably extract frequency changes caused by environmental variations, the nanorod must complete at least one full rotation within the time window. Consequently, the window length must be at least

equal to the duration of one rotation. In this work, the selected time window was on the order of 2–5 ms, corresponding to approximately 10–20 complete revolutions. A 50% overlap was used, which satisfies the constant-overlap-add condition for the Hanning window and ensures uniform temporal coverage of the signal.[168]

5.4 Nanomotion Measurements with an Optically Trapped Gold Nanorod

The setup described above is used to measure nanoscale height fluctuations on the membranes of living cells (**Paper I**). The measurement procedure consists of three steps, illustrated in **Figure 5.6a**. First, a single functionalized gold nanorod is optically trapped against the upper coverslip of the sample chamber using the circularly polarized 785 nm laser, with the laser power set to the minimum level that maintains stable trapping (typically 4–5.5 mW).

The rotation frequency of the trapped nanomotor is then calibrated against its axial position by translating the piezo stage in 100 nm steps and recording the frequency at each height (**Figure 5.6b**). The frequency depends on the distance from the laser focus, reaching a maximum near the focus and decreasing at larger separations due to reduced optical torque, and the relationship is well described by a second-order polynomial fit that defines the calibration curve $f(z)$ (**Figure 5.6c**). Both the rotation frequency and the scattering intensity of the nanomotor depend on its axial position and can in principle be used as readouts of membrane height; rotation frequency is used as the primary signal for the nanomotion measurements in **Paper I**, while scattering intensity is used for the surface profilometry measurements described in **Section 5.5**.

After calibration, the nanomotor is positioned at the midpoint of the calibrated range, which maximizes the dynamic range available for detecting membrane displacements, and is then laterally relocated to a targeted region on a living cell — typically the nucleus, perinuclear region, or cell periphery. Its rotation frequency is monitored continuously over time, and vertical displacements of the cell membrane modulate the nanomotor's axial position within the optical trap, which in turn modulates its rotation frequency. Applying the calibration curve to the measured frequency trace $f(t)$ yields a time-resolved trace of axial displacements $z(t)$, from which nanomotion amplitudes and dynamics are quantified.

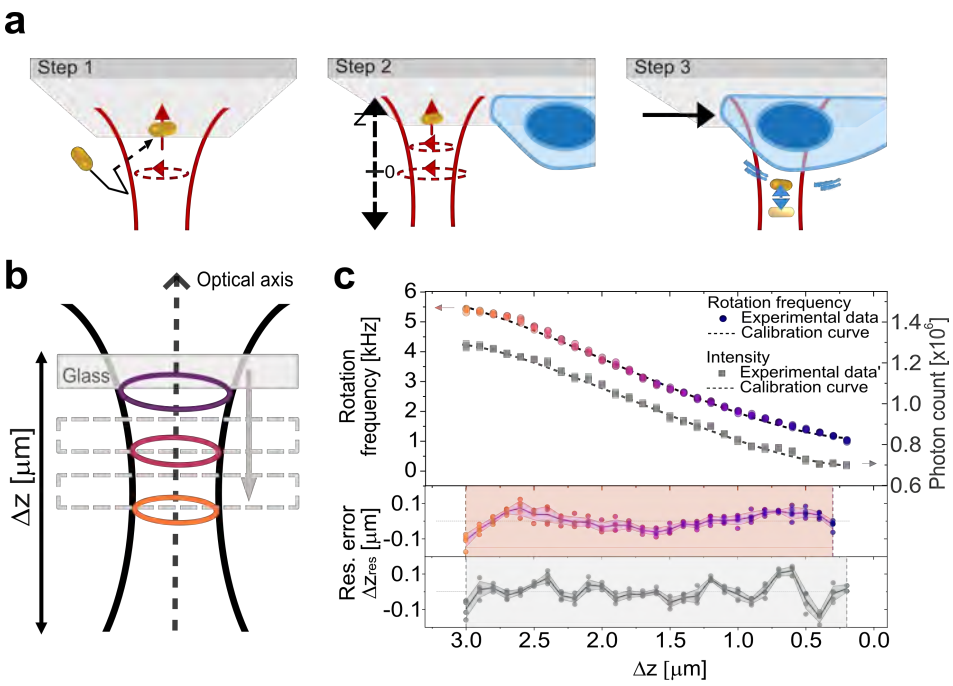

Figure 5.6: **a** Schematic of the three-step nanomotion measurement protocol. Step 1: a single gold nanorod is optically trapped against the upper coverslip. Step 2: a calibration curve is acquired by axially translating the piezo stage and recording the rotation frequency at each height. Step 3: the nanomotor is laterally relocated above a targeted region on a living cell, where its rotation frequency is monitored over time and converted to axial displacements via the calibration curve. **b** Schematic illustrating calibration curve acquisition through stage displacement. **c** Rotation frequency (circles) and scattering intensity (squares) as functions of axial position for a nanomotor ($\approx$ 164 $\times$ 98 nm) at 5.5 mW laser power in water. The dashed line shows a polynomial fit used to obtain the calibration curves. Reproduced from.[28] © 2025 The Author(s). *Small Methods* published by Wiley-VCH GmbH.

5.5 Surface Profilometry with 2D Trapped Gold Nanorod

The same trapping configuration described above can also be used to map surface topography. In an ongoing project, we exploit the equilibrium particle–surface separation that arises from the balance between radiation pressure and electrostatic repulsion. The trapped nanorod can be scanned across the substrate beneath it by laterally translating the sample with a piezo stage. Variations in surface height beneath the particle modulate its axial position within the trap, which is read out through either the rotation frequency or the scattering intensity, as in the nanomotion measurements. The

maximum accessible feature size depends on the equilibrium separation, which can be tuned through the ionic strength of the surrounding solution. The following subsections characterize this approach. We first quantify how lateral motion affects measurement stability, then demonstrate profilometry on microscale features, and finally show how ionic strength can be used to access different feature sizes.

5.5.1 Scan-Speed Effect on Measurement Stability

The lateral translation of the trapped gold nanorod introduces noise in the rotation frequency. **Figure 5.7a** shows the standard deviation (SD) of the inferred height as a function of particle velocity, where the SD increases with increasing speed. The SD rises sharply from approximately 50 nm at rest to approximately 250 nm at 1 μm/s, a factor of five, and then grows more moderately with further increases in speed, reaching approximately 325 nm at 4 μm/s.

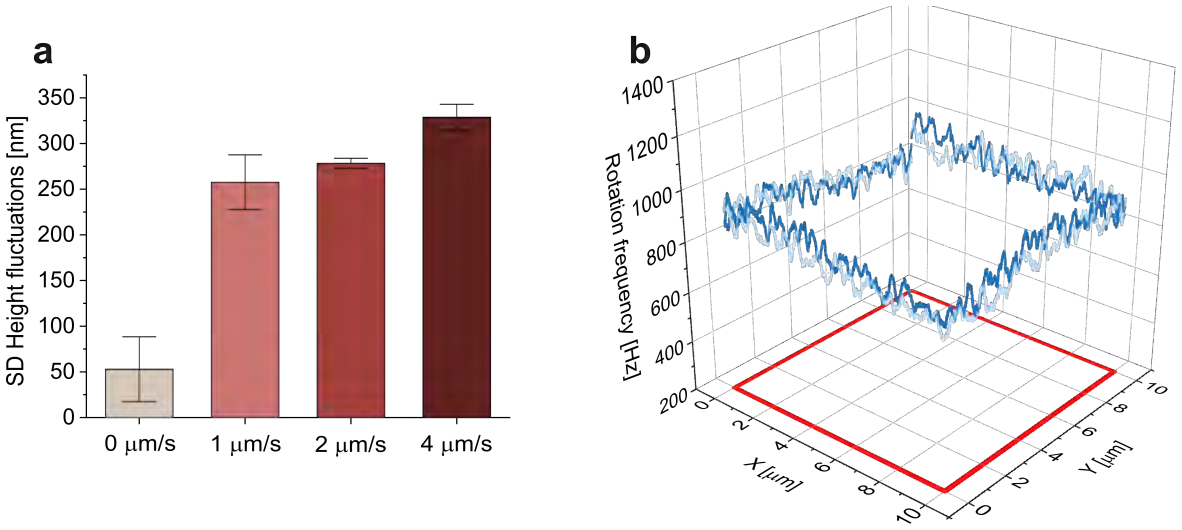

Figure 5.7: Characterization of measurement stability as a function of scan speed for a trapped gold nanorod used as a profilometry probe. **a** Standard deviation of height fluctuations of a trapped gold nanorod measured over 5 μm at different scan speeds ($n = 4$ per speed). Bars show the mean; error bars indicate ± 1 SD. **b** Rotation frequency recorded while tracing the perimeter of a 10 μm $\times$ 10 μm square on flat PDMS, repeated twice at 1 μm/s (reproducibility test). All data are analyzed using STFT (1024-point Hanning window) and smoothed with a third-order Savitzky–Golay filter (51-point window).

This behavior can partly be understood from the force balance in the optical trap. A particle moving through the fluid experiences a viscous drag force proportional to its

velocity[a]. Under steady motion, the drag force is balanced by the restoring force of the trap, producing a steady-state displacement from the trap center that scales linearly with velocity.[169] This larger displacement leads to enhanced fluctuations in both position and rotation, thereby increasing the measured SD.[49,170] The observed SD, however, does not scale linearly with velocity: the largest increase occurs between 0 and 1 μm/s, while further increases in speed produce only moderate growth in comparison. This suggests that additional factors beyond steady-state displacement, such as stage-induced vibrations, contribute to the fluctuations once the particle is in motion. Keeping the scan speed sufficiently low therefore preserves the sensitivity needed to resolve surface structure, and a scan speed of 1 μm/s was used in all subsequent measurements.

5.5.2 Profilometry of Microscale Structures

The reproducibility of the scanning approach is shown in **Figure 5.7b**, where the perimeter of a square with 10 μm sides was scanned twice at the speed of 1 μm/s over a featureless PDMS surface. In water, where the particle-surface separation is approximately 100 nm (as discussed in **Chapter 3**), allows for larger features to be scanned without destabilizing the trap. **Figure 5.8a, b**, shows an inverted pyramid in PDMS scanned at a speed of 1 μm/s, with the rotation-frequency readout clearly resolving the step-like features as the particle moves down into and back up out of the structure.

5.5.3 Tuning Particle-Surface Distance by Ionic Strength

Resolving smaller features requires reducing the particle–surface separation. This can be achieved by increasing the salt concentration of the surrounding solution, which screens electrostatic repulsion and allows the particle to approach the surface more closely. The trade-off is that the maximum feature size that can be traversed without destabilizing the trap is correspondingly reduced.

Figure 5.9a illustrates this trade-off. In this measurement, performed in undiluted PBS (NaCl concentration $\approx$ 137 mM), the particle is very close to the surface. As the trapped particle is translated toward a wall with a height of $\sim$250 nm, it does not

[a] In the regime where the optical trap can be approximated as harmonic, the restoring force is linear in displacement ($F_{res} = -kx$). At low Reynolds numbers, the hydrodynamic drag force is linear in velocity ($F_{drag} = \gamma v$, γ is the drag coefficient).

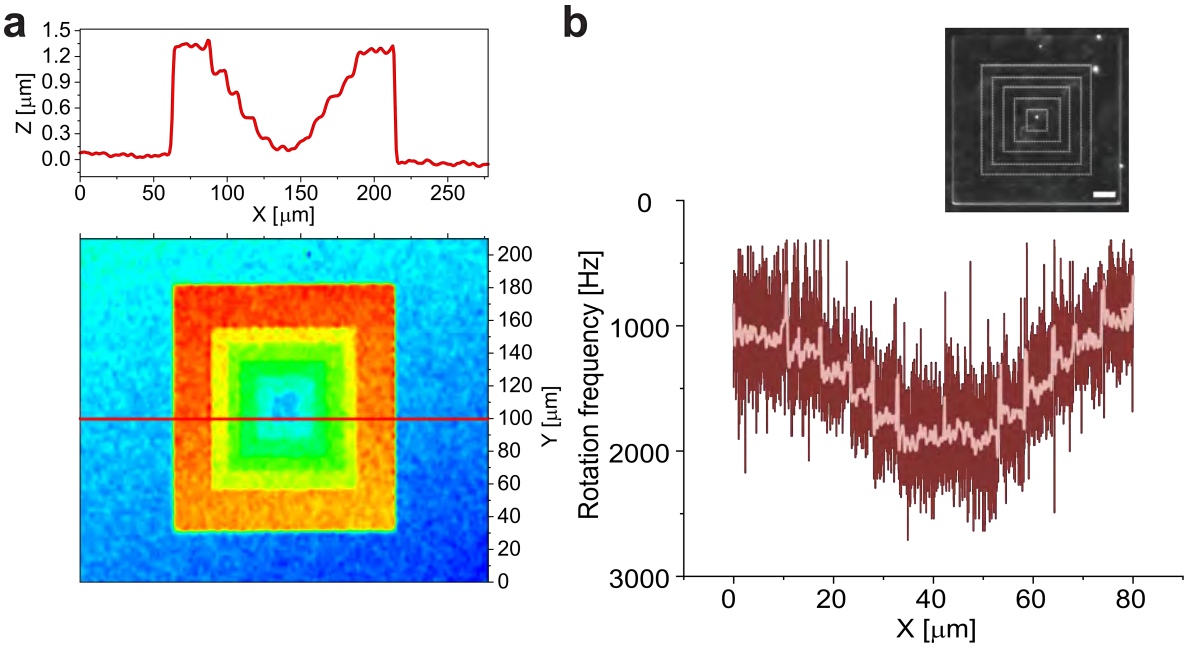

Figure 5.8: Profilometry of a microscale inverted pyramid structure in PDMS using a trapped gold nanorod scanned in water. **a** 3D optical profilometry of a PDMS structure with the same dimensions as in (**b**), measured using a Sensofar Neox system (Dr. Khosro Zangeneh Kamali). **b** Top: Dark-field image of the structure with edges highlighted in white (scale bar: 10 μm). Bottom: Rotation frequency as a function of position for an gold nanorod scanned over an inverted pyramid PDMS microstructure with 250 nm step size at 1 μm/s; dark trace shows extracted data, light trace shows smoothing. All data are analyzed using STFT (1024-point Hanning window) and smoothed with a third-order Savitzky–Golay filter (51-point window).

traverse the feature. Instead, it becomes increasingly displaced within the trap and ultimately escapes as the laser focus is moved across the wall.

At lower ionic strength, the equilibrium separation increases and finer features can be resolved. **Figure 5.9b-d**, shows a 3 μm square well of 100 nm depth, profiled by scanning the trapped particle back and forth across the feature nine times at a speed of 1 μm/s. This measurement is performed in a solution with a salt concentration of 0.001 M, corresponding to a particle–surface separation of approximately 40 nm.[66] Here the scattering intensity provides the readout, clearly resolving the particle entering and exiting the well.

The ability to control particle–surface separation through ionic strength highlights the flexibility of this approach, enabling access to different interaction regimes and length

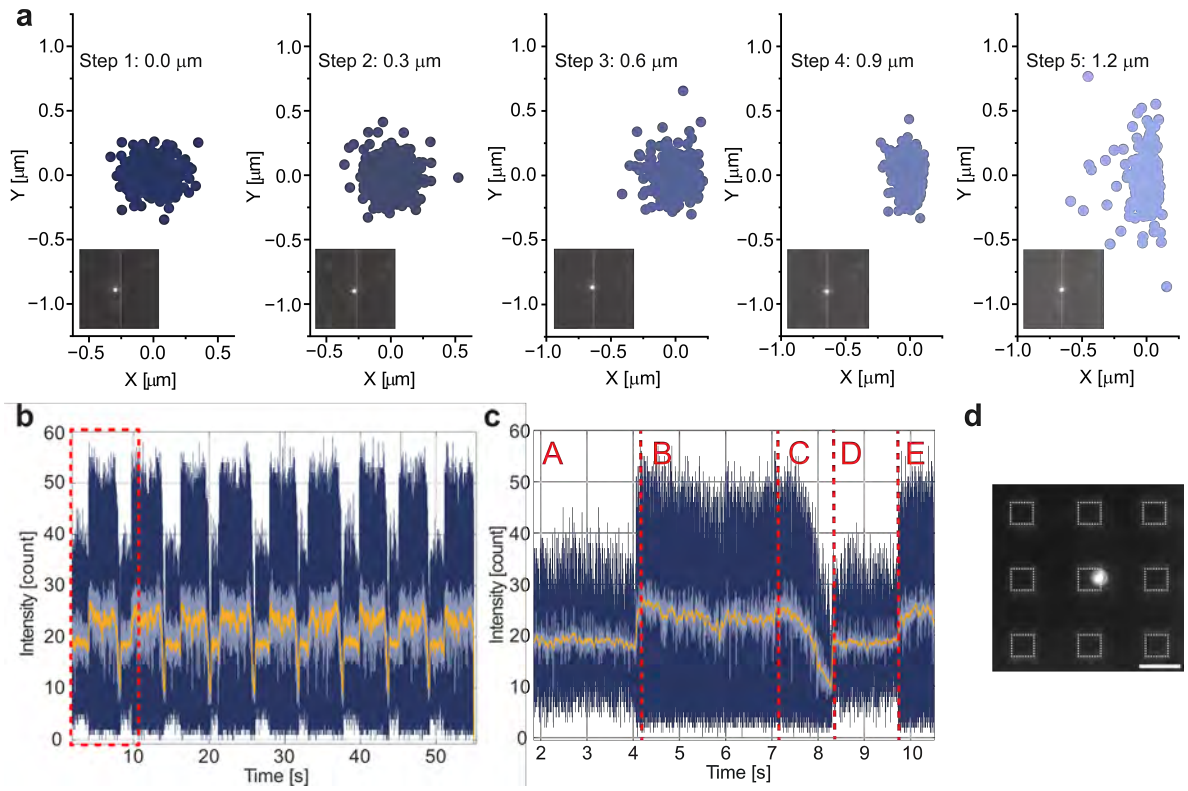

Figure 5.9: Tuning particle–surface separation via ionic strength to access different surface feature sizes. **a** Lateral position traces of a trapped gold nanorod as it is gradually moved toward a wall. The measurement was performed in undiluted PBS. **b** Intensity trace of an optically trapped gold nanorod scanned back and forth over a square glass well (3 μm side length, 100 nm deep) at a speed of 1 μm/s. The raw data are shown in dark blue, the light blue trace is smoothed using a third-order Savitzky–Golay (SG) filter (1001-point window), and the yellow trace is further smoothed using SG followed by a moving average filter. **c** Zoomed-in segment of the data in **b**, divided into regions to track the particle motion: (A) start of the measurement, (B) entry into the well, (C) exit from the well, (D) reversal of scan direction, and (E) re-entry into the well from the opposite direction. **d** Dark-field image of the measured glass well with the trapped gold nanorod. The edges of the well are highlighted in white for clarity. Scale bar: 5 μm.

scales. Together with the dual readout from rotation frequency and scattering intensity, this opens opportunities for high-resolution, non-contact probing of surface topography, with potential applications in studying both engineered nanoscale structures and soft systems such as cells.

5.6 Tracking Intracellular Gold Nanorods

In the previous sections, gold nanorods were used as actively driven probes, optically trapped and rotated to interrogate cellular nanomotion or surface topography. The same particles can also be used in a fundamentally different way, as passive cargo that has been internalized by cells, with their motion through the cytoplasm reporting on the intracellular transport machinery itself. In this regime, the role of the nanorod shifts from a controlled probe held in place by light to a freely moving tracer carried by the cell.

Following individual particles in this way relies on single-particle tracking (SPT), which is widely used to study biological and biomolecular processes inside living cells.[139] SPT requires that individual emitters be detected and tracked above the background. These emitters are often fluorescently labeled molecules or strongly scattering nanoparticles,[171–173] such as the gold nanorods used in our work. We use dark-field microscopy, in which the whole sample is illuminated simultaneously, allowing us to visualize multiple cells with hundreds of internalized nanorods. By combining deep-learning-based particle detection and trajectory linking across frames, we obtain large ensembles of trajectories that report on intracellular transport. Because individual particles rarely follow a single mode of motion throughout an entire trajectory, but instead switch between confined, diffusive, and directed transport, we further apply a Hidden Markov Model to segment each trajectory into its underlying motility states.

5.6.1 Particle Detection and Trajectory Reconstruction

In **Paper II**, intracellular cargo containing highly scattering gold nanorods in two prostate cancer cell lines were tracked using a deep-learning framework consisting of two neural network architectures: LodeSTAR[174] for particle detection and MAGIK[175] for trajectory reconstruction, shown in **Figure 5.10**. The training and application of the deep-learning models LodeSTAR and MAGIK were performed by Yuchao He.

LodeSTAR (Localization and Detection from Symmetries, Translations, And Rotations) is a self-supervised deep-learning method for object detection in microscopy. It is particularly advantageous in systems such as those studied in **Paper II**, where hundreds of particles must be detected within crowded environments.

LodeSTAR learns to detect particles without labeled examples, exploiting a simple

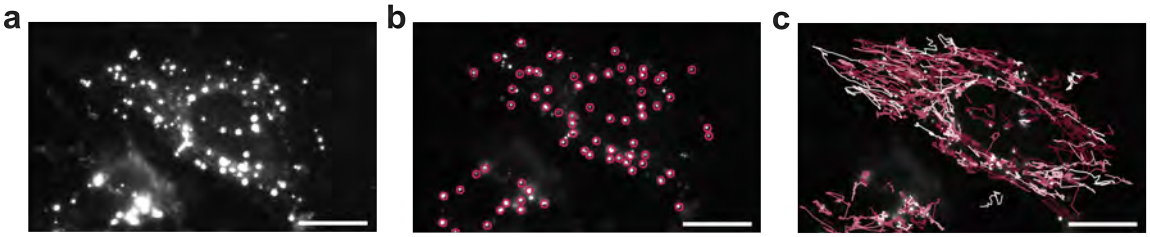

Figure 5.10: Detection and tracking of intracellular gold nanorods. **a** DF image of PC-3 prostate cancer cells with internalized gold nanorods ($\sim 70 \times 140$ nm). **b** Particle localization using LodeSTAR (pink circles) **c** Trajectory reconstruction using MAGIK. Scale bar in **a**, **b** and **c**: 20 μm.

but powerful idea: if you shift or rotate an image of a particle, the predicted particle position should shift or rotate by exactly the same amount. By generating multiple transformed versions of the same image and requiring the network's predictions to transform consistently, LodeSTAR learns to recognize particles purely from this geometric self-consistency — no manual annotation required. The final positions of the objects are then obtained through a weighted aggregation of local predictions derived from the network's vector-field and weight-map outputs, enabling precise and robust localization of the intracellular particles, in our case. Beyond providing centroid positions, LodeSTAR's localization output is also used to quantify the scattering intensity of each detected cluster, which serves as a qualitative indicator of cargo load. To account for uneven illumination and background signal, the intensity was obtained by integrating the signal within a 25×25 pixel region of interest (ROI) centered on each cluster. The ROI is chosen to capture the diffraction-limited scattering profile while avoiding overlap with neighboring particles, and the resulting intensities are averaged over each trajectory.

While LodeSTAR provides per-frame particle positions, studying intracellular transport requires stitching these detections together over time. This linking step is non-trivial in crowded environments, where particles can be closely spaced, cross paths, or briefly disappear from view. MAGIK (Motion Analysis through GNN Inductive Knowledge) approaches this by representing all detections across all frames as nodes in a graph, where candidate links between detections in nearby frames form the edges. A graph neural network then learns which candidate edges correspond to true particle identities, using both local motion features and the global context of the whole trajectory field.

5.6.2 Hidden Markov Model for Sub-Trajectory Analysis

Particles moving inside cells rarely exhibit a single, uniform mode of motion. A single vesicle might sit nearly stationary for several seconds, then be captured by a molecular motor and transported rapidly along a cytoskeletal filament, before being released again to diffuse more slowly. Quantifying intracellular transport therefore requires segmenting each trajectory into these distinct dynamical regimes. The difficulty is that the regime itself — whether a particle is confined, diffusing, or being actively transported — cannot be observed directly. We only see the particle's positions over time, not the underlying process driving its motion.

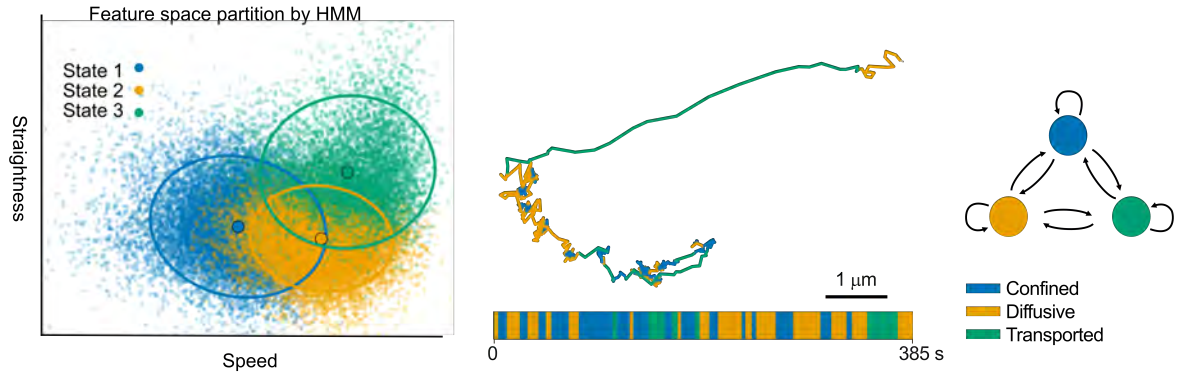

Figure 5.11: llustration of Hidden Markov Model state inference applied to intracellular gold nanorod trajectories. **Left:** Trajectory steps projected into the two-dimensional feature space defined by speed and straightness ratio. Each point corresponds to one time step, colored by its inferred hidden state (State 1, State 2, State 3). Ellipses show the fitted Gaussian emission distributions for each state. **Right:** A representative intracellular trajectory color-coded by inferred motility state, after physical interpretation of the states as confined (blue), diffusive (orange), and transported (green), illustrating the intermittent switching between these regimes over a 385 s acquisition. The bar below shows the full temporal sequence of state assignments. Inset: three-state HMM schematic showing possible transitions between states, including self-transitions. Scale bar: 1 μm.

The Hidden Markov Model (HMM) provides a framework for these kinds of problems, and has been used in several prior studies of intracellular transport.[176–178] The HMM assumes that at each time step, the system is in one of a small amount of *hidden states*, which in our case corresponds to three motility regimes.[179] The HMM assumes that the observed data, i.e the motion features of the trajectory, at each time step is drawn from a probability distribution that depends on which state the system is currently in. The states themselves evolve over time according to a *transition matrix*, which specifies

how likely the system is to stay in a certain state or switch to another. **Figure 5.11** illustrates this framework applied to a representative intracellular trajectory, where the inferred state sequence reveals the intermittent switching between motility regimes. The Markov assumption means that the probability of transitioning to a future state depends only on the current state, meaning the process has no memory of past states:

$$P(S_{t+1} = j \mid S_t = i, S_{t-1}, \ldots, S_1) = P(S_{t+1} = j \mid S_t = i). \tag{5.5}$$

Given a sequence of observations, the HMM framework can answer two types of questions. First, what are the parameters of the model, the emission distributions that describe the observations in each state, and the transition between each state? Second, given those parameters, what is the most likely sequence of hidden states that produce those parameters? The first question is answered during training and, the second during inference.

Feature Extraction. The observable features that are provided to the HMM are computed for each trajectory. The first is *step speed*, defined as the displacement between consecutive frames divided by the frame interval. This provides a time-resolved measure of particle motion and reflects how efficiently cargo is moved through the cell. The second feature is *straightness ratio* that computes directional persistence over a centered sliding window, comparing the net displacement over the window to the total path length, which generates a ratio between 0 (indicating tortuous movement) and 1 (perfectly straight movement). The two features are computed for each step in every trajectory, except the start and end point where the centered window cannot be defined. To place these features on comparable scales, both are standardized by subtracting the global mean and dividing by the global standard deviation (z-score normalization) computed across all trajectories in the dataset.

Model Specification. Trajectory dynamics are modeled using a discrete-time HMM with K hidden states, $S_t \in \{1, \ldots, K\}$, each corresponding to a distinct motility regime. The observed feature vector $\mathbf{f}_t$ at time t, is assumed to be generated from a multivariate Gaussian distribution whose mean and covariance depend on the current hidden state:

$$p(\mathbf{f}_t \mid S_t = k) = \mathcal{N}(\mathbf{f}_t \mid \boldsymbol{\mu}_k, \boldsymbol{\Sigma}_k), \tag{5.6}$$

where k indexes the discrete set of hidden states, and $\boldsymbol{\mu}_k$ and $\boldsymbol{\Sigma}_k$ denote the mean vector

and covariance matrix associated with state k, respectively. A full covariance structure is employed to capture correlations between features. The model further includes an initial state distribution $\boldsymbol{\pi}$ and a state transition matrix A

$$A = \begin{pmatrix} a_{11} & a_{12} & a_{13} \\ a_{21} & a_{22} & a_{23} \\ a_{31} & a_{32} & a_{33} \end{pmatrix}, \tag{5.7}$$

where $a_{ij} = P(S_{t+1} = j \mid S_t = i)$ denotes the probability of transitioning from state i to state j.

Training. The model parameters $\{\boldsymbol{\pi}, A, \boldsymbol{\mu}_k, \boldsymbol{\Sigma}_k\}$ are learned from the full ensemble of trajectories using the Baum–Welch algorithm, an Expectation–Maximization (EM) procedure.[180] In plain terms, Baum–Welch iteratively refines the model parameters to maximize the likelihood that the observed trajectories were produced by the model. Each iteration has two steps: the Expectation step computes, for every time point in every trajectory, the posterior probability that the system was in each hidden state at that moment (using the forward–backward algorithm); the Maximization step then uses those posteriors to update the transition probabilities and the emission distribution parameters.

Before training begins, the model must be initialized. We initialize the emission distributions by partitioning the observations into K groups based on step speed (low, intermediate, and high for $K = 3$) and computing the mean and covariance of the features within each group. The transition matrix is initialized with a bias toward self-transitions, reflecting the expectation that motility regimes typically persist over multiple frames rather than switching at every time step.

Inference. Once the model is trained, each trajectory is segmented into its sequence of motility states. The most probable sequence of hidden states given the observations, a single and temporally consistent state assignment for every time point, is computed using the Viterbi algorithm. In addition to this hard classification, the posterior state probabilities computed during the Expectation step provide a soft assignment: they quantify how confident the model is in each state assignment at each time point, which is useful for identifying ambiguous transitions.

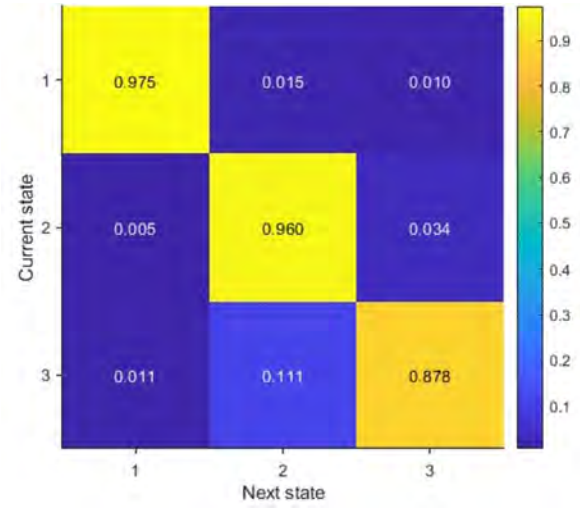

Figure 5.12: Empirical transition matrix for PEG-functionalized gold nanorods in PC-3 cells, derived from Viterbi-decoded state sequences. Rows indicate the current state and columns the next state, such that each row sums to one (within rounding). The large diagonal elements indicate strong temporal persistence of all three motility states, while the off-diagonal structure shows that transitions between the diffusive (state 2) and transported (state 3) states are more probable than direct transitions between confined (state 1) and transported (state 3).

An example of such a transition matrix from **Paper II**, derived from Viterbi-decoded trajectories of PEG-functionalized nanorods in PC-3 cells, is shown in **Figure 5.12**. The dominance of diagonal elements reflects the temporal persistence of each motility state, while the off-diagonal structure reveals which transitions between states are most probable.

Physical Interpretation. The three learned states are interpreted based on their characteristic feature values. Low speed with low directional persistence corresponds to confined motion; intermediate speed with low persistence corresponds to diffusive motion; high speed combined with high persistence corresponds to directed (actively transported) motion. This framework enables quantitative characterization of intracellular transport, including the extraction of trajectory-level statistics such as state occupancies, transition frequencies, and the durations of active transport episodes.

6

Summary of Appended Papers

The preceding chapters have established the physical principles and methodological framework underlying this thesis. The following sections describe how these tools were applied in practice, summarizing the main findings of the appended papers and the context in which they emerged. Where relevant, I have included some reflection on how the projects developed, since the path a project takes is often as informative as its outcome.

Paper I

Rotating Gold Nanomotors for High-Resolution Mapping of Subcellular Nanomotions

When I first joined the group as a Ph.D. student, a substantial body of work had already been established on the optical trapping of plasmonic nanoparticles. From early demonstrations of optically driven rotation[63,76] to ultrafast gold nanorod motors,[42] this work has laid the foundation for understanding key aspects of plasmonic trapping, including hot Brownian motion and photothermal effects.[81,181] It further enabled studies of non-equilibrium dynamics,[182] while also clarifying particle–surface interactions in 2D traps[66] and enabling applications such as probing DNA melting kinetics on single nanoparticles.[162] Building on this foundation, we aimed to extend these techniques to more complex environments and explore their application to the study of dynamics in living cells, which forms the basis of **Paper I**.

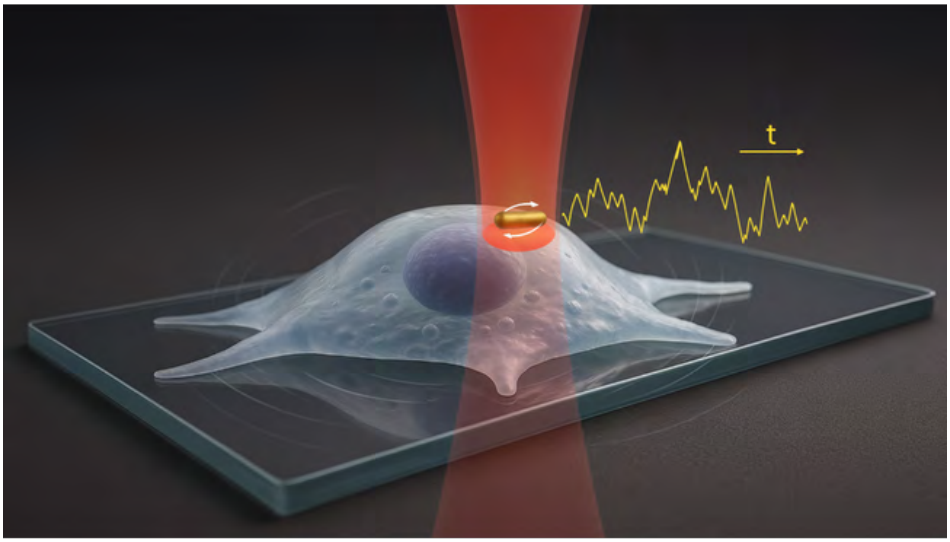

Figure 6.1: In Paper I, an optically trapped rotating nanomotor is used to detect nanoscale height fluctuations of living cells. Reproduced from.[28] © 2025 The Author(s). *Small Methods* published by Wiley-VCH GmbH.

By establishing an approximately linear relationship between the rotation frequency of the trapped nanomotor and its position along the optical axis, we realized that it could be used as a nanoscale ruler to measure height fluctuations of the cell membrane. The region probed during the measurements was highly localized, allowing the rotating nanomotor to function almost as a stethoscope for detecting sub-cellular nanomotions, providing a new approach to probing cellular dynamics.

The small probing area enabled us to investigate specific cellular compartments and assess whether the nanomotion patterns differed between them. We defined three regions: the nucleus, the perinuclear region, and the cell periphery. We observed clear heterogeneity in the nanomotion, with the largest fluctuations occurring in the perinuclear region. We believe this behavior is linked to active intracellular processes, such as the trafficking of vesicles and organelles, cytoskeletal rearrangements, and the dynamic activity of the endoplasmic reticulum and Golgi apparatus. In contrast, the cell periphery appeared to be the most mechanically stable region, consistent with its role in cell adhesion and structural integrity. We also observed variations within each compartment, indicating that these membrane fluctuations are transient in nature.

By analyzing the nanomotion data at higher temporal resolution, we were able to resolve short-lived oscillatory motions with characteristic frequencies of approximately 10 Hz. In addition, power spectral analysis (PSA) of the signals revealed $1/f^{\alpha}$ dynamics. A

shift in the exponent α was observed in nearly all measurements, suggesting a transition in the mechanical behavior of the cell from correlated (long-memory) dynamics to more stochastic (short-memory) motion. This project resulted in a method for studying both mechanical and dynamic processes in living cells, and it also introduced me to the fascinating and complex world of cellular dynamics.

Paper II

Gold Nanorod Tracking and Deep-learning Analysis Reveal Intracellular Transport Phenotypes in Therapy-resistant Prostate Cancer Cells

Paper II continues the exploration of cellular dynamics, but from a different angle. Here, the focus shifts from mechanical fluctuations at the membrane to transport processes inside the cell. The gold nanorods followed us into this project as well, though in a different role: rather than being driven as nanomotors, they are now passive probes, internalized by the cells and tracked as they move through the cytoplasm.

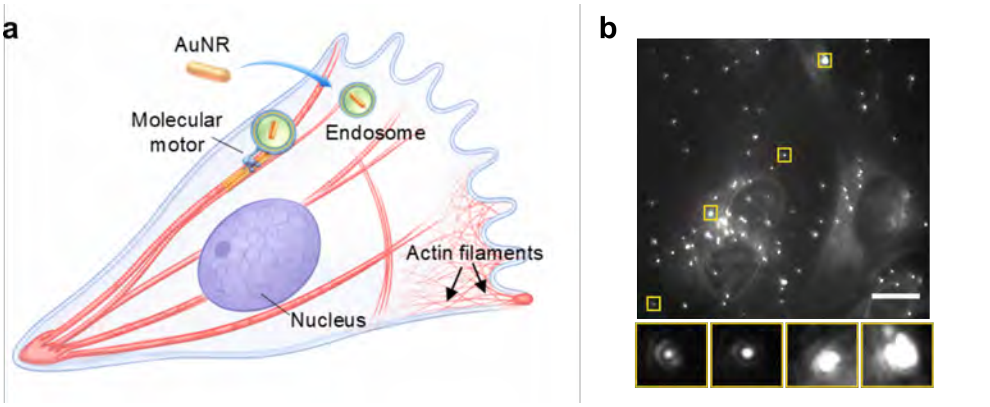

Figure 6.2: In Paper II, intracellular transport of gold nanorods is studied using a deep-learning framework for single-particle tracking. **a** Schematic illustration of intracellular trafficking in prostate cancer cells, showing AuNR-containing endocytic vesicles transported along microtubules and actin filaments. **b** A dark-field image of a PC-3 cell with internalized gold nanorods. Scale bar: 20 μm.

In **Paper II**, our objective was to compare intracellular transport between two prostate cancer cell lines, LNCaP-19 and PC-3. Both cell lines are androgen-independent; however, PC-3 cells exhibit a more aggressive than LNCaP-19 cells. We wanted to investigate whether transport differences could be detected without specific organelle staining,

instead relying on highly scattering nanoparticles. Furthermore, we also investigated whether different surface coatings influence intracellular transport.

Both cell lines were incubated with a large number of nanoparticles, resulting in hundreds of particles per cell. Their transport was characterized using dark-field imaging, exploiting the strong scattering of the nanorods, and the resulting trajectories were extracted using a deep-learning framework combining the self-supervised detector LodeSTAR with the graph neural network tracker MAGIK. To capture variations within trajectories and switching between transport modes, we further analyzed the data using a three-state Gaussian Hidden Markov Model (HMM), segmenting motion into confined, diffusive, and directed states. A single model was trained on pooled trajectories to ensure consistent state definitions across both cell types and surface coatings.

Using this analysis framework, we resolved clear differences in transport behavior between the two cell lines. Both exhibited confined, diffusive, and directed motion; however, PC-3 cells showed a higher prevalence of active transport, with more frequent and faster directed events compared to LNCaP-19. In addition, the spatial distribution of cargo differed markedly. In PC-3 cells, cargo was distributed throughout the cytoplasm with accumulation near the nucleus, whereas in LNCaP-19 it was more confined to the cell periphery, indicating differences in cargo organization and loading. Furthermore, we also observed that the surface coating of the nanorods have an effect on intracellular transport. PEG-functionalized rods exhibited longer confined intervals but maintained active transport over a wide range of cargo sizes, indicating a weaker dependence on cargo load. In contrast, SAM-functionalized rods favored rapid transport of lightly loaded vesicles, while larger cargos were more likely to remain confined or diffusive. These differences suggest that surface chemistry plays an important role in how nanoparticles interact with the intracellular transport machinery.

Taken together, this work demonstrates that plasmonic nanoparticle tracking combined with neural network–based analysis provides a powerful way to quantify intracellular transport and relate it to cellular state, establishing motion as a measurable physical phenotype. On a personal level, it has been fascinating to realize that what initially appears as random, busy motion within the cell in fact encodes the dynamics of a tightly regulated and highly organized intracellular machinery.

7

Conclusions and Outlook

7.1 Conclusions

The aim of this thesis has been to convey the versatility of plasmonic gold nanorods as probes of nanoscale dynamics and structure. By exploiting their translational and rotational Brownian motion together with optically driven rotation, we have shown that a single class of particle can be used to investigate a surprisingly broad range of systems, from nanoscale mechanical fluctuations of living cell membranes, to intracellular transport patterns in cancer cells, to static surface structures on engineered materials.

The theoretical foundation for this versatility was established in **Chapters 2**, **3**, and **4**. **Chapter** 2 described why gold nanorods are particularly well suited to this role, with their localized surface plasmon resonances in the visible and near-infrared regime giving rise to strong, tunable scattering and absorption. **Chapter 3** built on these properties to introduce the framework of optical trapping and rotation, in which the anisotropic geometry of the nanorods, combined with their plasmonic response, gives rise to optical forces and torques that allow them to be held and controlled with light. **Chapter 4** then addressed the additional considerations that arise when these particles are introduced into biological environments, where colloidal stability, surface functionalization, and protein corona formation determine their behavior and fate. **Chapter 5** introduced the experimental and analytical methods that build on this foundation, including optical trapping, dark-field tracking, deep-learning-based trajectory analysis, and rotational readout. These methods are applied across the studies summarized in **Chapter 6**.

Across the three studies, the same particle takes on three distinct roles — actively driven, passively tracked, and applied beyond biology. **Paper I** uses an optically driven nanorod as an active probe of mechanical activity at a cellular interface. **Paper II** uses internalized nanorods as passive tracers of intracellular transport across a population of particles. The profilometry study extends the same trapping-and-rotation configuration to non-biological surfaces, demonstrating that the underlying readout is not specific to living systems.

Taken together, these results demonstrate that a single plasmonic nanorod functions as a transducer linking optical interaction to its surroundings, translating mechanical, transport, and structural information into measurable optical signals. The versatility of this approach, and the richness of the information it provides, motivates the directions explored in the following section.

7.2 Outlook

The work presented in this thesis opens up many possible directions for further study. Here, I focus on a few that I find particularly compelling — directions that build on what the methods can already do, while pushing them toward richer detail and more directly interpretable signals.

A natural starting point for extending the work in **Paper I** lies in the experimental geometry itself. Adding axial tracking via a quadrant photodiode (QPD) would extend the measurement from a one-dimensional height signal to a full three-dimensional mapping of sub-cellular fluctuations, and would also provide much higher-bandwidth lateral tracking than our current camera-based detection, giving access to faster dynamics.[183] A complementary extension would be the introduction of a spatially separated second optical trap, which would make it possible to test whether nanomotion events are correlated between nearby locations, and in particular whether mechanical fluctuations propagate along the membrane.[184]

Beyond these technical upgrades, a recurring limitation across the studies in this thesis is that the nanorod reports on motion without directly reporting on the underlying cause of that motion. In **Paper I**, for instance, we observed clear heterogeneity in nanomotion across cellular compartments, but the specific processes responsible for the

fluctuations — organelle trafficking, cytoskeletal rearrangement, membrane remodeling — could only be inferred indirectly. A natural next step is to combine nanomotion detection with fluorescence imaging of specific organelles or cytoskeletal elements, so that mechanical fluctuations and their molecular context can be recorded simultaneously. Together, these extensions would move the platform from sensing that something is moving to resolving what is moving and how — turning sensitive but generic readouts into measurements that can be linked to specific cellular structures.

Like nanomotion detection, the profilometry method would also benefit from moving into biological environments. Because the technique is non-contact and the particle–surface separation can be tuned via ionic strength, it is in principle well suited to mapping soft surfaces such as cell membranes. Tuning the ionic strength adjusts the length scale being probed: high ionic strength brings the nanorod close to the surface and resolves small features, while lower ionic strength would allow coarser scans across larger regions, potentially even whole cells. Such measurements would, however, require fixed cells, since—as we saw in **Paper I**—living cells move too much for scanning to work on the relevant timescales. Combined with axial QPD readout, this approach could yield gentle, three-dimensional maps of cellular topography.

The methodology developed in **Paper II** could be extended in several ways. First, adding fluorescent tagging of endocytic compartments would make it possible to resolve not only where a nanorod is transported, but through which pathway it was internalized, enabling a more direct link between surface chemistry and uptake route. Second, our current analysis is restricted to the two lateral dimensions, whereas the intracellular transport network is inherently three-dimensional. Extending the measurement to full 3D tracking would give access to each cargo's complete trajectory, rather than its projection onto the imaging plane, and would allow a more complete characterization of diffusion modes, transport direction, and the local cellular environment through which cargo moves. Adapting recent single-particle 3D tracking approaches, which achieve nanometer localization precision with extended axial ranges,[185–187] to plasmonic scattering-based readout would be a valuable direction to pursue.

Beyond the measurement itself, there remains a wide range of biological parameters to explore. As discussed in **Chapter 4**, particle size, shape, and surface chemistry all influence how nanoparticles are taken up by cells and subsequently transported intracellularly. Tuning these parameters is therefore not only a means of optimizing particles

as probes, but also a way to deliberately bias which uptake pathways are engaged and which intracellular compartments the nanorods ultimately access.[188]

The effect of surface chemistry on intracellular transport observed in **Paper II** stood out to me, and a systematic study combining variations in nanorod size, aspect ratio, and surface functionalization would help disentangle which particle properties most strongly determine intracellular fate. A natural extension of this would be a more focused investigation in LNCaP and PC-3 cells, specifically targeting lysosomal transport, as altered trafficking within the endo-lysosomal system is a well-established feature of cancer progression,[189–192] making it a relevant and sensitive pathway to probe. Combining systematically tuned nanorods with fluorescently labeled lysosomes would enable direct correlation between particle design and lysosomal transport dynamics, providing a more mechanistic understanding of the differences previously observed between these cell lines.

The directions outlined here all build on the same observation that has run through this thesis: the motion of a single nanorod, observed through light, encodes a surprising amount of information about the system it explores. This thesis has shown that a single nanorod can reveal a great deal. The remaining task is to ask sharper questions of it.

Bibliography

[1] Tornéus E. Optically Driven Nanomotors for Cellular Motion Detection at the Nano-Scale . Gothenburg: Chalmers University of Technology; 2024.

[2] Gest H. The discovery of microorganisms by Robert Hooke and Antoni van Leeuwenhoek, Fellows of The Royal Society. Notes and Records of the Royal Society of London. 2004 2;58(2):187-201.

[3] Lane N. The unseen world: reflections on Leeuwenhoek (1677) 'Concerning little animals'. Philosophical Transactions of the Royal Society B: Biological Sciences. 2015 4;370(1666):20140344.

[4] Israelachvili JN. Intermolecular and surface forces. 3rd ed. Elsevier Inc.; 2011.

[5] S Mogre S, Brown AI, Koslover EF. Getting around the cell: Physical transport in the intracellular world. IOP Publishing Ltd; 2020.

[6] Chithrani DB, Dunne M, Stewart J, Allen C, Jaffray DA. Cellular uptake and transport of gold nanoparticles incorporated in a liposomal carrier. Nanomedicine: Nanotechnology, Biology, and Medicine. 2010;6(1):161-9.

[7] Purcell EM. Life at low Reynolds number. American Journal of Physics. 1977 2;45(1):3-11.

[8] Nolte DD. Coherent light scattering from cellular dynamics in living tissues. Reports on Progress in Physics. 2024 3;87(3):036601.

[9] Kühlbrandt W. The Resolution Revolution. Science. 2014 3;343(6178):1443-4.

[10] Cheng Y. Single-Particle Cryo-EM at Crystallographic Resolution. Cell. 2015 4;161(3):450-7.

[11] Alessandrini A, Facci P. AFM: a versatile tool in biophysics. Measurement Science and Technology. 2005 6;16(6):R65-92.

[12] Joshua AM, Cheng G, Lau EV. Soft matter analysis via atomic force microscopy (AFM): A review. Applied Surface Science Advances. 2023 10;17:100448.

[13] Booth MJ. Adaptive optical microscopy: the ongoing quest for a perfect image. Light: Science & Applications. 2014 4;3(4):e165-5.

[14] Lichtman JW, Conchello JA. Fluorescence microscopy. Nature Methods. 2005 2;2(12):910-9.

[15] Schermelleh L, Ferrand A, Huser T, Eggeling C, Sauer M, Biehlmaier O, et al. Super-resolution microscopy demystified. Nature Cell Biology. 2019 1;21(1):72-84.

[16] Rust MJ, Bates M, Zhuang X. Sub-diffraction-limit imaging by stochastic optical reconstruction microscopy (STORM). Nature Methods. 2006 10;3(10):793-5.

[17] Balzarotti F, Eilers Y, Gwosch KC, Gynnå AH, Westphal V, Stefani FD, et al. Nanometer resolution imaging and tracking of fluorescent molecules with minimal photon fluxes. Science. 2017 2;355(6325):606-12.

[18] Roca-Cusachs P, Conte V, Trepat X. Quantifying forces in cell biology. Nature Cell Biology. 2017 2;19(7):742-51.

[19] Wu PH, Aroush DRB, Asnacios A, Chen WC, Dokukin ME, Doss BL, et al. A comparison of methods to assess cell mechanical properties. Nature Methods. 2018 2;15(7):491-8.

[20] Català-Castro F, Schäffer E, Krieg M. Exploring cell and tissue mechanics with optical tweezers. Journal of Cell Science. 2022 2;135(15).

[21] Braun M, Bregulla AP, Günther K, Mertig M, Cichos F. Single Molecules Trapped by Dynamic Inhomogeneous Temperature Fields. Nano Letters. 2015 2;15(8):5499-505.

[22] Vos BE, Muenker TM, Betz T. Characterizing intracellular mechanics via optical tweezers-based microrheology. Current Opinion in Cell Biology. 2024 6;88.

[23] Hardiman W, Clark M, Friel C, Huett A, Pérez-Cota F, Setchfield K, et al. Living cells as a biological analog of optical tweezers – a non-invasive microrheology approach. Acta Biomaterialia. 2023 8;166:317-25.

[24] Kasas S, Ruggeri FS, Benadiba C, Maillard C, Stupar P, Tournu H, et al. Detecting nanoscale vibrations as signature of life. Proceedings of the National Academy of Sciences. 2015;112(2):378-81.

[25] Longo G, Alonso-Sarduy L, Rio LM, Bizzini A, Trampuz A, Notz J, et al. Rapid detection of bacterial resistance to antibiotics using AFM cantilevers as nanomechanical sensors. Nature Nanotechnology. 2013;8(7):522-6.

[26] Kohler AC, Venturelli L, Kannan A, Sanglard D, Dietler G, Willaert R, et al. Yeast Nanometric Scale Oscillations Highlights Fibronectin Induced Changes in C. albicans. Fermentation. 2020 2;6(1):28.

[27] Mustazzolu A, Venturelli L, Dinarelli S, Brown K, Floto RA, Dietler G, et al. A rapid unraveling of the activity and antibiotic susceptibility of mycobacteria. Antimicrobial Agents and Chemotherapy. 2019;63(3):02194-18.

[28] Tornéus E, Hamngren Blomqvist C, Beck Adiels C, Šípová-Jungová H. Rotating Gold Nanomotors for High-Resolution Mapping of Subcellular Nanomotions. Small Methods. 2025 12;9(12).

[29] Mark Fox. Optical Properties of Solids. 2nd ed. Oxford: Oxford University Press, Incorporated; 2010.

[30] Saleh BEA, Teich MC. Fundamentals of Photonics. Wiley; 1991.

[31] Yang HU, D'Archangel J, Sundheimer ML, Tucker E, Boreman GD, Raschke MB. Optical dielectric function of silver. Physical Review B - Condensed Matter and Materials Physics. 2015 2;91(23).

[32] Giannini V, Fernández-Domínguez AI, Heck SC, Maier SA. Plasmonic nanoantennas: Fundamentals and their use in controlling the radiative properties of nanoemitters; 2011.

[33] Bohren CF, Huffman DR. Absorption and Scattering of Light by Small Particles. John Wiley & Sons, Inc.; 1983.

[34] Oubre C, Nordlander P. Optical Properties of Metallodielectric Nanostructures Calculated Using the Finite Difference Time Domain Method. The Journal of Physical Chemistry B. 2004 2;108(46):17740-7.

[35] Johnson PB, Christy RW. Optical Constants of the Noble Metals. Physical Review B. 1972 12;6(12).

[36] Maier SA. Plasmonics: Fundamentals and Applications. Springer Science + Business Media LLC; 2007.

[37] Eustis S, El-Sayed MA. Why gold nanoparticles are more precious than pretty gold: Noble metal surface plasmon resonance and its enhancement of the radiative and nonradiative properties of nanocrystals of different shapes. Chem Soc Rev. 2006;35(3):209-17.

[38] Huang X, Jain PK, El-Sayed IH, El-Sayed MA. Plasmonic photothermal therapy (PPTT) using gold nanoparticles. Lasers in Medical Science. 2008 2;23(3):217-28.

[39] Tian Q, Jiang F, Zou R, Liu Q, Chen Z, Zhu M, et al. Hydrophilic Cu9S5 Nanocrystals: A Photothermal Agent with a 25.7% Heat Conversion Efficiency for Photothermal Ablation of Cancer Cells in Vivo. ACS Nano. 2011 2;5(12):9761-71.

[40] Setoura K, Ito S, Miyasaka H. Stationary bubble formation and Marangoni convection induced by CW laser heating of a single gold nanoparticle. Nanoscale. 2017;9(2):719-30.

[41] Dara P, Shanei M, Jones S, Käll M. Directional Control of Transient Flows Generated by Thermoplasmonic Bubble Nucleation. The Journal of Physical Chemistry C. 2023 2;127(35):17454-9.

[42] Shao L, Yang ZJ, Andren D, Johansson P, Kall M. Gold nanorod rotary motors driven by resonant light scattering. ACS Nano. 2015;9(12):12542-51.

[43] Qian W, Huang X, Kang B, El-Sayed MA. Dark-field light scattering imaging of living cancer cell component from birth through division using bioconjugated gold nanoprobes. Journal of Biomedical Optics. 2010 8;15(04):1.

[44] Meier M, Wokaun A. Enhanced fields on large metal particles: dynamic depolarization. Optics Letters. 1983 2;8(11):581.

[45] Ellen Zeman CJ, Schatz GC. An Accurate Electromagnetic Theory Study of Surface Enhancement Factors for; 1987.

[46] Kelly KL, Coronado E, Zhao LL, Schatz GC. The Optical Properties of Metal Nanoparticles: The Influence of Size, Shape, and Dielectric Environment. The Journal of Physical Chemistry B. 2003 1;107(3):668-77.

[47] Myroshnychenko V, Rodríguez-Fernández J, Pastoriza-Santos I, Funston AM, Novo C, Mulvaney P, et al. Modelling the optical response of gold nanoparticles. Chemical Society Reviews. 2008 2;37(9):1792-805.

[48] Baffou G, Quidant R. Thermo-plasmonics: using metallic nanostructures as nano-sources of heat. Laser & Photonics Reviews. 2013 2;7(2):171-87.

[49] Bustamante CJ, Chemla YR, Liu S, Wang MD. Optical tweezers in single-molecule biophysics. Nature Reviews Methods Primers. 2021 2;1(1):25.

[50] Ashkin A, Dziedzic JM, Bjorkholm JE, Chu S. Observation of a single-beam gradient force optical trap for dielectric particles. Optics Letters. 1986 2;11(5):288.

[51] Ashkin A. Acceleration and Trapping of Particles by Radiation Pressure. Physical Review Letters. 1970 2;24(4):156-9.

[52] Ashkin A, Dziedzic JM, Yamane T. Optical trapping and manipulation of single cells using infrared laser beams. Nature. 1987 2;330(6150):769-71.

[53] Nobel Prize Outreach AB. Arthur Ashkin - Facts; 2018. Available from: `https://www.nobelprize.org/prizes/physics/2018/ashkin/facts/`.

[54] Bustamante C, Smith SB, Liphardt J, Smith D. Single-molecule studies of DNA mechanics. Current Opinion in Structural Biology. 2000;10(3):279-85.

[55] Svoboda K, Block SM. Force and velocity measured for single kinesin molecules. Cell. 1994;77(5):773-84.

[56] Brenner S, Berger F, Rao L, Nicholas MP, Gennerich A. Force production of human cytoplasmic dynein is limited by its processivity. Science Advances. 2020 2;6(15).

[57] Wirtz D. Particle-Tracking Microrheology of Living Cells: Principles and Applications. Annual Review of Biophysics. 2009 2;38(1):301-26.

[58] Arbore C, Perego L, Sergides M, Capitanio M. Probing force in living cells with optical tweezers: from single-molecule mechanics to cell mechanotransduction. Biophysical Reviews. 2019;11:765-82.

[59] Shinde A, Illath K, Gupta P, Shinde P, Lim KT, Nagai M, et al. A Review of Single-Cell Adhesion Force Kinetics and Applications. Cells. 2021 2;10(3):577.

[60] Jones PH, Maragò OM, Volpe G. Optical Tweezers: Principles and Applications. Cambridge University Press; 2015.

[61] Ashkin A. Forces of a single-beam gradient laser trap on a dielectric sphere in the ray optics regime. Biophysical Journal. 1992 2;61(2):569-82.

[62] Novotny L, Hecht B. Principles of Nano-Optics. Cambridge University Press; 2012.

[63] Lehmuskero A, Johansson P, Rubinsztein-Dunlop H, Tong L, Käll M. Laser trapping of colloidal metal nanoparticles. ACS Nano. 2015 2;9(4):3453-69.

[64] Arias-González JR, Nieto-Vesperinas M. Optical forces on small particles: attractive and repulsive nature and plasmon-resonance conditions. Journal of the Optical Society of America A. 2003 2;20(7):1201.

[65] Svoboda K, Block SM. Optical trapping of metallic Rayleigh particles. Optics Letters. 1994 2;19(13):930.

[66] Andrén D, Odebo Länk N, Šípová-Jungová H, Jones S, Johansson P, Käll M. Surface Interactions of Gold Nanoparticles Optically Trapped against an Interface. The Journal of Physical Chemistry C. 2019 7;123(26):16406-14.

[67] Beth RA. Mechanical Detection and Measurement of the Angular Momentum of Light. Physical Review. 1936 7;50(2):115-25.

[68] Friese MEJ, Enger J, Rubinsztein-Dunlop H, Heckenberg NR. Optical angular-momentum transfer to trapped absorbing particles. Physical Review A. 1996 8;54(2):1593-6.

[69] Šípová-Jungová H, Andrén D, Jones S, Käll M. Nanoscale Inorganic Motors Driven by Light: Principles, Realizations, and Opportunities. Chemical Reviews. 2020 2;120(1):269-87.

[70] Bruce GD, Rodríguez-Sevilla P, Dholakia K. Initiating revolutions for optical manipulation: the origins and applications of rotational dynamics of trapped particles. Advances in Physics: X. 2021 1;6(1).

[71] Friese MEJ, Nieminen TA, Heckenberg NR, Rubinsztein-Dunlop H. Optical alignment and spinning of laser-trapped microscopic particles. Nature. 1998 7;394(6691):348-50.

[72] Marston PL, Crichton JH. Radiation torque on a sphere caused by a circularly-polarized electromagnetic wave. Physical Review A. 1984 11;30(5):2508-16.

[73] Allen L, Beijersbergen MW, Spreeuw RJC, Woerdman JP. Orbital angular momentum of light and the transformation of Laguerre-Gaussian laser modes. Physical Review A. 1992 6;45(11):8185-9.

[74] He H, Friese MEJ, Heckenberg NR, Rubinsztein-Dunlop H. Direct Observation of Transfer of Angular Momentum to Absorptive Particles from a Laser Beam with a Phase Singularity. Physical Review Letters. 1995 7;75(5):826-9.

[75] Lehmuskero A, Li Y, Johansson P, Käll M. Plasmonic particles set into fast orbital motion by an optical vortex beam. Optics Express. 2014 2;22(4):4349.

[76] Lehmuskero A, Ogier R, Gschneidtner T, Johansson P, Käll M. Ultrafast Spinning of Gold Nanoparticles in Water Using Circularly Polarized Light. Nano Letters. 2013 2;13(7):3129-34.

[77] Lee YE, Fung KH, Jin D, Fang NX. Optical torque from enhanced scattering by multipolar plasmonic resonance. Nanophotonics. 2014 2;3(6):343-50.

[78] Kong D, Lin W, Pan Y, Zhang K. Swimming motion of rod-shaped magnetotactic bacteria: the effects of shape and growing magnetic moment. Frontiers in Microbiology. 2014;5.

[79] Einstein A. Über die von der molekularkinetischen Theorie der Wärme geforderte Bewegung von in ruhenden Flüssigkeiten suspendierten Teilchen. Annalen der Physik. 1905 2;322(8):549-60.

[80] Fogel'son RL, Likhachev ER. Temperature dependence of viscosity. Technical Physics. 2001 2;46(8):1056-9.

[81] Hajizadeh F, Shao L, Andrén D, Johansson P, Rubinsztein-Dunlop H, Käll M. Brownian fluctuations of an optically rotated nanorod. Optica. 2017;4(7):746-51.

[82] Rings D, Schachoff R, Selmke M, Cichos F, Kroy K. Hot Brownian motion. Physical Review Letters. 2010 8;105(9).

[83] Rings D, Chakraborty D, Kroy K. Rotational hot Brownian motion. New Journal of Physics. 2012 5;14(5):053012.

[84] Falasco G, Gnann MV, Rings D, Kroy K. Effective temperatures of hot Brownian motion. Physical Review E - Statistical, Nonlinear, and Soft Matter Physics. 2014 9;90(3).

[85] Rodríguez-Sevilla P, Arita Y, Liu X, Jaque D, Dholakia K. The Temperature of an Optically Trapped, Rotating Microparticle. ACS Photonics. 2018 9;5(9):3772-8.

[86] Arita Y, Richards JM, Mazilu M, Spalding GC, Skelton Spesyvtseva SE, Craig D, et al. Rotational Dynamics and Heating of Trapped Nanovaterite Particles. ACS Nano. 2016 12;10(12):11505-10.

[87] Moore TL, Rodriguez-Lorenzo L, Hirsch V, Balog S, Urban D, Jud C, et al. Nanoparticle colloidal stability in cell culture media and impact on cellular interactions. Chemical Society Reviews. 2015;44(17):6287-305.

[88] Ma Y, Hong J, Ding Y. Biological Behavior Regulation of Gold Nanoparticles via the Protein Corona. Advanced Healthcare Materials. 2020 3;9(6).

[89] Weissleder R. A clearer vision for in vivo imaging. Nature Biotechnology. 2001 4;19(4):316-7.

[90] Zheng J, Cheng X, Zhang H, Bai X, Ai R, Shao L, et al. Gold Nanorods: The Most Versatile Plasmonic Nanoparticles. Chemical Reviews. 2021 11;121(21):13342-453.

[91] Zhang Y, Qian J, Wang D, Wang Y, He S. Multifunctional Gold Nanorods with Ultrahigh Stability and Tunability for InVivo Fluorescence Imaging, SERS Detection, and Photodynamic Therapy. Angewandte Chemie International Edition. 2013 1;52(4):1148-51.

[92] Wang H, Huff TB, Zweifel DA, He W, Low PS, Wei A, et al. In vitro and in vivo two-photon luminescence imaging of single gold nanorods; 2005. 44.

[93] Chen YS, Zhao Y, Yoon SJ, Gambhir SS, Emelianov S. Miniature gold nanorods for photoacoustic molecular imaging in the second near-infrared optical window. Nature Nanotechnology. 2019 5;14(5):465-72.

[94] Lee C, Hwang HS, Lee S, Kim B, Kim JO, Oh KT, et al. Rabies Virus-Inspired Silica-Coated Gold Nanorods as a Photothermal Therapeutic Platform for Treating Brain Tumors. Advanced Materials. 2017 4;29(13).

[95] Dickerson EB, Dreaden EC, Huang X, El-Sayed IH, Chu H, Pushpanketh S, et al. Gold nanorod assisted near-infrared plasmonic photothermal therapy (PPTT) of squamous cell carcinoma in mice. Cancer Letters. 2008 9;269(1):57-66.

[96] Venkatesan R, Pichaimani A, Hari K, Balasubramanian PK, Kulandaivel J, Premkumar K. Doxorubicin conjugated gold nanorods: a sustained drug delivery carrier for improved anticancer therapy. J Mater Chem B. 2013;1(7):1010-8.

[97] Huang X, Wu S, Ke X, Li X, Du X. Phosphonated Pillar[5]arene-Valved Mesoporous Silica Drug Delivery Systems. ACS Applied Materials & Interfaces. 2017 6;9(23):19638-45.

[98] Zhao Y, Guo Q, Dai X, Wei X, Yu Y, Chen X, et al. A Biomimetic Non-Antibiotic Approach to Eradicate Drug-Resistant Infections. Advanced Materials. 2019 2;31(7).

[99] Uusitalo M, Eriksson G, Hulander M, Andersson M. Gold Nanorods as Photothermal Antibacterial Materials. ACS Applied Nano Materials. 2025 2;8(7):3661-70.

[100] Zhao YQ, Sun Y, Zhang Y, Ding X, Zhao N, Yu B, et al. Well-Defined Gold Nanorod/Polymer Hybrid Coating with Inherent Antifouling and Photothermal Bactericidal Properties for Treating an Infected Hernia. ACS Nano. 2020 2;14(2):2265-75.

[101] Napper DH. Steric stabilization. Journal of Colloid and Interface Science. 1977 2;58(2):390-407.

[102] Grabinski C, Schaeublin N, Wijaya A, D'Couto H, Baxamusa SH, Hamad-Schifferli K, et al. Effect of Gold Nanorod Surface Chemistry on Cellular Response. ACS Nano. 2011 4;5(4):2870-9.

[103] Wang L, Jiang X, Ji Y, Bai R, Zhao Y, Wu X, et al. Surface chemistry of gold nanorods: Origin of cell membrane damage and cytotoxicity. Nanoscale. 2013 9;5(18):8384-91.

[104] Schulz F, Friedrich W, Hoppe K, Vossmeyer T, Weller H, Lange H. Effective PEGylation of gold nanorods. Nanoscale. 2016 4;8(13):7296-308.

[105] Schollbach M, Zhang F, Roosen-Runge F, Skoda MWA, Jacobs RMJ, Schreiber F. Gold nanoparticles decorated with oligo(ethylene glycol) thiols: Surface charges and interactions with proteins in solution. Journal of Colloid and Interface Science. 2014 7;426:31-8.

[106] Harder P, Grunze M, Dahint R, Whitesides GM, Laibinis PE. Molecular Conformation in Oligo(ethylene glycol)-Terminated Self-Assembled Monolayers on Gold and Silver Surfaces Determines Their Ability To Resist Protein Adsorption. The Journal of Physical Chemistry B. 1998 1;102(2):426-36.

[107] Manson J, Kumar D, Meenan BJ, Dixon D. Polyethylene glycol functionalized gold nanoparticles: The influence of capping density on stability in various media. Gold Bulletin. 2011;44(2):99-105.

[108] Bashiri G, Padilla MS, Swingle KL, Shepherd SJ, Mitchell MJ, Wang K. Nanoparticle protein corona: from structure and function to therapeutic targeting. Lab on a Chip. 2023;23(6):1432-66.

[109] Walczyk D, Bombelli FB, Monopoli MP, Lynch I, Dawson KA. What the Cell "Sees" in Bionanoscience. Journal of the American Chemical Society. 2010 4;132(16):5761-8.

[110] Wang H, Ma R, Nienhaus K, Nienhaus GU. Formation of a Monolayer Protein Corona around Polystyrene Nanoparticles and Implications for Nanoparticle Agglomeration. Small. 2019 5;15(22).

[111] Vilanova O, Martinez-Serra A, Monopoli MP, Franzese G. Characterizing the hard and soft nanoparticle-protein corona with multilayer adsorption. Frontiers in Nanotechnology. 2025 1;6.

[112] Mohammad-Beigi H, Hayashi Y, Zeuthen CM, Eskandari H, Scavenius C, Juul-Madsen K, et al. Mapping and identification of soft corona proteins at nanoparticles and their impact on cellular association. Nature Communications. 2020 9;11(1):4535.

[113] Boyles MSP, Kristl T, Andosch A, Zimmermann M, Tran N, Casals E, et al. Chitosan functionalisation of gold nanoparticles encourages particle uptake and induces cytotoxicity and pro-inflammatory conditions in phagocytic cells, as well as enhancing particle interactions with serum components. Journal of Nanobiotechnology. 2015 12;13(1):84.

[114] Nel AE, Mädler L, Velegol D, Xia T, Hoek EMV, Somasundaran P, et al. Understanding biophysicochemical interactions at the nano–bio interface. Nature Materials. 2009 7;8(7):543-57.

[115] Schöttler S, Landfester K, Mailänder V. Controlling the Stealth Effect of Nanocarriers through Understanding the Protein Corona. Angewandte Chemie International Edition. 2016 7;55(31):8806-15.

[116] Barbir R, Jiménez RR, Martín-Rapún R, Strasser V, Domazet Jurašin D, Dabelić S, et al. Interaction of Differently Sized, Shaped, and Functionalized Silver and Gold Nanoparticles with Glycosylated versus Nonglycosylated Transferrin. ACS Applied Materials & Interfaces. 2021 6;13(23):27533-47.

[117] Deng ZJ, Liang M, Toth I, Monteiro MJ, Minchin RF. Molecular Interaction of Poly(acrylic acid) Gold Nanoparticles with Human Fibrinogen. ACS Nano. 2012 10;6(10):8962-9.

[118] Piella J, Bastús NG, Puntes V. Size-Dependent Protein–Nanoparticle Interactions in Citrate-Stabilized Gold Nanoparticles: The Emergence of the Protein Corona. Bioconjugate Chemistry. 2017 1;28(1):88-97.

[119] García-Álvarez R, Hadjidemetriou M, Sánchez-Iglesias A, Liz-Marzán LM, Kostarelos K. In vivo formation of protein corona on gold nanoparticles. the effect of their size and shape. Nanoscale. 2018 1;10(3):1256-64.

[120] Behzadi S, Serpooshan V, Tao W, Hamaly MA, Alkawareek MY, Dreaden EC, et al.. Cellular uptake of nanoparticles: Journey inside the cell. Royal Society of Chemistry; 2017.

[121] Sousa De Almeida M, Susnik E, Drasler B, Taladriz-Blanco P, Petri-Fink A, Rothen-Rutishauser B. Understanding nanoparticle endocytosis to improve targeting strategies in nanomedicine. Royal Society of Chemistry; 2021.

[122] Sahay G, Alakhova DY, Kabanov AV. Endocytosis of nanomedicines. Journal of Controlled Release. 2010 8;145(3):182-95.

[123] Iversen TG, Skotland T, Sandvig K. Endocytosis and intracellular transport of nanoparticles: Present knowledge and need for future studies. Nano Today. 2011 4;6(2):176-85.

[124] Conner SD, Schmid SL. Regulated portals of entry into the cell. Nature. 2003 3;422(6927):37-44.

[125] Ungewickell E, Branton D. Assembly units of clathrin coats. Nature. 1981 1;289(5796):420-2.

[126] Kumari S, MG S, Mayor S. Endocytosis unplugged: multiple ways to enter the cell. Cell Research. 2010 3;20(3):256-75.

[127] Lim JP, Gleeson PA. Macropinocytosis: an endocytic pathway for internalising large gulps. Immunology & Cell Biology. 2011 11;89(8):836-43.

[128] Swanson JA. Shaping cups into phagosomes and macropinosomes. Nature Reviews Molecular Cell Biology. 2008 8;9(8):639-49.

[129] Zhu M, Nie G, Meng H, Xia T, Nel A, Zhao Y. Physicochemical Properties Determine Nanomaterial Cellular Uptake, Transport, and Fate. Accounts of Chemical Research. 2013 3;46(3):622-31.

[130] Chithrani BD, Ghazani AA, Chan WCW. Determining the Size and Shape Dependence of Gold Nanoparticle Uptake into Mammalian Cells. Nano Letters. 2006 4;6(4):662-8.

[131] Jiang W, Kim BYS, Rutka JT, Chan WCW. Nanoparticle-mediated cellular response is size-dependent. Nature Nanotechnology. 2008 3;3(3):145-50.

[132] Chithrani BD, Chan WCW. Elucidating the Mechanism of Cellular Uptake and Removal of Protein-Coated Gold Nanoparticles of Different Sizes and Shapes. Nano Letters. 2007 6;7(6):1542-50.

[133] Dasgupta S, Auth T, Gompper G. Shape and orientation matter for the cellular uptake of nonspherical particles. Nano Letters. 2014 2;14(2):687-93.

[134] Banerjee A, Qi J, Gogoi R, Wong J, Mitragotri S. Role of nanoparticle size, shape and surface chemistry in oral drug delivery. Journal of Controlled Release. 2016 9;238:176-85.

[135] Zhou H, Gong X, Lin H, Chen H, Huang D, Li D, et al. Gold nanoparticles impair autophagy flux through shape-dependent endocytosis and lysosomal dysfunction. Journal of Materials Chemistry B. 2018;6(48):8127-36.

[136] Arvizo RR, Miranda OR, Thompson MA, Pabelick CM, Bhattacharya R, Robertson JD, et al. Effect of Nanoparticle Surface Charge at the Plasma Membrane and Beyond. Nano Letters. 2010 7;10(7):2543-8.

[137] Li Y, Chen X, Gu N. Computational Investigation of Interaction between Nanoparticles and Membranes: Hydrophobic/Hydrophilic Effect. The Journal of Physical Chemistry B. 2008 12;112(51):16647-53.

[138] Tao W, Zhang J, Zeng X, Liu D, Liu G, Zhu X, et al. Blended Nanoparticle System Based on Miscible Structurally Similar Polymers: A Safe, Simple, Targeted, and Surprisingly High Efficiency Vehicle for Cancer Therapy. Advanced Healthcare Materials. 2015 6;4(8):1203-14.

[139] Simon F, Weiss LE, van Teeffelen S. A guide to single-particle tracking. Nature Reviews Methods Primers. 2024 9;4(1):66.

[140] Berg HC. Random Walks in Biology. Princeton, NJ: Princeton University Press; 1993.

[141] Metzler R, Klafter J. The random walk's guide to anomalous diffusion: a fractional dynamics approach. Physics Reports. 2000 12;339(1):1-77.

[142] Aw TY, Jones DP. ATP concentration gradients in cytosol of liver cells during hypoxia. American Journal of Physiology-Cell Physiology. 1985 11;249(5):C385-92.

[143] Phillips R, Kondev J, Theriot J. Physical Biology of the Cell. 2nd ed. New York: Garland Science, Taylor & Francis Group; 2012.

[144] Cooper ST, McNeil PL. Membrane Repair: Mechanisms and Pathophysiology. Physiological Reviews. 2015 10;95(4):1205-40.

[145] Carlton JG, Jones H, Eggert US. Membrane and organelle dynamics during cell division. Nature Reviews Molecular Cell Biology. 2020 3;21(3):151-66.

[146] Bálint Verdeny Vilanova I, Sandoval Álvarez Lakadamyali M. Correlative live-cell and superresolution microscopy reveals cargo transport dynamics at microtubule intersections. Proceedings of the National Academy of Sciences. 2013 2;110(9):3375-80.

[147] Misgeld T, Schwarz TL. Mitostasis in Neurons: Maintaining Mitochondria in an Extended Cellular Architecture. Neuron. 2017 11;96(3):651-66.

[148] Guimaraes SC, Schuster M, Bielska E, Dagdas G, Kilaru S, Meadows BRA, et al. Peroxisomes, lipid droplets, and endoplasmic reticulum "hitchhike" on motile early endosomes. Journal of Cell Biology. 2015 12;211(5):945-54.

[149] Bandyopadhyay D, Cyphersmith A, Zapata JA, Kim YJ, Payne CK. Lysosome transport as a function of lysosome diameter. PLoS ONE. 2014 1;9(1).

[150] Brangwynne CP, MacKintosh FC, Weitz DA. Force fluctuations and polymerization dynamics of intracellular microtubules. Proceedings of the National Academy of Sciences. 2007 10;104(41):16128-33.

[151] Hirokawa N. Kinesin and Dynein Superfamily Proteins and the Mechanism of Organelle Transport. Science. 1998 1;279(5350):519-26.

[152] Hancock WO. Bidirectional cargo transport: moving beyond tug of war. Nature Reviews Molecular Cell Biology. 2014 9;15(9):615-28.

[153] Hendricks AG, Perlson E, Ross JL, Schroeder HW, Tokito M, Holzbaur ELF. Motor Coordination via a Tug-of-War Mechanism Drives Bidirectional Vesicle Transport. Current Biology. 2010 4;20(8):697-702.

[154] Ye X, Zheng C, Chen J, Gao Y, Murray CB. Using Binary Surfactant Mixtures To Simultaneously Improve the Dimensional Tunability and Monodispersity in the Seeded Growth of Gold Nanorods. Nano Letters. 2013 2;13(2):765-71.

[155] Alkilany AM, Murphy CJ. Toxicity and cellular uptake of gold nanoparticles: what we have learned so far? Journal of Nanoparticle Research. 2010 2;12(7):2313-33.

[156] Alkilany AM, Nagaria PK, Hexel CR, Shaw TJ, Murphy CJ, Wyatt MD. Cellular Uptake and Cytotoxicity of Gold Nanorods: Molecular Origin of Cytotoxicity and Surface Effects. Small. 2009 3;5(6):701-8.

[157] Homola J, editor. Surface Plasmon Resonance Based Sensors. vol. 4. Berlin, Heidelberg: Springer Berlin Heidelberg; 2006.

[158] Gustavsson H, Welén K, Damber J. Transition of an androgen-dependent human prostate cancer cell line into an androgen-independent subline is associated with increased angiogenesis. The Prostate. 2005 3;62(4):364-73.

[159] Moustafa TE, Belote RL, Polanco ER, Judson-Torres RL, Zangle TA. Quadrant darkfield for label-free imaging of intracellular puncta. Journal of Biomedical Optics. 2024 11;29(11).

[160] Nan X, Sims PA, Xie XS. Organelle Tracking in a Living Cell with Microsecond Time Resolution and Nanometer Spatial Precision. ChemPhysChem. 2008 2;9(5):707-12.

[161] Wilson JD, Cottrell WJ, Foster TH. Index-of-refraction-dependent subcellular light scattering observed with organelle-specific dyes. Journal of Biomedical Optics. 2007;12(1):014010.

[162] Šípová H, Shao L, Odebo Länk N, Andrén D, Käll M. Photothermal DNA Release from Laser-Tweezed Individual Gold Nanomotors Driven by Photon Angular Momentum. ACS Photonics. 2018;5(6):2168-75.

[163] Oppenheim AV, Willsky AS, Nawab SH. Signals and systems. 2nd ed. Harlow, Essex: Pearson Education Ltd; 2014.

[164] Cohen L. Time-frequency analysis. vol. 778. Prentice Hall PTR New Jersey; 1995.

[165] Gupta V, Mittal M. Respiratory signal analysis using PCA, FFT and ARTFA. In: 2016 International Conference on Electrical Power and Energy Systems (ICEPES). IEEE; 2016. p. 221-5.

[166] Papoulis A, Pillai SU. Probability, Random Variables, and Stochastic Processes. 4th ed. Boston: McGraw-Hill, cop. 2002; 2002.

[167] Harris FJ. On the use of windows for harmonic analysis with the discrete Fourier transform. Proceedings of the IEEE. 1978;66(1):51-83.

[168] Allen JB, Rabiner LR. A unified approach to short-time Fourier analysis and synthesis. Proceedings of the IEEE. 1977;65(11):1558-64.

[169] Gieseler J, Gomez-Solano JR, Magazzù A, Pérez Castillo I, Pérez García L, Gironella-Torrent M, et al. Optical tweezers — from calibration to applications: a tutorial. Advances in Optics and Photonics. 2021 3;13(1):74.

[170] Baro N, Mondal PP. Planar lightsheet optical tweezer pLOT for 2D trapping and imaging of freely-moving live cells. Communications Biology. 2025 12;8(1):1763.

[171] Qiu K, Du Y, Liu J, Guan JL, Chao H, Diao J. Super-resolution observation of lysosomal dynamics with fluorescent gold nanoparticles. Theranostics. 2020;10(13):6072-81.

[172] Levi V, Gratton E. Exploring dynamics in living cells by tracking single particles; 2007.

[173] Tkachenko AG, Xie H, Liu Y, Coleman D, Ryan J, Glomm WR, et al. Cellular trajectories of peptide-modified gold particle complexes: Comparison of nuclear localization signals and peptide transduction domains. Bioconjugate Chemistry. 2004;15(3):482-90.

[174] Midtvedt B, Pineda J, Skärberg F, Olsén E, Bachimanchi H, Wesén E, et al. Single-shot self-supervised object detection in microscopy. Nature Communications. 2022 12;13(1).

[175] Pineda J, Midtvedt B, Bachimanchi H, Noé S, Midtvedt D, Volpe G, et al. Geometric deep learning reveals the spatiotemporal features of microscopic motion. Nature Machine Intelligence. 2023 1;5(1):71-82.

[176] Das R, Cairo CW, Coombs D. A hidden Markov model for single particle tracks quantifies dynamic interactions between LFA-1 and the actin cytoskeleton. PLoS Computational Biology. 2009;5(11).

[177] Röding M, Guo M, Weitz DA, Rudemo M, Särkkä A. Identifying directional persistence in intracellular particle motion using Hidden Markov Models. Mathematical Biosciences. 2014;248(1):140-5.

[178] Monnier N, Barry Z, Park HY, Su KC, Katz Z, English BP, et al. Inferring transient particle transport dynamics in live cells. Nature Methods. 2015 8;12(9):838-40.

[179] Bilmes JA. A Gentle Tutorial of the EM Algorithm and its Application to Parameter Estimation for Gaussian Mixture and Hidden Markov Models; 1998.

[180] Rabiner LR. A Tutorial on Hidden Markov Models and Selected Applications in Speech Recognition. Proceedings of the IEEE. 1989;77.

[181] Andren D, Shao L, Odebo Lank N, Acimovic SS, Johansson P, Kall M. Probing photothermal effects on optically trapped gold nanorods by simultaneous plasmon spectroscopy and brownian dynamics analysis. ACS Nano. 2017;11(10):10053-61.

[182] Shao L, Andrén D, Jones S, Johansson P, Käll M. Optically controlled stochastic jumps of individual gold nanorod rotary motors. Physical Review B. 2018 8;98(8):085404.

[183] Friedrich L, Rohrbach A. Surface imaging beyond the diffraction limit with optically trapped spheres. Nature Nanotechnology. 2015 12;10(12):1064-9.

[184] Biswas A, Alex A, Sinha B. Mapping Cell Membrane Fluctuations Reveals Their Active Regulation and Transient Heterogeneities. Biophysical Journal. 2017 2;113(8):1768-81.

[185] Chen K, Gu Y, Sun W, Bin Dong, Wang G, Fan X, et al. Characteristic rotational behaviors of rod-shaped cargo revealed by automated five-dimensional single particle tracking. Nature Communications. 2017 12;8(1).

[186] Maurice L, Bilenca A. Three-dimensional single particle tracking using 4π self-interference of temporally phase-shifted fluorescence. Light: Science & Applications. 2023 3;12(1):58.

[187] Nozue S, Ali R, Wu Y, Habuchi S. Long axial range 3D single-particle tracking using birefringent substrates. Nature Communications. 2025 7;16(1):6728.

[188] Soukar J, Peppas NA, Gaharwar AK. Organelle-Targeting Nanoparticles. Advanced Science. 2025 2;12(7).

[189] Piao S, Amaravadi RK. Targeting the lysosome in cancer; 2016.

[190] Tang T, Yang Zy, Wang D, Yang Xy, Wang J, Li L, et al.. The role of lysosomes in cancer development and progression. BioMed Central Ltd; 2020.

[191] Wang JM, Zhang FH, Liu ZX, Tang YJ, Li JF, Xie LP. Cancer on motors: How kinesins drive prostate cancer progression?. Elsevier Inc.; 2024.

[192] Nturubika BD, Guardia CM, Gershlick DC, Logan JM, Martini C, Heatlie JK, et al. Altered expression of vesicular trafficking machinery in prostate cancer affects lysosomal dynamics and provides insight into the underlying biology and disease progression. British Journal of Cancer. 2024 11;131(8):1263-78.